UNIVERSITÀ DELLA CALABRIA

Scuola di Dottorato in Scienze e Ingegneria dell'Ambiente,
delle Costruzioni e dell'Energia

Department of Environmental engineering

Advanced membrane-based operations for recovery of minerals from desalination brines and exhaust batteries leachate.

CHIM 07

PhD student: Giuseppe D'Andrea

Cycle: XXXVI

SIACE coordinator: Prof. Salvatore Critelli

Salvatore Critelli
04.09.2024
06:12:40
GMT+01:00

Supervisor: Prof. Efrem Curcio

Co-supervisor: Prof. Sergio Santoro

Abstract

The need to implement innovative technological approaches to secure undistorted access to raw materials and minerals is due to EU high dependance on import of several metal ores from international market and to problematic politic relationship with governance of countries where minerals extraction takes place, in conjunction with excessively high import reliance.

In this scenario, the recovery of valuable metals and minerals (M&M) for commercial purposes from seawater desalination brines represents a promising potential path which has been raising interest over the past few years, considering that seawater is composed by 3.3% of dissolved salts and it is considered an invaluable source of minerals.

In addition, this strategy represents an innovative approach from an environmental point of view, promoting the valorization of brines, that today are considered wastes and are rejected back to seas and oceans with an enormous impact on flora and fauna.

In this thesis work, Membrane Distillation technology has been employed in combination to carbon-based photothermal nanomaterials as performance enhancers for minerals recovery from seawater brines and, moreover, in Air-gap configuration for the treatment of real groundwaters collected from former iron mines near Stockholm.

On the other hand, this work is also aimed to point a steering direction for further developments in Donnan Dialysis process for the selective extraction of Magnesium from concentrated brine with the employment of commercial Cation Exchange Membranes. Moreover, a systematic investigation of ion exchange membrane selectivity towards different competing ions in brine treatment has been performed in combination to a Matlab process simulation, highlighting a thrilling match between simulation and real Dialysis process.

In addition, Membrane Distillation technology has been included in an integrated system consisting in precipitation and distillation steps, aimed to solve complex separation problems connected to battery recycling and recovery of strategically important elements from battery leachate.

During this last task, Lithium was successfully extracted from acid leachate with remarkable recovery percentages combined to a water recovery above 65%, obtained thanks to the concentration stage performed through Air-gap Membrane Distillation.

Table of contents

Chapter 1 - Introduction

1.1. Problem statement

Today, the world population is expected to increase from 7,7 billion in 2017 to 9,4-10 billion in 2050, with two-thirds of population living in cities and consequently it is estimated that more than 50% of countries on our planet could address water stress on water storage by 2025, while by 2050, as much as 75% of world population could address water scarcity [1].

Considering that seawater is the 98% of the water present on earth, the seawater desalination processes represent the major solution and the most reliable and economically sustainable way to produce drinkable water in order to face the future water scarcity problem.

In the last years, the market has been largely dominated by Seawater Reverse Osmosis (RO), a mature and tested technology that, since the end of the 1970s, saw a significant reduction of energy consumption due to process and technological improvement [2]. At the end of 2017, there are around 19000 desalination plants worldwide with a total capacity of 99.8 million m^3/day [1] and according to Ji et al. [3] the capacity of Reverse Osmosis desalination industry, in the same period, can be estimated around 20 million m^3/day. The water recovery in seawater R.O. operations vary from 30 to 40 %, with the subsequent rejection of the remaining concentrated brine. These brines are usually rejected, with dangerous environmental impact on soil, groundwater and marine ecosystems. So, in Reverse Osmosis plants the principal by-product, that soon becomes waste product, is the brine resulting from the filtration, characterized by a high concentration of salts and specifically elements and species like: Chlorine, Sodium, Sulphates, Magnesium, Calcium and Carbonates [3].

On the other side, as can be seen from the Figure 1.1 (https://ec.europa.eu/growth/content/raw-materials-scoreboard-2018_en), Eu is highly dependent on import of several metal ores from international market, with many implications for the feasibility of sustainable industrial development in sectors such as chemical, automotive, defense, energy and construction.

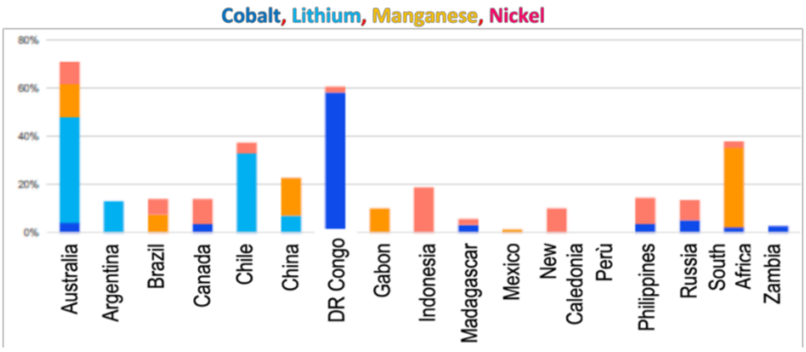

Figure 1.1 Dependence of Europe from import of ores from many international markets.

In this scenario of high import reliance, problematic politic relationships with countries (Figure 1.2) where the extraction of these minerals takes place, push towards the necessity to implement innovative technological approaches in order to secure an undistorted access to raw materials.

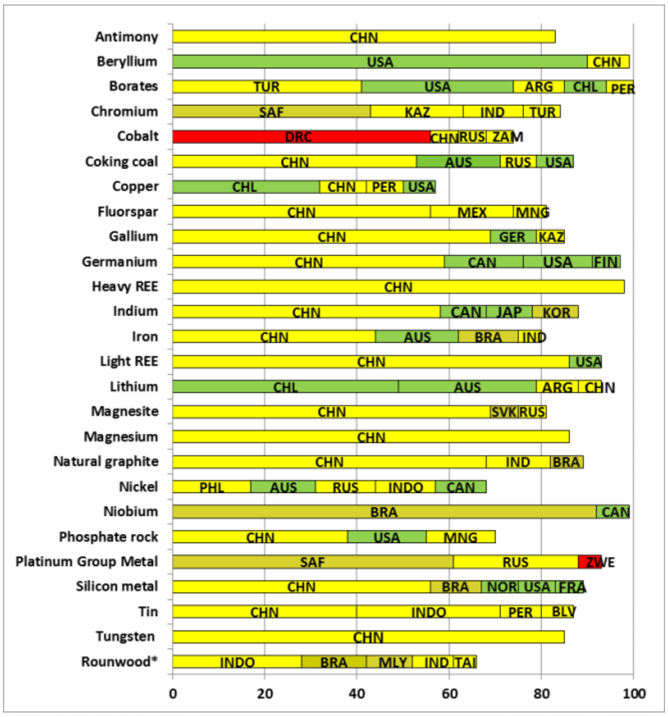

Figure 1.2 Geographical concentration of raw materials supplier countries and level of governance (evaluated in 2017) (based on WGI; red=poor; yellow=intermediate; green=good) [4].

1.2. Critical Raw Materials

The increasing demand for technological materials and components that enable certain functions for a variety of important applications, the growing world population and the fact that our earth's resources are limited raise the question of future material supply.

Construction and transportation sectors are looking for mass materials such as Copper, Zinc, Aluminium, Lead and Steel, while technology sector requires specific elements such as rare earth elements (REEs), platinum group elements and other metals including Cobalt, Silver, Tantalum, Titanium, Lithium and Tungsten.

Future supply of these materials has received increasing attention over the last few years, with the term "Critical Raw Materials" finding its way into the public debate to bear our society's future materials demand.

"Critical raw materials" describe elements that at a given time and within a given economic system are necessary for achieving certain performances and functions in a technology or product, and for which the supply of this element therefore is crucial.

The term “critical” is thus strongly related to the discussion of medium- and long-term economic and technological strategies and their advantages or disadvantages in a global competition. A classification of a raw material to be “critical” differs fundamentally from attributes such as materials properties, which can be directly linked with a material [5].

Magnesium (Mg^{2+}) is one of the major cations in seawater and its mining from brine is of economic relevance since it has been recently included in the Critical Raw Materials by the European Community due to its relevant role in different industrial sectors, as well as its potentialities as substitute of Li in battery field [6,7].

Moreover, this last alkaline element is highlighted by mineral ores and brine deposits unevenly distributed and it can be defined as the lightest metal element on Earth with an average concentration of 20 ppm in the continental crust.

Even though the demand for Li is increasing exponentially because of the ecological transition and technology industry, this element is still not labelled as critical raw material thanks to its relative abundance when compared to other metals like tin and silver [8].

With the improvement of battery technologies, lithium tends to be a promising material that plays a critical role in the lowering of carbon emissions for global warming. Thus, the supply and demand response trends of lithium resources driven by the demand for emerging renewable energy technology need to be urgently examined and revised [8].

In this contests, innovative techniques aiming to reduce the volume of Reverse Osmosis wastes and to extract dissolved salts from the rejected brines can represent an interesting opportunity towards sustainability and political independence [3].

1.3. Membrane technologies for the selective extraction of Magnesium and Lithium

1.3.1 Membrane Distillation-Crystallization

Membrane Distillation-Crystallization is a thermally driven separation process, in which a hydrophobic macroporous membrane (with pore diameters between 0.05 and 0.5 μm) separates a feed stream and a receiving phase having a lower temperature as can be observed in Figure 1.3.

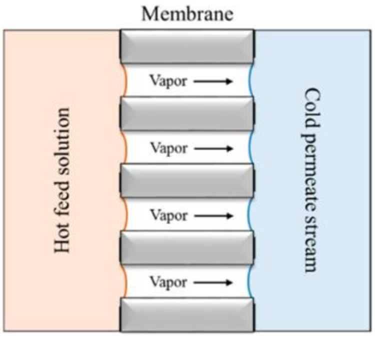

Figure 1.3 Schematization of Membrane Distillation process.

The driving force of the heat transport is represented by the temperature gradient across the membrane, which results in a water vapor pressure differential that causes transport of water through the membrane pores [9,10]. The hydrophobic nature of the membranes prevents liquid solution from entering its pores thanks to the surface tension forces and, consequently, liquid/vapor interfaces are formed at the entrance of pores [11].

So, this barrier permits only the passage of water vapor molecules, which are the most volatile. These volatile molecules will cross the membrane pores and condense on the cold liquid/vapor interface inside the membrane module. Because Membrane Distillation is a non-isothermal process in which the hydrophobic membrane is not wetted by water, it is less prone to membrane fouling, it exhibits higher rejection of solutes when compared with conventional membrane technologies such as RO, and it is unaffected by high osmotic pressure of highly saline feed [12,13]. In addition, when MD is compared with full-scale thermal distillation approaches, MD can be carried out at lower operating temperatures and pressures because it requires lower vapor space (due to membrane barrier), it has good compatibility with waste heat sources or renewable energy, and it can be used for decentralized applications because of its less complex configurations [9,14].

Some investigations on Membrane Distillation at high recovery factors demonstrated the possibility to concentrate saline solutions up to supersaturation, thus implementing the innovative concept of Membrane Crystallization (Drioli et al., 2015). Crystallization is an old chemical operation which aims to produce, separate and purify the solid products but it has been considered as “unit operation” starting from the 70s. Specifically, it is a process where a solution became supersaturated in order to achieve solute separation and component solidification generally via solvent evaporation, hence, heat and mass transfer processes are key issues for the crystallization process [16].

On the other hand, MCr can be identified as the protraction of water recovery - via MD - up to supersaturation conditions of the saline solution [10,15,17,18]. As a consequence of the previous-described features and of the total absence of osmotic phenomena, MD and MCr can be implemented as a synergic complement to the conventional pressure-driven processes in desalination and mineral recovery from brines [19].

Among the limitations that hinder the Membrane Distillation applications at operational level, we can identify temperature polarization and high energy input (> 100 kWh per m^3 of distillate in presence of heat recovery) [20] [21] [22]. Temperature polarization is a phenomenon intrinsically related to the removal of latent heat associated to water evaporation, causing a decrease of the temperature at the surface of the membrane and, consequently, at the transmembrane flux [20].

Lithium present in salt-lakes or in geothermal waters generally reduces the water activity because of his high solubility, hindering the extraction processes of Li via Membrane Crystallization.

Also, the direct extraction of Mg from brine is still allusive because of its low concentration (ca. 0,1 M) imposing the need of an additional stage of concentration [23].

With respect to this, Membrane Distillation (MD) is an attractive process having the potentialities to intensify the desalination up to a water recovery factor of 90% [13] [24]. However, the Membrane Distillation-Crystallization is emerging during the last decade as a convenient solution to obtain a rapid concentration of the brines and, accordingly, a generous further recovery of water from the same brine [25]. Another advantage of Membrane Distillation is the possibility to compensate the energy demand with renewable and green energy sources.

Beyond the hybridization of MD with renewables, the recent achievements in thermoplasmonics have opened the door for the advent of Photothermal Membrane Distillation (PhMD), where photothermal nanoparticles are embodied into/onto hydrophobic microporous polymeric membranes leading to the development of self-heating membranes under a resonant radiation [18].

The integration of nanofillers enabling a UV light-to-heat conversion showed an 11 times enhancement of the transmembrane flux, by overcoming the TP [18][26][27][28].

This approach has simulated the development of photothermal membrane based on a wide variety of nanomaterials able to efficiently exploit the solar radiation to harvest the heat required for PhMD process and to reverse the TP (es. NiSe [29], CoSe [29], Graphene [30], WS_2 [31] and carbon black [32]) demonstrating the potentialities of PhMD to intensify the concentration of the brine using the natural radiation without impacting on the anthropic energetic input.

In this scenario, the first goal of the present research work is to enhance and upgrade the performances of a classical Membrane Distillation process with the integration of 2D photothermal nanomaterials in order to cancel the effect of Temperature Polarization and to lower the high energy demand. This step has the objective to evaporate the solvent concentrating up to supersaturation

Reverse Osmosis Brine and to perform the Crystallization process of part of dissolved salts with their subsequent recovery. These 2D nanostructures and/or carbon-based nanomaterials must exhibit a broadband excitation spectrum well matching with sunlight radiation, a relatively low thermal conductivity and a suitability for solution processing. These 2D nanostructured materials are a rising family of nanomaterials and, in the case of 2D semiconductor nanostructures, show a strong absorption at the wavelength matching the bandgap energy, in fact when irradiated by light, electron–hole pair is formed with similar energy corresponding to bandgap. Then, the stimulated electrons fall back to the low energy states and the energy is released through radiating photons, or nonradiative phonons in the interaction with defects or surface dangling bonds [33]. It has been demonstrated that also noble metals as Ag nanoparticles in PVDF membranes behave as nanoscale thermal hotspot under UV light irradiation [34], due to the excitation of plasmons localized in metal NPs which results in a coherent oscillation of the charge density [33].

A MD-MCr bench-scale plant operating with synthetic RO brine can reach a water recovery greater than 90%, with the subsequent reduction of waste discharged to sea [35]. In literature, the Membrane Distillation-Crystallization process has been investigated for the concentration and purification of the Lithium from brine while recovering fresh water (solvent)[25]. Cerda et al. carried out Lab-scale Membrane Crystallization experiments with synthetic Li brines in order to evaluate the efficiency of Membrane Crystallization in terms of water recovery and brine purification and proposed a feasible approach, supported by an experimental simulation methodology, in order to move forward with an industrial application of Membrane Crystallization process in complex multicomponent systems. In another study, an experimental and theoretical comparative analysis of DCMD-MCr, OMD-MCr and VMD-MCr for treatment of highly concentrated solutions has been performed with the goal to recover crystals from single LiCl salt solutions [36]. In this study of Quist-Jensen et al., the Vacuum configuration showed the higher lithium concentration reached in combination with the minimum temperature polarization and low resistance to vapor transport through membrane pores. According to Park et al. [37] it is possible to develop a membrane-based lithium recovery process by combining Membrane Distillation and Nanofiltration to concentrate a brine solution containing lithium and to remove divalent ions such as Magnesium and Calcium. The proposed membrane-based process was demonstrated to concentrate 100 ppm lithium solution in artificial brine to 1200 ppm lithium solution within several days and exhibited up to 60 times higher water flux (22.5 L m^{-2} h^{-1}) than that of solar evaporation (0.37 L m^{-2} h^{-1} at 30°C and 0.56 L m^{-2} h^{-1} at 50°C).

Also Nanofiltration (NF) can be considered a suitable technique for lithium extraction from brine on the basis of both Donnan exclusion and steric hindrance, which make it capable of rejecting multivalent ions but allowing monovalent ions to pass [38]. The same author stats that the Supported Liquid Membrane technology represents an alternative approach for Lithium recovery because of the low energy demand and the low solvent consumption in combination with a high selectivity, due to an organic phase containing an organic extracting molecule that selectively binds to a target metal ion and forms lipophilic metal-organic ligand species.

1.3.2 Donnan Dialysis

On the other hand, Donnan Dialysis (DD) is an attractive process for the concentration of valuable materials in an ionic form from diluted solutions or removing undesirable ionic species from solutions.

In general, DD is a membrane-based equilibrium process and it is different from the classical dialysis technique. It is used to exchange ions between two solutions, the feed (A) and receiver (R) solution, separated by an ion-exchange membrane (Figure 1.4). The difference in the electrochemical potential on both sides of the membrane acts as the driving force. Thus, fluxes of the two counter-ions moving through the membrane appear in opposite directions [39].

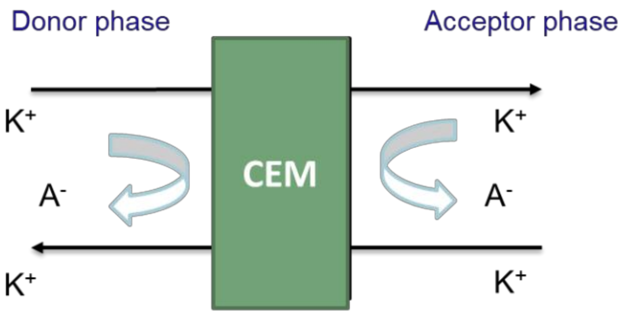

Figure 1.4 Schematization of Donnan Dialysis process implemented with Cation Exchange Membranes (CEMs).

It can also be asserted that Donnan dialysis exhibits advantages over similar processes such as electrodialysis on the basis of its non-susceptibility to membrane fouling, ease of operation, cost effectiveness, and energy savings [40]. In this process, the feed solution is separated from a receiver electrolyte of relatively high ionic strength by an Ion Exchange Membrane composed of a water-insoluble polymer with fixed ionogenic groups, mainly sulfonic for the Cation-Exchange Membrane (CEM) and tetraalkylammonium for the Anion-Exchange Membrane (AEM).

In the case of Cation Exchange Membranes (CEMs), the transport of cations is allowed whereas the permeation of co-ions is hindered due to the electrostatic exclusion (referred as Donnan exclusion) from the membrane phase and, simultaneously, cations from the acceptor solutions diffuse through the membrane to maintain electroneutrality in both solutions [41]. In this latter work they made a review of many research works focusing on the analytes, type of membranes and acceptor phases in separation/preconcentration of metal ions.

This process has been employed to study the removal of Ca and Mg ions from water samples with the use of PVDF membrane modified with polyaniline, poly-n-etylaniline, poly-n-metylaniline and poly-o-anisidine doped with1,3 (6 or 7)-napthalenetrisulfonic acid (NTSA) through acidic solution as draw solution ([39]) or using Neosepta standard-grade CMX, and standard-grade Type II CEMs FUJIFILM with saline solutions as strip observing a reduction of divalent cation content in feed between 76 and 90 % phase [42] [43] [44]. Similarly, DD was explored as a separation process aimed to tap water softening, operated with a stripping solution made of NaCl with a removal efficiency around 75% [45]. With the same membranes, Marzouk et al. studied the removal of Ca and Mg through DD from Tunisian dam, lake, and tap water according to the Doehlert design with a Mg removal efficiency around 90% [46]. Agarwal in 2012, measured the transport rate of ions across Nafion-117 ion-exchange membrane in a DD process for mono–monovalent (Na^+ – Cs^+) and mono–bivalent (Na^+ – Ba^{2+}, Na^+ – Mg^{2+}) ion-exchange process for different salt concentrations with removal efficiencies up to 44% [47].

This kind of process have been employed also in order to study the removal of Calcium and Magnesium ions from water samples with the use of polymer modified membranes. In particular, [39] performed a Donnan Dialysis process with a strip phase composed by 0.1 M HCl and a feed phase consisting in tap water from Anadolu University, while the cation exchange took place through membranes modified with polymers by immersion method named as PVDF/PAni, PVDF/poly-n-ethylaniline, PVDF/ poly-n-methylaniline and PVDF/ poly-o-anisidine.

1.4. General Objective

The general objective of the present research project is to develop multi-disciplinary and cross-sectorial approaches with the aim to develop next-generation membrane technologies for sustainable recovery of minerals from desalination brine resources, thus accelerating the transition towards a Circular Blue Industry.

In this research work, the specific minerals under investigation are Magnesium and Lithium, both considered as Critical Raw Materials from European Union [6,7] and two of the most sought-after elements due to their large use in batteries and electronic devices production. This ambitious goal can be reached with the development of Photothermal Membrane Distillation-Crystallization incorporating 2D nanostructures based on layered materials, like for instance carbon-based nanomaterials, as graphene and carbon nanotubes, with light-harvesting properties.

Our target is to reach a MD transmembrane flux > 2 L/m^2h under solar light irradiation and a recovery factor of at least 80%. This technique will be employed for an additional concentration of brines and their supersaturation up to selective precipitation of NaCl and KCl (crystallization) followed by a Donnan Diffusion treatment for the selective transport of Li(I) and Mg(II) through Ion Exchange Membranes and reactive precipitation.

Specifically, a reactive Ion Exchange Membrane-based Crystallizer (Donnan Diffusion) will be operated downstream the retentate Nanofiltration (rich in bi- and multi-valent ions), furtherly concentrated by Photothermal Membrane Distillation-Crystallization in order to selectively transport Mg^{2+} ions towards a HCl solution in order to obtain $MgCl_2$ and lastly to precipitate selectively $Mg(OH)_2$ raising pH with a target of 80% yield or more.

Our approach for Li^+ recovery was aimed to implement hydrometallurgical process, consisting in the processing of a pretreated stream with a step-by-step removal of impurities integrated with a MD step for a further concentration of Li-containing solution in order to obtain additional water and increase the overall lithium removal in the consecutive heterogeneous precipitation stage.

In this work, the simulated exhaust batteries leachate was pre-treated through the addition of oxalic acid for a preliminary removal and recovery of Nickel, Manganese and Cobalt under the form of oxalates. Then, in order to recover the water and the Li, three main steps were systematically studied and assessed: i) pH adjustment of the leachate via $Ca(OH)_2$ addition to favour the precipitation of the residuals of sulfates; ii) Air-gap Membrane Distillation (AGMD) to increase Li concentration in the stream in combination with water recovery; iii) Li recovery through chemically induced precipitation of Li_2CO_3 via addition of Na_2CO_3 in solid phase.

Chapter 2 - Membrane Distillation in Groundwaters and Brines treatments

2.1 Introduction

Various human activities, such as ore extraction and industrial processes, disrupt the natural biogeochemical cycles leading to an accumulation of heavy metals in terrestrial and aquatic environments.

In nature, metals and minerals of industrial interest typically occur in immobilized form in sediments. However, anthropic activities have accelerated their mobility since they can be released in wastewater discharged from industries (such as mining, metal processing, electroplating, textile, tannery, and petroleum refinery) contributing to soil contamination and pollution [48]. Such wastewater can profoundly affect various living organisms, including humans, aquatic animals, and plants [49].

Despite the significant contribution of the mining sector to world's economy; the environmental impact of wastewaters originated in these processes is a major public concern [49].

These wastewaters from mining processes are rich in valuable metals and minerals that can be recovered and employed in industry coherently with the circular economy. Although today they are mostly considered low-value wastes because of the sophisticated, highly impacting and expensive techniques for the selective extraction of the elements of interest, current efforts are focused in developing sustainable processes for their valorization as resources [ref: https://doi.org/10.1016/j.clet.2021.10009].

Nowadays, wastewaters treatment exploits many conventional systems such as physics, chemistry, biology, or their various combinations. The use of chemicals in the wastewater treatment process usually produces a lot of sludge. The treatment system using microbiology requires a large area of land and a relatively long processing time. While impractical for addressing the organic pollutants, nutrients, etc., that are present in the wastewater, electrocoagulation remains the prevailing method for removing recalcitrant inorganic constituents, primarily metals, from acid mine wastewater. This process uses aluminum as electrode, and it is easy to apply wastewater treatment with an excellent ability to agglomerate various impurities [50].

The components involved in the electrocoagulation reaction other than the electrodes are the treated water as the acid mine wastewater acts as an electrolyte solution. The factors that affect the electrocoagulation process include electric current density, operating time, voltage, acid content, plate thickness, and electrode distance [50].

Because of the number of factors and of the costs affecting the traditional process, industries and scientific community are searching for innovative solutions and processes to transform these wastes in resources, in order to recover Valuable Metals and Minerals for industrial purposes and, secondary, water via dehydration for internal reuse, following the logics of Zero Liquid discharge philosophy and water recycling.

Also the implementation of Reverse Osmosis (RO) for water desalination and drinkable water production generates incredibly high amounts of brines, highlighted by an outstanding level of salinity [51].

Discharging the RO brine directly into offshore waters may result in serious coastal environment pollution and land salinization due to the previously cited high salinity levels of RO brine and several chemical agents added to pretreat seawater prior to RO [51] and, in the meantime, discharging RO brine may also cause a waste of water resources leading to a higher burden of associated facilities.

The relatively low concentration of metals and minerals in mining wastewater streams impose a preliminary step to dehydrate and concentrate these streams. Among the different technologies, Membrane Distillation (MD) has the potentialities for efficiently achieve this objective. In fact, MD emerges as a membrane-thermally driven technology as a convenient technique to obtain a rapid concentration of brines or contaminated waters and, accordingly, a generous further recovery of water from the same solutions [25]. Moreover, the capability to exploit low-grade energy sources such as waste heat or renewable geothermal or solar-thermal energy makes this technology versatile and exploitable at any scale.

One of the advantages of MD is the moderate operative temperature gradient through which microporous hydrophobic membranes allow the diffusional transport of volatile compounds in vapor phase (i.e., water), with the rejection of non-volatile components (i.e., liquid water and dissolved salts).

Unlike conventional pressure-driven membrane filtration processes, liquid streams are recirculated into MD modules near to atmospheric pressure, thus determining a reduced impact of the fouling. Moreover, the absence of osmotic phenomena and the low sensitivity of MD to concentration polarization guarantee significant volume reduction and high-water recovery factor [14].

In addition to its application in wastewater valorization within the mining sector, MD has gained momentum as a pre-treatment stage in the Lithium (Li) extraction industry. In fact, Li is found in three main types of deposits: saline subsurface waters (continental brines), hydrothermally altered clays (sedimentary deposits), and pegmatites (crystalline hard rock). Lithium-bearing minerals are mainly phosphates and complex alumino-silica and in 2019 and 2020, world production of lithium was approximately 86,000 and 82,000 metric tons, which was approximately 10% less than in 2018, demonstrating that year-to-year production can fluctuate significantly, even as demand increases steadily [52].

However, the lithium distribution chain relies on deposits in aqueous solutions. As an example, Salton Sea represent the most promising geothermal source for the production of Lithium with an potential annual production of 6460–31580 mt.

In this scenario, MD can be considered a promising technology for the treatment of Reverse Osmosis (R.O.) brines for a further water recovery and an efficient Valuable Metals and Minerals concentration and extraction, employing the great potential of thermal-driven processes.

The primary objective of the activity described in this chapter is to evaluate the performance of MD in dehydrating wastewaters from the mining sector and brines, with the aim of reducing the water footprint of the mining industry. In the first part, photothermal mixed matrix membranes (MMMs) were developed by incorporating graphene oxide (GO) or carbon black (CB) into polyvinylidene fluoride (PVDF) solubilized into eco-friendly solvent (i.e., triethyl phosphate, TEP.). MMMs were prepared using the non-solvent induced phase separation (NIPS) methodology. The effect of GO or CB on MMMs morphology and the photothermal behavior were examined. The light-heat conversion was used in PhMD-MCr experiments to facilitate the evaporation of water from SWRO brine up to the supersaturation leading to Sodium Chloride (NaCl) nucleation and crystallization. Overall, the results indicate the exciting perspectives of PhMD-MCr in brine valorization for a sustainable desalination industry.

The second part of the study involved processing three different types of waters using Membrane Distillation: (i) Natural groundwater collected from an abandoned iron mine near Stockholm; (ii) A hybrid water consisting of natural water that has been artificially modified; (iii) A completely synthetic groundwater. A comparison between the three sets of feeds is expected to reveal differences in permeate quality, distillate flux, and recovery factor, dependent on the nature of the feed. Specifically, the study aims to investigate the mutual influence of the different solubilized species on these parameters.

2.2 Materials and Methods

2.2.1 Photothermal Membrane Distillation (PhMD)- Materials

Polyvinylidene Fluoride (PVDF, grade 6010) was supplied by Solvay Specialty Polymers (Italy). Triethyl phosphate (TEP) was purchased by Sigma Aldrich (Italy) and it was utilized for PVDF solubilization without further purification. Polyvinylpyrrolidone (PVP, grade K17) purchased from BASF(Germany) and Polyethylene glycol (PEG, grade 200) purchased from Sigma Aldrich, (Italy) were used as pore-forming additives. GO powder made of 15-20 sheets and characterized by a 4-10% of edge-oxidized and a density of 1.8 g·cm^{-3} was purchased by Sigma- Aldrich (Italy). Charcoal activated, also referred as CB, powder with a density of 2.31 g·cm^{-3} was purchased by Merck KGaA (Germany).

PhMCr experiments were performed using synthetic SWRO brine containing Na^+, Mg^{2+}, K^+, and Ca^{2+}as major cations and Cl^-, SO_4^{2-}, CO_3^-, NO_3^- as major anions (Table 2.1), leading to an ionic strength of 0.958 M. Before conducting the PhMCr tests, the brine was treated with sodium bicarbonate ($NaHCO_3$) to achieve a CO_3/Ca molar ratio of 1.3. This procedure was essential in reducing the risk of inorganic scaling, which is primarily caused by calcium-based compounds. The addition of $NaHCO_3$ proved to be highly effective in selectively removing Ca^{2+} ions from SWRO, causing them to precipitate as either $CaCO_3$ or $CaSO_4$. This effectiveness was recently confirmed by Molinari et al. [42]. The reagents for synthesizing the artificial SWRO brine were bought from Carlo Erba reagent (Italy).

Table 2.1 The ionic composition of SWRO brine measured by ion chromatography.

Ion	Na^+	Mg^{2+}	K^+	Ca^{2+}	Cl^-	SO_4^{2-}	CO_3^-	NO_3^-
Concentration (ppm)	35.9	4236	1356	980	41.642	4398	320	130

2.2.2 PhMD - Membrane Preparation

In order to obtain a homogeneous dispersion of the carbon-based NPs, GO or CB powder was preliminary dispersed into TEP via sonication (Sonica2200ETH, Soltec, Italy) for 30 minutes. Subsequently, the polymers (PVDF, PEG and PVP) were added to the dispersion of CB or GO and solubilized by magnetically stirring overnight (100 rpm and 70 °C).

The concentration of the photothermal filler with respect to the PVDF was 0 wt.%, 2.5 wt.%, 5 wt.% and 10 wt.%. The PVDF, PEG and PVP concentrations in the dope solutions were fixed at 15 wt.%, 20 wt.% and 5 wt.% respectively. The compositions of the polymeric solutions for the preparation of the photothermal MMMs are reported in Table 2.2.

Table 2.2 Polymeric solutions employed in the preparation of photothermal MMMs.

Membrane	PVDF	GO/CB 2.5	GO/CB 5	GO/CB 10
TEP (wt.%)	60	59.625	59.25	58.5
PVDF (wt.%)	15	15	15	15
PEG (wt.%)	20	20	20	20
PVP (wt.%)	5	5	5	5
NPs: GO/CB (wt.%)	-	0.375	0.75	1.5

Before the casting procedure, the homogeneous PVDF solutions were left without mixing for 2 hours at 70°C ensuring the removal of entrapped air. The photothermal MMMs were prepared by casting the polymeric solutions with a doctor blade (Elcometer, UK) set at 0.30 mm of thickness. The nascent MMMs were immersed in a mixture of water and ethanol (50/50 wt.%/wt.%) for 3 hours.

Then, the obtained MMMs were washed for 2 hours in distilled water and dried for 8 hours at 50 °C enabling the removal of any traces of solvent and additives (i.e., PEG and PVP).

2.2.3 Photothermal Membrane Distillation (PhMD)-Membrane characterization

The morphologies of the membranes were observed using a scanning-electron microscope (SEM, model EVO MA10 by Zeiss, Germany) at a beam energy of the electron source of 10 kV. The samples were fixed on the stubs using a conductive carbon tape and sputter-coated with a thin graphite film before analysis. Both membrane surfaces were examined. For cross-section observations, the membranes were frozen by immersion in liquid nitrogen (1 min) and subsequently fractured to preserve the microporous structure.

A set-up for contact angle measurements (Drop Shape Analyzer-DSA30, Kruss GmbH, Germany) was employed to evaluate the membrane hydrophobicity according to the sessile drop method at ambient temperature.

Pore size and bubble point measurements were conducted using a Capillary Flow Porometer (INNOVA-500NX, Porous Materials Inc., USA) under the management of the software Capwin

(Porous Materials Inc., USA). The wet up/dry-up method was employed using Galwet® (surface tension of 15.9 dyne·cm^{-1}) as the wetting liquid. The results were processed using the Caprep software (Porous Materials Inc., USA).

The porosity (ε) of the membranes was determined with the gravimetric method. Briefly, the membrane was weighed before (dry) and after being immersed in kerosene for 24 hours (wet). The value of ε was calculated using the following equation:

$$\mathcal{E}(\%) = \left\{\frac{(W_w - W_d)/\rho_k}{(W_w - W_d)/\rho_k + \frac{W_d}{\rho_m}}\right\} \cdot 100 \qquad (1)$$

where W_W is the weight of the wet membrane, W_d is the weight of the dry membrane, ρ_k is the kerosene density (0.81 g·cm^{-3}) and ρ_m is the density of the membrane material estimated from the PVDF (1.8 g·cm^{-3})[43], GO (1.9 g·cm^{-3}) [44] and CB (2.3 g·cm^{-3}) [45] densities. Three measurements for each membrane were performed to calculate the average values and standard deviations of the porosities.

Ultraviolet and visible (UV-Vis) absorption was determined using a spectrophotometer analysis, specifically the Shimadzu UV-1601 (Kyoto, Japan). The photothermal response of the MMMs was measured using an infrared (IR) camera (FLIR, model T660, USA) with a sensitivity of ca. 0.02 °C and a resolution of 640 × 480 pixels.

X-ray diffraction analysis (XRD) was performed on crystallized salts with a D8 Advance Bruker Coatings diffractometer (Billerica, MA, USA) with Cu Kα radiation (operating conditions: 2θ step-size of 0.02°at 2s/step, analytical range from 3°to 65°) to identify the constituent mineralogical phases of the obtained crystals.

2.2.4 PhMD - Experiments

Solar-driven PhMD-MCr experiments were conducted feeding distilled water or SWRO brine with a micro-peristaltic pump (Reglo, Ismatec, US) at a flow rate of 10 mL·min^{-1}. The membrane (active area 3.14 cm^2) was positioned in a module of Polylactic acid (PLA) designed with Autodesk 123D®, printed using a 3D printer (model Tornado, TEVO, China) and equipped with a transparent window exposing the feed surface to the external radiation.

During PhMCr test, the membrane module was irradiated by the light generated from a solar simulator (Abet Technologies, US) mimicking the sunlight spectrum with an irradiance of 1 sun (P_{in}=1000 W·m^{-2}) over an area field of 35 mm of diameter.

The evaporation rate was periodically determined by weighing the feed using an analytical balance (Gilbertini, Model E 50 S/3). The temperature during the experiments was 25.8±0.5 °C and the relative humidity was maintained at 47 ±4 %. Experiments of solar-driven PhMD-MCr were repeated 3 times and the mean values of the water evaporation fluxes and the experimental errors were then calculated.

2.2.5 Air-Gap MD

The goal of the current experimental session is the processing via Membrane Distillation of three different types of waters: (i) A Natural groundwater collected from an abandoned Iron mine near Stockholm; (ii) A hybrid water made of a natural water artificially modified; (iii) A totally synthetic groundwater.

The comparison between the three sets of Feeds mentioned above is expected to show the difference of permeate quality, Distillate flux and Recovery factor in dependance of the Feed nature, more specifically, the mutual influence of different species solubilized.

The experimental session consists in the treatment of three different Feeds, each one performed three times:

a) Natural Groundwater collected from a former iron mine near Stockholm (fig. 2.1)
b) Hybrid water consisting of the natural Groundwater above-mentioned enriched with 150 mg/L of Li.
c) A completely synthetic water containing only Li in the same concentration of the hybrid water (150 mg/L).

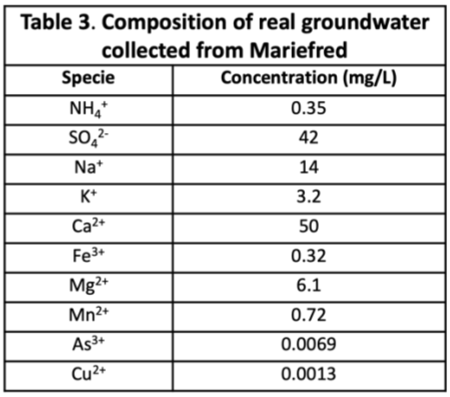

Table 3. Composition of real groundwater collected from Mariefred

Specie	Concentration (mg/L)
NH_4^+	0.35
SO_4^{2-}	42
Na^+	14
K^+	3.2
Ca^{2+}	50
Fe^{3+}	0.32
Mg^{2+}	6.1
Mn^{2+}	0.72
As^{3+}	0.0069
Cu^{2+}	0.0013

Figure 2.1 (right) Entrance of the former Iron mine in Mariefred, near Stockholm and **Table 2.3** (left) composition of groundwater collected.

Figure 2.2 Air-Gap MD equipment employed in Circular Water Technology.

Lithium employed in Feed (b) and (c) was purchased from Sigma Aldrich-Sweden and its concentration has been determined considering the concentration of the same metal in Geothermal waters and brines found in literature [37,53]. Deionized water was produced by Sweltech Reverse Osmosis pilot plant. The Membrane Distillation process worked in Airgap configuration by courtesy of Circular Water Technology , as shown in Figure 2.3, with a double-layer flat-sheet membrane module constituted by PTFE-PP and with an exchange surface of 1886 cm^2 with a thickness of 67μm and a nominal pore size of 0,22 μm.

The Feed temperature is kept at 50°C, in combination with an open circuit cooling system with tap water at 14°C.

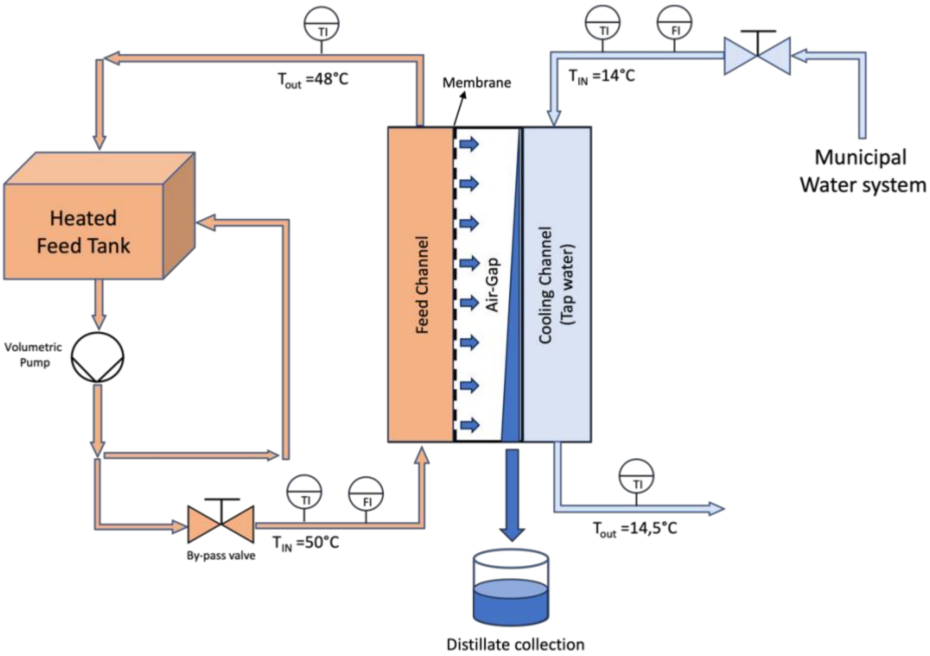

Figure 2.3 Scheme of the employed AGMD process.

The temperature and the acidic pH of the Feed have been chosen considering that the solubility of ammonia present in the Feed decreases significantly with increasing feed temperature and/or increasing pH values[54,55].

According to what explained above, the pH of the untreated Feed solution has been set with the addition of 10 mL of 5% H_2SO_4, purchased from Sigma Aldrich-Sweden and kindly supplied by KTH Chemical engineering department, in order to reach pH value of 3.6 – 3.8.

The process parameters monitored on-line are: (i) Height of the Feed in tank; (ii) Distillate quality (conductivity); (iii) Distillate Flowrate. Temperatures of Feed and cooling water leaving the MD cell were also monitored on-line.

Initial value of pH was measured using Filter-Lab® indicators, while the conductivity in Feed and Distillate side conductivity was measured with the employment of a portable Hanna HI98192 conductometer.

Distillate collection and weighting for flux computations have been performed using a scale Mettler Toledo model PG503-S Delta Range. The flowrates of cooling water and Feed water were kept respectively around 5 and 2,5 L/min.

For each test, the first sample was collected at the beginning of the test, when the Conductivity of the distillate stabilizes, while the second sample is collected when the Conductivity starts to increase at the end of the test.

2.3 Results

2.3.1 Membrane characterization

The thickness of MMMs, measured with a digital caliber, ranged from 150-166 µm for membrane doped with CB, while GO membranes presented a thickness range of 133-150 µm. These values are similar to the thickness observed for blank PVDF resulting of 161 ± 3 µm.

SEM inspections of the membrane cross-sections revealed the poor impact of both the photothermal nanomaterials on the morphology of MMMs in comparison with blank PVDF membrane (Figures 2.4). In all the cases, membranes demonstrated a heterogeneous microporous structure since the surface in touch with the coagulation bath during the NIPS stage (top surface) presented a finger-like morphology supported by a sponge-like layer (bottom surface). This because of the differences in the kinetic and thermodynamic aspects governing the NIPS between the two surfaces of the nascent membranes [56], as already discussed by Marino et al. for PVDF membranes prepared using TEP as solvent [57]. In fact, the top surface was obtained by the direct exposure of the cast polymeric solution with the coagulation bath encouraging a rapid demixing and the consequent formation of finger-like pores [58]. Upon diffusion, the non-solvent induced a delayed NIPS of the polymeric solution in the bottom surface with a consequent sponge-like morphology [59]. Also, Pagliero et al. observed a sponge-like morphology for PVDF membranes prepared using TEP as solvent and doped with GO or CB and employing ethanol as non-solvent [60]. In our case the presence of the water in the coagulation bath accelerated the NIPS stage leading to the appearance of finger-like pores [61,62]. It is worth to be mentioned that the presence of finger-like pores in MD membranes is highly desirable since they offer a minimal resistance to the mass transport of water vapor and reduce the membrane conductivity.

The different surface morphology impacted on their hydrophobicity: the bottom spherulitic-like surfaces presented higher roughness increasing the contact angle according to the Wenznel equation [63]. In fact, the bottom surface of the GO10 membrane showed a contact angle of ca. 119°, 20° higher than the finger-like smooth top surface.

Despite poor impact on membrane morphology, the organization of the polymeric chains during the NIPS was disturbed by the presence of the photothermal nanoparticles leading to an increment of the porosity.

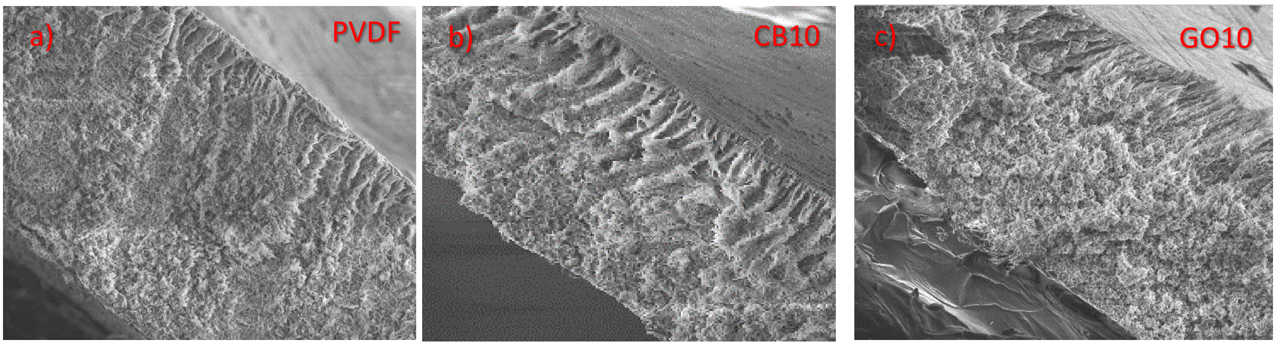

Figure 2.4 SEM Pictures (Magnification: 1,000 X) of: a) blank PVDF membrane (PVDF); b) MMM load with 10 wt.% of CB (CB10) and c) MMM load with 10 wt.% of GO (GO10).

In fact, blank PVDF membranes showed a porosity of 70.6 %, lower than the values measured for developed MMMs with exception for CB 10 (Table 2.4). In fact, the porosity of PVDF-based membranes progressively increased to 78.1% and 82.0% raising the CB concentration to 2.5 wt.% and 5 wt.% respectively. A further improvement of the CB to 10 wt.% decreased the porosity to 67% because of the high content of fillers decreasing the void space into the PVDF matrices. This effect was not observed for MMMs prepared with GO hitting a porosity of 85.2% for a loading of 10 wt.% thanks to the effective dispersity 2D flakes [60,64].

In all the cases, MMMs presented sub-micrometric pore sizes with average values in the order of 0.1-0.2 µm (Table 2.4). These results are in accordance with the recommended pore size for MD application finding a balance between the needs to maximize the mass transport and to minimize the risk of pore wetting [65]. In fact, the average pore size for blank PVDF was 0.092 µm with a largest pore detected at 0.219 µm (bubble point of 2.08 bar). The variation of the concentration of CB nanoparticle weakly influenced the pore size since fluctuations below than the 25% were observed on the average pore size. On the other hand, the loading of 2.5wt% of GO in PVDF lead to an increase in the average pore size of 2-folds (from 0.92 µm to 0.184 µm) coherent with the growth of the porosity (from 70.6% to 84.6%). Further improvement of the GO concentrations provoked a gradually reduction of the average pore size up to 0.075 µm for an embodiment of the 2D flaskes of 10 wt.%.

Table 2.4 Comparison of thickness, mean pore diameter, pore distribution and contact angle of the developed photothermal MMMs.

Membrane	Thickness (µm)	Average pore size (µm)	Porosity %	Contact Angle Top (°)
Bare PVDF	161 ± 3	0.0920	70.6	87.4 ± 2
CB 2.5	152 ± 1	0.1125	78.1	92.6 ± 2
CB 5	166 ± 2	0.0917	72.55	110.4 ± 1
CB 10	150 ± 3	0.0709	67.0	113.4 ± 2
GO 2.5	150 ± 2	0.185	84.6	94.3 ± 2
GO 5	133 ± 1	0.1262	80.6	119.7 ± 2
GO 10	133 ± 1	0.0748	85.2	118.8 ± 2

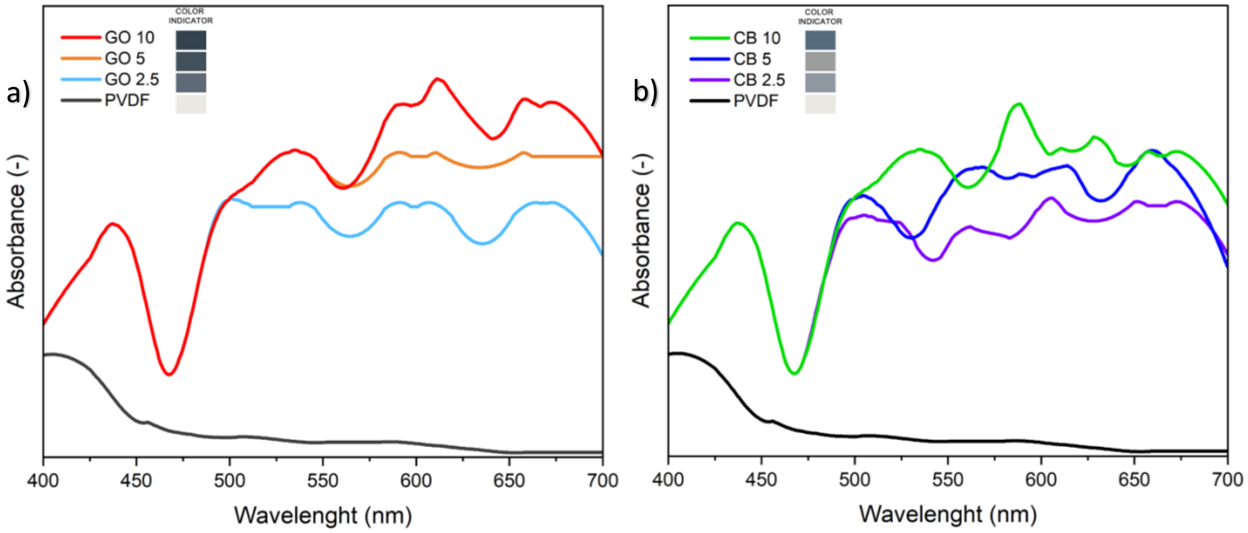

Figure 2.5 Visible spectra of the membranes at different GO (4.a)/CB(4.b) loading.

The color of MMMs changes from white to grey to black as the loading of GO or CB nanofillers increased. This change in color is reflective of the enhanced absorption in the visible region of the electromagnetic spectrum, as demonstrated by the UV-Vis spectra (Figure 2.5). Also, the absorption spectra confirmed the poor interaction of the neat PVDF with the irradiation, while the carbon-based nonmarital exhibited an intense and wide absorption the in range from 470 nm to 700 nm (Figure 2.5), matching the peak of the sunlight irradiation on Earth.

2.3.2 Photothermal Membrane Distillation (PhMD)

In Figure 2.6 it is revealed a notable gradation of membranes color, from gray to shadow, at increasing nanofiller content and, in order to investigate irradiance (i.e. irradiated power per unit area) of the system, a light source was employed to simulate solar energy on the surface of produced membranes. The irradiance must be compared to the average yearly standard solar conditions at the sea level [66].

The infrared pictures, obtained by IR CAMERA model FLIR E50 BX (FLIR, USA) with a sensitivity < 0.05°C at 30°C, confirmed that the exposure of the membranes loaded with GO or CB caused a noticeable enhancement of the surface temperature under the solar radiation (Figure 2.7).

In fact, from a physical point of view, in carbon-based nanomaterials (e.g., carbon black, carbon nanotubes, graphene, graphene oxide (GO), and reduced graphene oxide (RGO)) the closely spaced energy levels of the loosely held π electrons can effectively absorb light at different wavelengths and heat is generated when the excited electrons relax to their ground state. Usually, these carbon-based photothermal nanomaterials exhibit broad-band absorbance, chemical stability, low density, and low-cost [67].

The highest surface temperature, experimentally observed for the membrane loaded with GO 10 wt%, reached the value of 53.7°C at steady state under light radiation emitted by the solar simulator Abet Technologies (US) characterized by irradiance of 1 sun (1000 W m^{-2}) over a 35 mm diameter field. On the other hand, the maximum temperature attained under steady state by CB 10 wt.% was 49.7°C, a 7.5% lower value registered in GO-loaded photothermal membranes.

These reached temperatures can be justified considering that GO has an excellent 95% absorbance in visible region, decreasing as approaching near infrared (≅ 80%) and infrared regions (<80) [68], and, similarly, CB boasts a broad absorption band from 200 to 1400 nm with a wide maximum in the visible light range [66].

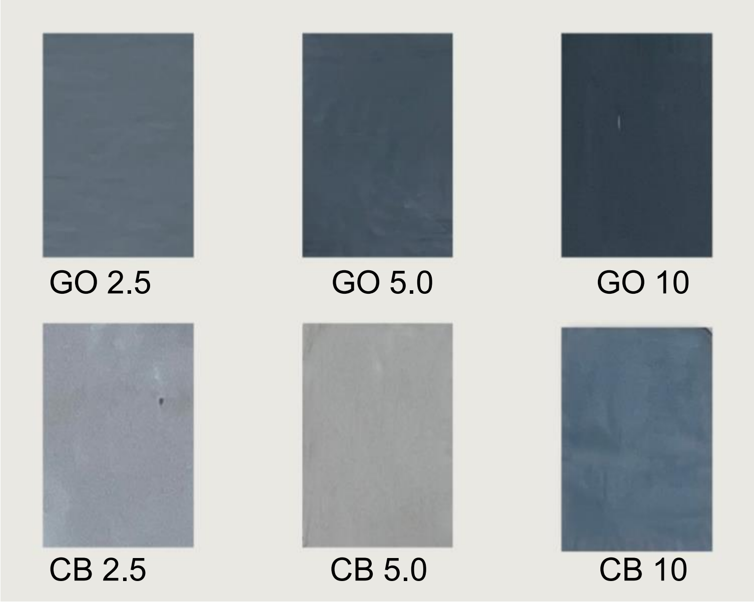

Figure 2.6 Pictures of lab-made photothermal membranes incorporating nanofillers after 1 hour exposure to sunlight simulator.

The obtained results are coherent with other works of scientific community, in fact, consequently to the exposure to an identical radiation power (1000 W m^{-2}), GO membrane surface charged with 5 %w/v of photothermal material reached a temperature of 53°C in Gaffer et al paper [68], in comparison to the 52°C reached from 5 wt% in our tests.

In contrast, no relevant temperature variation was observed for the bare PVDF membrane and this is due to the scarce absorption in the wavelength interval of our interest, in fact most of the solar radiation was reflected by the white surface of the bare (i.e. not functionalized) PVDF membranes.

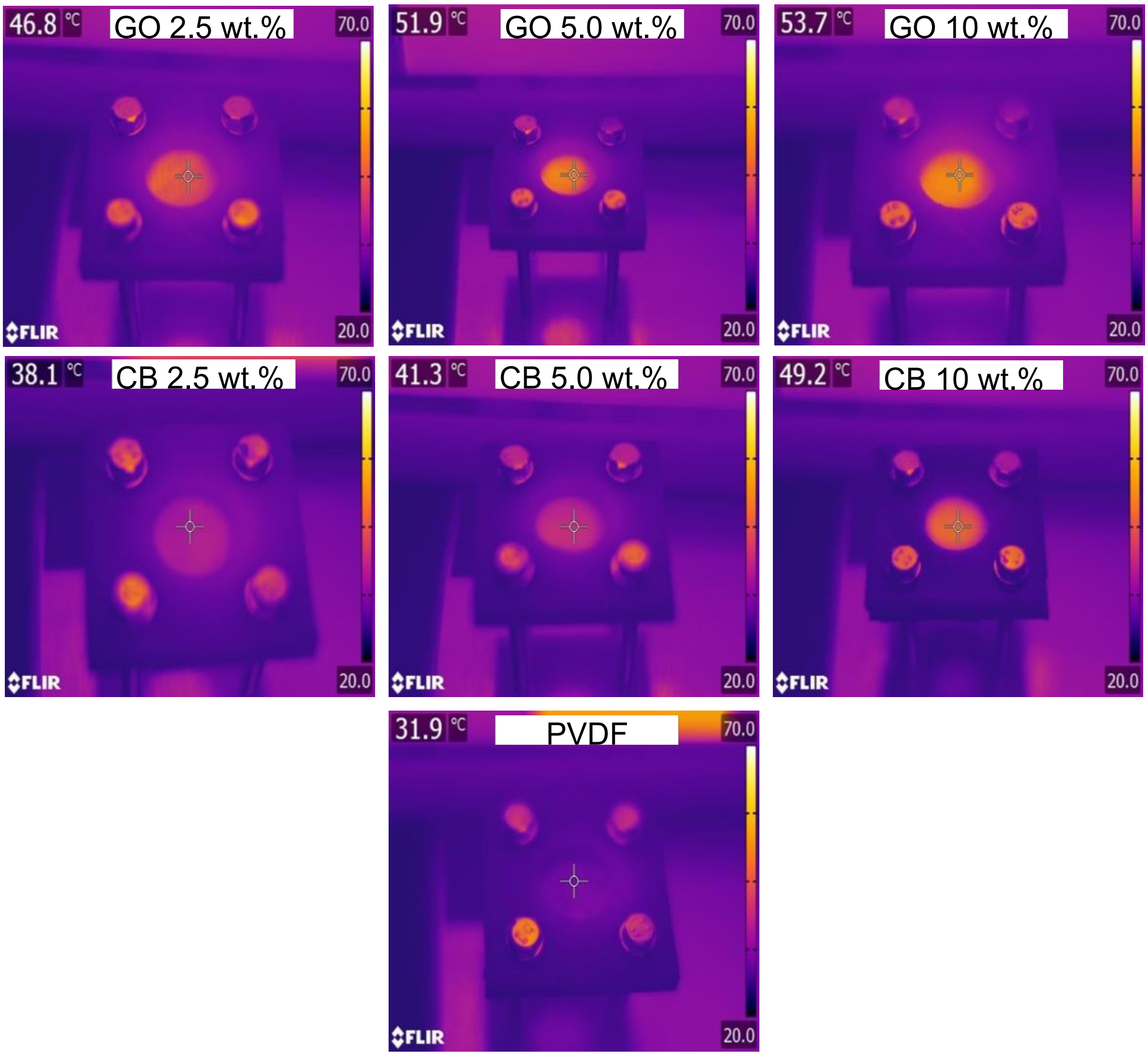

Figure 2.7 Infrared pictures of membranes under solar simulator after 60 min irradiation (1000 W m^{-2}).

It is very interesting to notice dissimilar increment percentages of temperature on the basis of the increment of photothermal Nanoparticles (PhNPs) concentration showed in Figure 3a.

The increment of PhNPs concentration from 2.5 to 5 % brought an increase of temperature quantifiable in 11 % and 8.4 % for GO and CB respectively.

In GO mebranes, the doubling of PhNPs concentration from 5 wt % to 10 wt % causes an increment of temperature of only 3.5 %, whereas in CB membranes the detected temperature shows an increase near to 20 %, providing an empirical demonstration of the different optimal points of PhNPs concentration parameter. To summarize, it can be stated that the temperature reached by 5 wt% GO membrane is slightly higher but comparable to the temperature reached by 10 wt% CB membrane, highlighting the superior efficiency of GO in light-to-heat conversion process.

The evolution in time of temperature at the membrane surface is illustrated in Figure 2.8; thermal profiles typically reach the steady state at 30 min, with a rapid increase within 5 min.

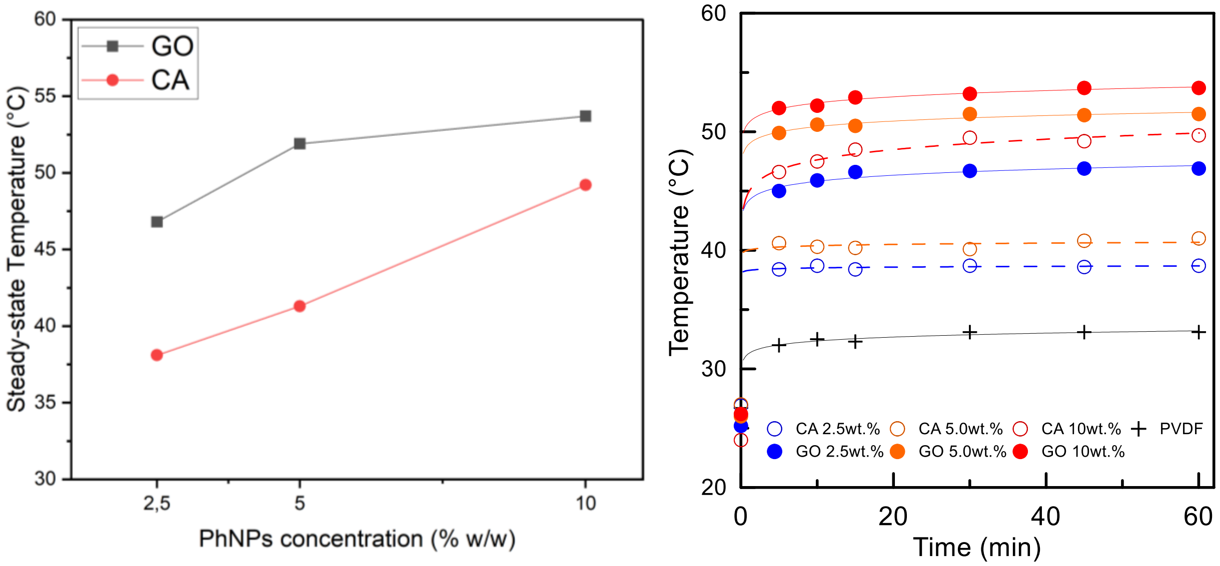

Figure 8. Temperature profiles of membrane surface at different nanofiller content.

The evaporative performance of lab-made membranes was tested in a Direct Contact PhMD system (for clarity, Figure 2.9.b shows only feed line). Membranes were placed in polylactic acid (PLA) modules, each one with active area of 3.14 cm^2 and equipped with a transparent window to enable the light radiation exposure via solar simulator. In each test, the saline feed solution was recirculated at 10 mL·min^{-1} by micro-peristaltic pump Reglo (Ismatec, US). Evaporative flux was quantified by measuring at regular time intervals (15 min) the weight variation of the feed tank, as registered by a balance Crystal 200 SMI (Gilbertini, Italy) with sensitivity of ±10^{-4} g.

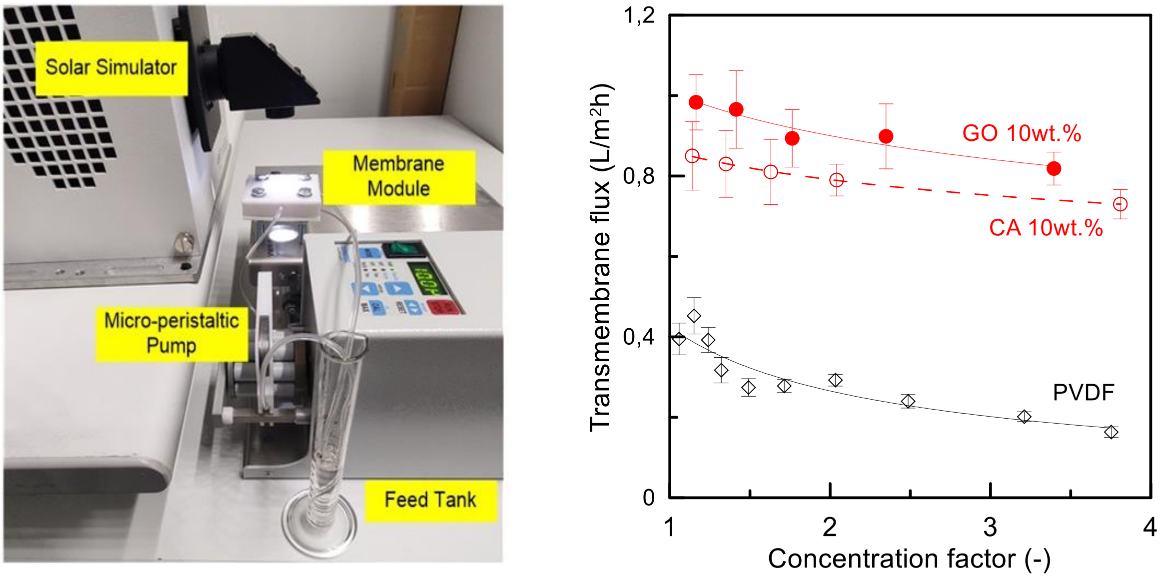

Figure 2.9 a) Lab-scale PhMD setup for evaporative tests with solar simulator; **b)** transmembrane flux as a function of concentration factor.

Figure 9.b reports the transmembrane flux for best performing photothermal membranes (i.e. GO 10 wt.% and CA 10 wt.%), and for bare PVDF as benchmark. The higher surface temperature resulted in an exponential increase of water vapor pressure as established by the Clausius-Clapeyron equation:

$$ln\frac{P_1}{P_2} = \frac{\Delta H_{vap}}{R}\left(\frac{1}{T_2} - \frac{1}{T_1}\right) \qquad (1)$$

where ΔH_{vap} and R are respectively the Enthalpy of vaporization and the gas constant (8,31 J mol^{-1} K^{-1}) and P_1 and P_2 are vapor pressures respectively at temperature T_1 and T_2.

As a consequence of water vapor pressure increase in the feed side at the membrane interface, the transmembrane flux grows linearly following its mathematical definition:

$$J_w = B_m(P_w^m - P_w^p) \qquad (2)$$

where P_w^m and P_w^p represent respectively water vapor pressure in feed side at membrane interface and in permeate side [69]. The two terms P_w^m and P_w^p are related to the temperature by means of the Raoult's law:

$$P_w^n = P_w^0(T_n)\, x_w^n\, \gamma_w \qquad (3)$$

Where $P_w^0(T_n)$ is the water vapor pressure evaluated at the temperature of the n compartment, x_w^n and γ_w are respectively the water molar fraction and water activity coefficient ($\neq 1$ for non-ideal mixtures) [26].

Coherently, the highest initial flux (0.98 L/m^2h) was measured for GO 10 wt.% membrane, that is about 15% greater than the one detected for CA 10 wt.% membrane. As a term of comparison, the initial flux in PVDF membrane was 0.39 L/m^2h.

The obtained results can be compared with other studies performed in literature, where similar values of permeate flux ($\approx$ 0,55 kg/m^2h) have been observed at pilot-scale plant with PVDF membrane charged with 1 wt% CB [32].

In all experiments, the progressive removal of water decreases its molar fraction, which determined a decrease of the evaporative rate according to Raoult law (eq 3). This effect, amplified by the reduction of the water activity coefficient due to increased salt concentration, causes a reduction of transmembrane flux at increasing concentration factor by about 15%. Interestingly, a drastic decrease (60% c.a) was found for PVDF membrane, presumably due to the negative impact of temperature polarization phenomena that lower the temperature at membrane interface under the form of latent heat of evaporation and not mitigating it through photothermal effect [70–72].

2.3.3 Groundwater treatments via AGMD

The goal of the current experimental session is to process via MD three different types of waters: (i) A Natural groundwater collected from an abandoned Iron mine near Stockholm; (ii) A hybrid water made of a natural groundwater artificially modified; (iii) A totally synthetic Li-containing groundwater.

The trend of permeate quality in the three feeds as function of time is reported in Figure 2.10.

After five hours of operation, the conductivity of distillate undergoes a slight decrease, reaching values included in the range between 1.5 and 2.5 μS/cm recording decrements up to 50%. After this time interval, values stabilize in the previous-cited range, confirming the high quality of distillate regardless of the type of the Feed.

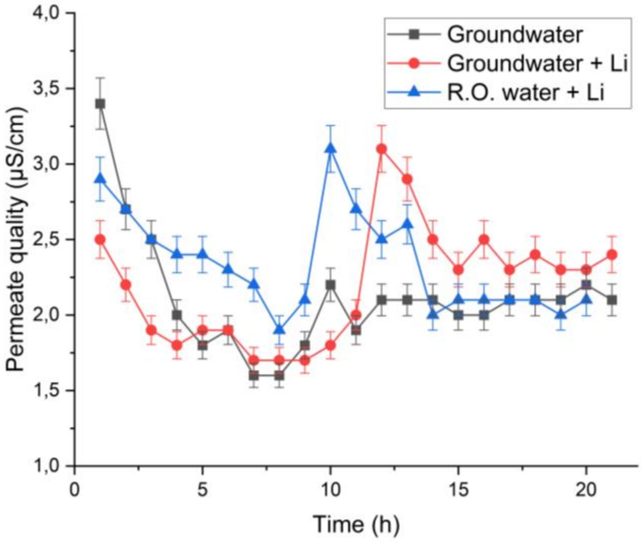

Figure 2.10 Water quality (conductivity) of distillate trend versus time.

The Distillate flux analysis (Figure 2.11) shows a common decreasing trend considering the entire time span, with decrements near to 57% for all the Feeds processed.

The observed weakening of Distillate flux during the experimental span can be attributable to the lowering of Feed partial pressure, associated to increase of the concentration of the solute in the feed according to Raoult's law (eq.3), bringing to a driving force decreasing (eq. 2)[73].

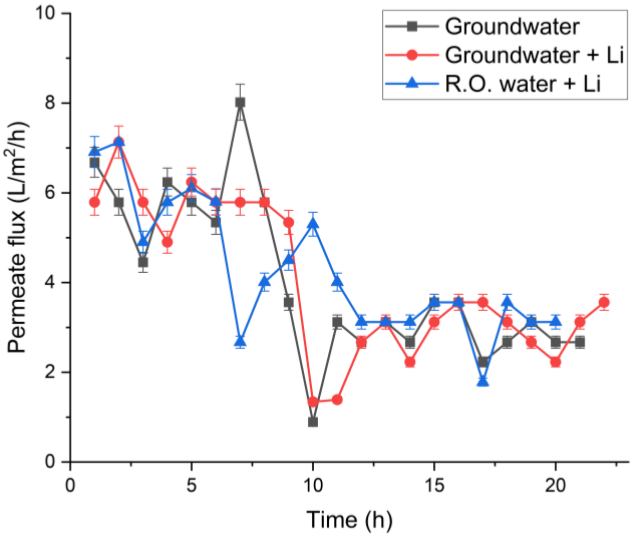

Figure 2.11 Permeate flux trend with time.

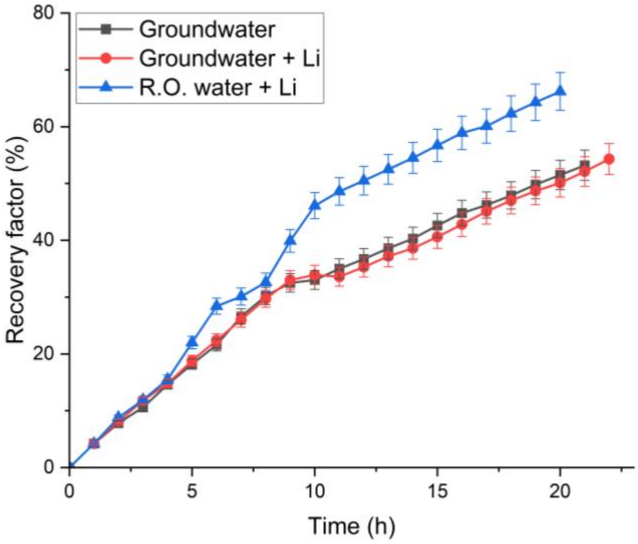

Figure 2.12 Recovery factor trend with time.

As can be also analyzed from Figure 2.12, the Recovery Factor (i.e. water recovery) trend during experimental time is superimposable for both Feeds employing natural water. On the other hand, the feed with R.O. water contaminated with Lithium shows higher values after ten hours of test with a final value of 20% higher than the other two experiments performed using natural water, highlighting the non-negligible effect of species initially dissolved in natural water collected form Mariefred former mine.

The obtained final recovery factor values are comparable with results produced in other works as, for instance, Martinetti et al. 2019 [74], where RO desalination brine feeds have been processed in combination to recovery batch values that lay between 50 and 70%.

Geng et al. [75], similarly, worked on AGMD in mono and multi-stage, respectively reaching an overall water recovery of ≈7% and ≈82%, in combination to a distillate flux of ≈7 kg/m^{2}h and ≈4 kg/m^{2}h.

It can be asserted that the presence of Lithium did not affect the quality of the water distilled with this process and the presence of other contaminants in Feed (i.e. natural water Feed) lowers the recovery factor in comparison to the R.O. water contaminated with Lithium.

2.3.3.1 Thermal analysis

MD is identified as a non-isothermal process, which means that it is a process involving a huge heat transfer through the membranes under the form of latent heat and conductive heat transfer.

Thermal energy consumed in this pre-concentration step was based on the evaluation of enthalpy change in the feed channel with an eventual sensible heat recovery on the cooling side. The heat transfer rate Q_f represent heat and Q_c is the one in the cooling side of the module and can be calculated following the eq (4) and (5):

$$Q_f = m_f\ C_{p,H_2O}\ (T_{f,IN} - T_{f,OUT}) \qquad (4)$$

$$Q_c = m_c\ C_{p,H_2O}\ (T_{f,out} - T_{f,IN}) \qquad (5)$$

where m_f and m_c are the feed and cooling water mass flow rates (kg/s) respectively, C_p is the specific heat of water (4.186 kJ/kg/K) and $T_{f,in}$ and $T_{f,out}$ are the feed temperatures (°C) at the inlet and outlet of the membrane module, respectively. $T_{c,out}$ and $T_{c,in}$ are the temperatures (°C) of the cooling water leaving and entering the MD modules respectively [76].

When the heat transferred to the cooling side is assumed to be recovered, the net heat demand for the MD process is calculated using eq (6):

$$Q_{net} = m_f\ C_{p,H_2O}\ \left(T_{f,IN} - T_{f,OUT}\right) - \varphi\ m_c\ C_{p,H_2O}\ (T_{f,out} - T_{f,IN}) \qquad (6)$$

The parameter φ indicates heat recovery on the cold side and assumes a value of 1 for higher cooling temperatures (50°C) of $T_{c,in}$ and 0 for cooling temperature of 15°C.

On the other hand, Specific heat demand, that consists in the amount of heat necessary to produce one cubic meter of permeate, is measured in kWh/m^3 and is computed from the net heat demand following the eq 7:

$$Q_{sp} = Q_{net}/m_p \qquad (7)$$

Parameter m_p indicates the permeate flowrate measured in m^3/h [77].

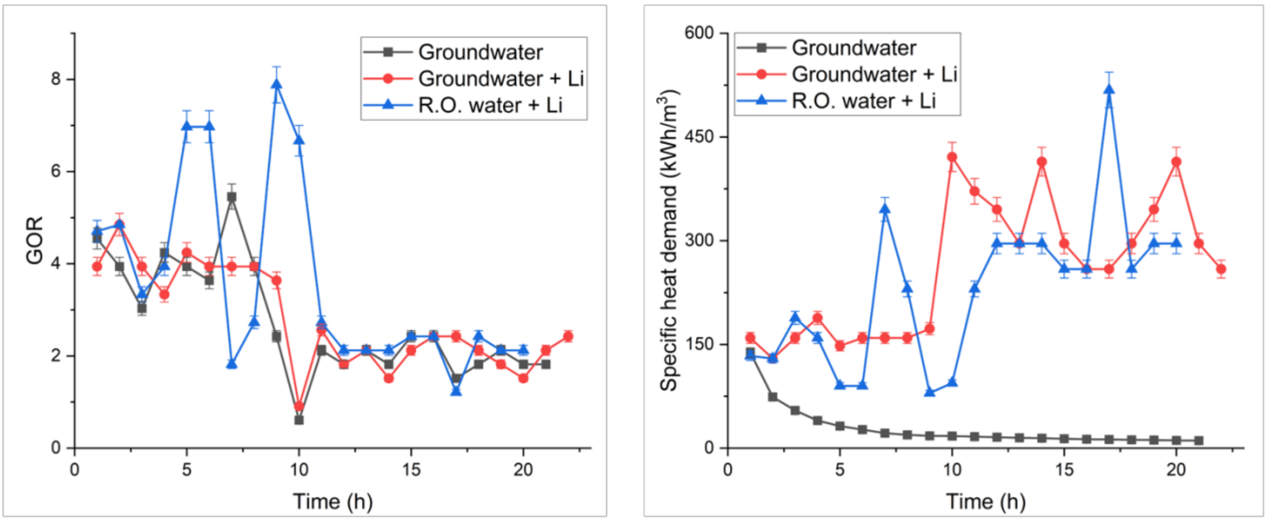

Figure 2.13 Gained Output Ratio (left) and Specific Heat demand (right) in AGMD tests.

In addition to specific thermal energy demand, Gained Output Ratio (GOR) is defined as a ratio between useful heat and the total heat input of the system, and it is employed to evaluate the thermal efficiency of the process, the higher the GOR value, the better the system perform in terms of heat recovery.

GOR can be computed using the Eq. 8:

$$GOR = \frac{J_W\, \Delta H_v\, A_m}{Q_{net}} \qquad (8)$$

J_w represents the permeate flux in (kg/m^2/s), A_m is the area of permeation in (m^2), which is equal to the total area of the membrane, ΔH_v is the enthalpy of vaporization of water in (kJ/kg), and Q_{net} is the total input power used by the MD system in (kW).

This latter parameter ranged, during the entire experimental period, in an interval included between 1.38 and 1.47, showing an experimentally observed overall reduction near to 6% according to direct mathematical relation between permeate flux and GOR expressed by eq 8 [78].

From Figure 2.13 it is possible to evaluate Gained Output ratio and Specific Heat Demand of AGMD test employed for groundwaters treatment.

Specific Heat Demand shows an increase during experimental time, with overall differences up to 100%, as in case of RO water with Lithium dissolved. This behavior depends on the gradual concentration of Feed, and it is inversely correlated to the flux of permeate (eq. 7), with a subsequent increasing heat demand for the vapor formation and permeation through the PP-PTFE membrane [79].

Analogously, GOR trend is superimposable to the permeate flux and directly correlated to distillate flux as expressed by eq. 8, showing a gradual decrease of the thermal efficiency of the process as a consequence of the increase of Specific Heat Demand [78].

In this work, the GOR values fluctuate between 2 and 5, with total decreases up to 50% in the whole experimental period, confirming the advantageous thermal efficiency of the employed pilot-scale AGMD plant.

2.4 Conclusions

In this chapter, the preparation of MMMs by the embodiment of carbon-based nanomaterials was studied, in order to induce a photothermal effect under the sunlight radiation exploited to recover sodium chloride from spent brines from SWRO plants via solar-driven PhMD-MCr.

The main goal of this study was to face and try to solve the high specific energy consumption of MD-MCr processes, that is hindering this technology in large scale application.

MMMs were prepared via NIPS by the preliminary dispersion of the nanoparticles into an environmentally friendly solvent (i.e., TEP) where the polymer (i.e., PVDF) was subsequently solubilized together with the pore-forming agents (i.e., PVP and PEG). In all the cases, membranes presented asymmetric structures based on a finger-like layer on a microporous spherulitic structure. The developed MMMs based on the embodiment of GO met the requirements for MD-MCr properties since they present porosity above to 70%, pore size in the order of 0.07-0.18 µm and contact angle superior to 96°. On the other hand, the poor dispersity of the CB negatively impacted on the porosity failing to 68% for CB10.

The solar radiation absorbed by the nanoparticles was effectively converted into heat: GO10 reached a surface temperature of 53 °C under 1 sun, while CB10 was heated up to 49 °C. In the case of the blank PVDF membrane the temperature under the sunlight radiation was just 31.2°C. As a result, the vaporization of the water increased with the temperature of the membrane surface and GO10 MMM secured an evaporation rate from SWRO brine of 0.910 L/m^{2}h, 2-folds higher than neat PVDF.

The membrane distillation was also employed for the treatment of naturally collected ground waters from Swedish former iron mines in order to compare the MD performances between real groundwaters, with the addition of high concentration of Lithium to emulate a typical Salar concentration, and a solution made of Lithium in R.O water. The goal of the current experimental session is to process via MD three different types of waters: (i) A Natural groundwater collected from an abandoned Iron mine near Stockholm; (ii) A hybrid water made of a natural groundwater artificially modified; (iii) A totally synthetic Li-containing groundwater.

The tested performances were similar in recovered water quality, with a conductivity of distillate in the range of 1.5 – 3.0 μS/cm, and permeate flux in the range of 2.0 – 7.0 L/m^2/h.

On the other hand, studying water recovery parameter, it emerged that the feed with R.O. water contaminated with Lithium shows higher values after ten hours of test with a final value of 20% higher than the other two experiments performed using natural water.

The thermal analysis confirmed a GOR value fluctuating between 2 and 5, confirming the thermal efficiency of the employed pilot-scale AGMD plant.

Chapter 3 – Photothermal Membrane Distillation-Crystallization

3.1 Introduction

An important part of daily-used products like additives, pharmaceuticals, fine chemicals, pigments and other items can be found in markets in crystalline form.

The quality of these products is a crucial parameter that needs to be guaranteed through the control of properties such as crystal morphology (shape, habit, average size, size distribution), structure (polymorphism) and purity (regular arrangement of the building blocks into the lattice).

It can be asserted that these properties have a considerable impact on the final employment of a crystalline product, in fact, for instance, polymorphism plays a primary role in pharmaceutical industry as the different polymorphic forms of the same substance display different physicochemical characteristics, so that each form can be considered like a specific material, different from the others, with significant consequences also on a legal point of view.

Although crystallization is playing a significant role in a wide range of scientific, technological, and industrial applications, current approaches still suffer of some limitations which affect both products quality and process efficiency. Poor reproducibility in the final crystals characteristics is the main limitation which is mainly associated with limited supersaturation control, imperfect mixing, reduced and inhomogeneous distribution over the plant of solvent removal or antisolvent addition points, reduced possibility to modulate the supersaturation generation rate; in addition, high energy requirements for heating in conventional evaporators or pumping in vacuum systems, represent additional limitations [35].

In this scenario, Membrane Crystallization (MCr) can be considered a valuable alternative to the traditional processes, exploiting all the advantages of membrane-based technologies that can be summarized in: i) Possibility to control the composition of crystallizing solution, level of supersaturation and its generation rate by tuning the mass transfer across the membrane; ii) Ability to affect solid features such as size, shape, polymorphic form and purity; iii) Easy scale-up and scale-down processes; iv) Reduced energy consumption with respect to cooling or evaporative crystallization[80].

MCr can be defined as a microscale interfacial technology based on the hybridization of MD and crystallization from solution and it has emerged in the last two decades as a promising alternative method to conventional evaporative crystallization [69].

In other words, MCr can be considered as an extension of MD over the saturation limits of the treated solution, with a consequent crystals nucleation and formation and, for this reason, it can be seen as a pioneering technology for the mining of Valuable Metals and Minerals from seawater and brines.

Moreover, this path permits to implement circular strategies on mineral recovery and reuse, exploiting the sea as a hypothetical unlimited mine and permits to solve the problem of shortage of raw materials.

Oceans and seas cover nearly three-quarters of the earth's surface and contain about 1.3×10^{18} t of water. They are composed of 96.7% water and 3.3% dissolved salts. This concentration of salts consists approximately 5×10^{16} t of salts which constitutes much more than most minerals that are available as land-based reserves and annually mined from lands. Almost all elements in the periodic table can be found in seawater although many are at very low concentrations and, in particular, the main ions which make up 99.9% of the salts in seawater in decreasing order are: $Na^+ > Mg^{2+} > Ca^{2+}$, $K^+ > Sr^{2+}$ (for cations) and $Cl^- > SO_4^{2-} > HCO_3^- > Br^- > BO_3^{2-} > F^-$ (for anions) [81].

The main pillar of this strategy consists in the improvement in valorization of Reverse osmosis brines (hypersaline solutions) coming from desalination plants through the direct recovery of minerals of industrial interest from these dehydrated and ultra-concentrated solutions.

This technique is evaluated as a complementary process for the treatment of hyper-concentrated brines generated from PhMD (Chapter 2) after an important volume of water removal and it is aimed to guarantee a preliminary mineral extraction before the selective recovery of Mg^{2+} via Donnan Dialysis treatment (Chapter 4).

MCr, just like MD, is based on the exploitation of hydrophobic microporous membranes capable of rejecting liquid water and dissolved salts and transporting the vaporized water molecules under the action of a moderate gradient of vapor pressure across the membrane, often generated by a temperature gradient. For this reason, these types of processes are not affected by concentration polarization and osmotic pressure [17] but, quite the opposite, they are mostly hindered by temperature polarization (TP) phenomenon.

The answer to TP proposed in this work consists in the addition of photothermal nanoparticles (NPs) in the membrane matrix, performing a light-to-heat conversion in plasmonic NPs irradiated at their resonance frequencies, that can be exploited for heat harvesting in MD.

Specifically, photothermal effects induce temperature increase at the boundary layer of the feed solution in contact with the membrane surface loaded with thermoplasmonic NPs, to facilitate the vaporization of the water molecules in MD experiments, thus overcoming the limitations related to the TP [17,27,28]. The photothermal efficiency (ηv) of membranes quantifies the effectiveness of the light-to-heat-to vapor conversion and it was estimated as:

$$J_v = \frac{J_W(\lambda_v+Q)}{P_{in}} \qquad (1)$$

where J_w is the flux of water vapor ($g \cdot m^{-2} \cdot s^{-1}$), λ_v the latent heat of vaporization of water ($J \cdot g^{-1}$), Q sensible heat of water ($J \cdot g^{-1}$), and P_{in} the power of the incident light ($W \cdot m^{-2}$), respectively.

The water evaporation flux (J_w), quantified through Eq. (2), is proportional to the difference between the vapor pressure of water at the membrane surface and the partial pressure of water vapor in air $(P_w^{membrane} - P_w^{air})$:

$$J_W = (P_w^{membrane} - P_w^{air}) \qquad (2)$$

The role of the photothermal nanofillers is to increase the driving force of the evaporation rate by raising the value of $P_w^{membrane}$, which is dependent, according to Raoult's law, on the vapor pressure of pure water p^0_w evaluated at the interface temperature of the irradiated membrane (T^*_f), the molar fraction (xw), and the activity coefficient (γ_w, ≠1 for a non-ideal mixture) of water in the feed solution. Moreover, p^{air}_w is affected by saturated water vapor pressure (p^0_w), evaluated at the actual dry bulb temperature (T^{air}), and relative humidity (ϕ).

Thus, J_w can be expressed as:

$$J_w = k\left[P_w^0(T_f^*)x_w\gamma_w - P_w^0(T^{air})\frac{\varphi}{100}\right] \qquad (3)$$

Regarding crystallization kinetic and according to the Classical Nucleation Theory (CNT), the impact of the membrane surface to facilitate the nucleation is quantified by the ratio of the Gibbs energy barrier for heterogeneous nucleation occurring at the membrane interface (ΔG^*_{het}) to the one for homogeneous nucleation occurring in the bulk of the solution (ΔG^*_{hom}), as following:

$$\frac{\Delta G^*_{het}}{\Delta G^*_{hom}} = \frac{1}{4}(2+cos\theta)(1-cos\theta)^2\left[1-\epsilon\frac{(1+cos\theta)^2}{(1-cos\theta)^2}\right]^3 \qquad (4)$$

Furthermore, the CNT describes the crystallization as a thermally activated process, where the nucleation rate (B) (the number of new crystals that are generated per unit of time per unit solution volume) is correlated to ΔG* (Gibbs energy barrier) by:

$$B = \Gamma e^{-\frac{\Delta G^*}{k_B T}} \qquad (5)$$

where Γ is the pre-exponential kinetic parameter and kB is the Boltzmann's constant, respectively. As described by the CNT, the nucleation rate B is associated to supersaturation S by the equation:

$$B = a\, e^{\frac{-b}{lnS^2}} \qquad (6)$$

where a is a pre-exponential factor and b is a constant.

The growth rate (R_G) is described by the following empirical correlation:

$$R_G = k_G(c - c^*)^g \qquad (7)$$

With k_G are the kinetic rate constant, g the growth rate order, c the actual salt concentration and c* the NaCl solubility, respectively [17].

MCr demonstrated to have the potential to recover dissolved salts with high purity level and freshwater form Reverse Osmosis seawater brines.

With this technology it was produced successfully NaCl or $MgSO_4$ $7H_2O$ crystals from artificial seawater RO brine with low crystal diameter coefficients of variation (CV) compared to the values generally obtained in conventional crystallizers (approximately 50% for NaCl) [10,12,24,81,82].

The low CVs are characteristic of narrow crystal-size distributions and, therefore, the crystals constitute a qualitatively better product.

There are evidence in literature of the employment of photothermal materials and NPs included in the polymeric membrane matrix as, for instance, graphene materials (2D-G and 3D-G) in PVDF for crystallization and recovery of NaCl, KCl and $MgSO_4$ $7H_2O$ with CVs in the range of 20-38%, below the value of 50% usually obtainable industrially [69].

MCr combined with plasmonic nanofillers have also been explored through the use of NiSe CoSe NPs synthetized via solvothermal approach on PDMS membranes with a crystallization of a high-quality NaCl characterized by a CVs near to 29% [17]. In this latter work, sunlight was converted heat with efficiencies up to 38% in case of NiSe NPs and 55% with the employment of CoSe NPs.

This chapter has been conceived as a natural prosecution of Photothermal Membrane Distillation (PhMD), experimenting a photothermal Membrane Crystalization (PhMCr) with the employment of Polyvinylidene Fluoride (PVDF) membranes prepared via Non-Solvent Induced Phase Separation (NIPS).

The photothermal effect was exploited to boost the vaporization of the water from SWRO brine up to the generation of the supersaturation conditions responsible for the nucleation and crystallization of Sodium Chloride (NaCl).

3.2 Materials and Methods – PhMD-MCr

Solar-driven PhMD-MCr experiments were conducted feeding distilled water or SWRO brine with a micro-peristaltic pump (Reglo, Ismatec, US) at a flow rate of 10 $mL \cdot min^{-1}$. The membrane (active area 3.14 cm^2) was positioned in a module of Polylactic acid (PLA) designed with Autodesk 123D®, printed using a 3D printer (model Tornado, TEVO, China) and equipped with a transparent window exposing the feed surface to the external radiation. During PhMCr test, the membrane module was irradiated by the light generated from a solar simulator (Abet Technologies, US) mimicking the sunlight spectrum with an irradiance of 1 sun (P_{in}=1000 $W \cdot m^{-2}$) over an area field of 35 mm of diameter.

The evaporation rate was periodically determined by weighing the feed using an analytical balance (Gilbertini, Model E 50 S/3). The temperature during the experiments was 25.8±0.5 °C and the relative humidity was maintained at 47 ±4 %. Experiments of solar-driven PhMD-MCr were repeated 3 times and the mean values of the water evaporation fluxes and the experimental errors were then calculated.

After the experiments, the obtained crystals were collected and examined under a Nikon industrial microscope (model Eclipse LV100ND, Japan). The cumulative function F(L) for the crystal size distribution was determined (population>100 crystals) and the coefficient of variation (CV) was calculated using:

$$CV = \frac{L84\% - L16\%}{2\,L50\%} \qquad (1)$$

where the crystal size (L) was obtained from the F(L) curve at a specified percentage (16%, 50% or 84%)[83].

3.3 Results – PhMD-MCr

After confirming the effectiveness of the photothermal effects with distilled water, MMMs were tested in sunlight-driven PhMD-MCr to extract salts and recovery water from SWRO brine.

Figure 3.1 reports the evaporation rates from SWRO brine as a function of the recovered water (%). In all the cases, the flux slightly increased in the early stage of the experiments because of the time required for the achievement of the steady state of the photothermal membrane-SWRO brine system. Then, J_w progressively decreased during PhMD-MCr experiments due to the gradual improvement of the concentration of the solutes by raising the recovered water. In fact, the partial pressure of the water in a solution ($p_w(T_f^*)$) depends on its molar fraction (x_w) and activity coefficient (γ_w) as described by the following equation:

$$p_w(T_f^*) = p_w^0(T_f^*) \cdot x_w \cdot \gamma_w \qquad (6)$$

Thus, the gradual dehydration of the brine lead to a coherent decrease of driving force due to a reduction of both x_w and γ_w. Just to give an example, the evaporation rate using GO10 decreased from 0. 910 L/m^{2}h to 0.800 L/m^{2}h after removing the 80% of the water from the brine.

Also, in the case of SWRO brines, the higher temperature of the photothermal membranes boosted the vaporization of the water. In fact, the higher J_w was observed for the MMM load with 10wt.% of GO (0.910 L/m^{2}h), more than 2-fold higher than the one observed for blank PVDF (0.446 L/m^{2}h) (see Fig 3.1). As expected, the reduction of the GO concentration from 10wt% to 2.5 wt% % provoked a reduction of the photothermal behavior with a consequent lowering of J_w from 0.910 L/m^{2}h to 0.740 L/m^{2}h. The lower photothermal efficiency of CB in comparison with GO lead to inferior J_w from the brine: CB10 membranes presented a maximum evaporation rate of 0.854 L/m^{2}h, close to the value observed for GO2.5 (0.740 L/m^{2}h). In all experiments, the progressive removal of water decreases its molar fraction (x_w in eq.6), which results in a reduction of J_w. This effect is more noticeable when initial fluxes are higher as observed for GO10 membrane, and it is amplified by the reduction of the activity coefficient with salt concentration of SWRO brine, whose activity coefficient reduces from an initial 0.97 to below 0.74.

Advantages of using a membrane with higher photothermal efficiency were observed in the reduction of the times required to induce the supersaturation of the brine and, as a consequence, the nucleation of the crystals. Crystals firstly nucleated on the surface of GO10 because of the rapid dehydration of the brine. With respect to GO10, nucleation time extended of 34% and 57 % for GO5 and CB10 respectively because of the lower transmembrane vapour fluxes. However, the poor evaporation rate from bare PVDF membranes delayed of more than 4-folds the time required for the appearance of crystal nuclei.

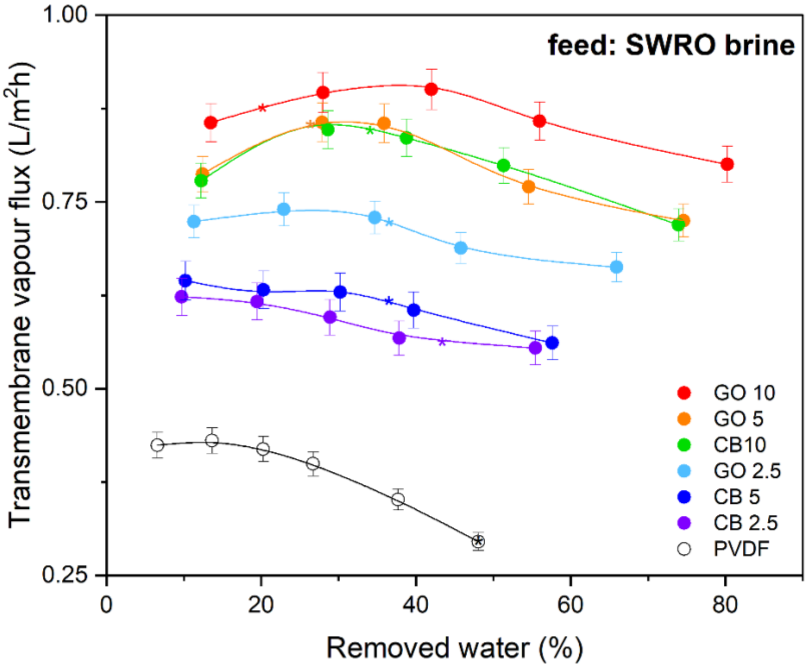

Figure 3.1 Evaporation rate from artificial SWRO brine in PhMCr under the solar radiation (* nucleation).

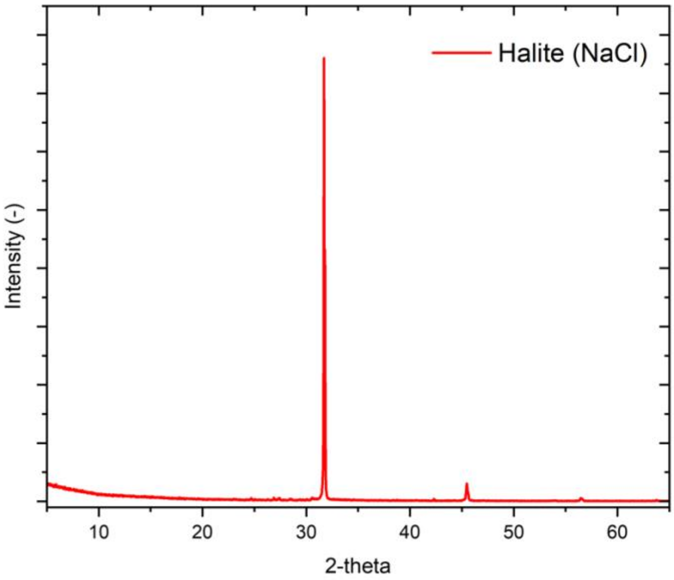

Figure 3.2 XRD pattern of crystals extracted from artificial SWRO brine in PhMD-MCr experiment performed with GO10.

The *post-hoc* inspection with the optical microscope of the membrane surface employed in PhMD-MCr experiments revealed the presence of crystals with a cubic structure, which is the characteristic morphology of NaCl. In fact, in accordance with the guidelines established by the Joint Committee on Powder Diffraction Standards (JCPDS), the crystal form is confirmed to be halite NaCl by diffraction peaks at 27.4°, 31.7°, 45.4°, 56.4°. Thus, the resulting XRD pattern emerging from Figure 3.2 shows the dominant presence of halite peaks (100% of the total) [84].

A wide variation in crystal size distribution was observed for crystals nucleated on bare PVDF membranes, evidenced by a large coefficient of variation calculated by the cumulative number distribution function, which reached 250%. This occurs when water slowly evaporates from solution, favoring the formation of a few initial crystals. Their slow growth combined with heterogeneity of the supersaturated environments lead to the appearance of crystals with widely varying sizes, inadequate for the industrial applications.

In contrast, the early onset of nucleation, promoted by the photothermal effect of CB and GO, provided to the nascent crystals more time to grow in well-controlled supersaturated environment. In fact, larger crystals were detected on the surfaces of photothermal MMMs with narrow distributions (Figures 3.3). Specifically, the average size of the final crystalline product was 497 µm and 583 µm on CB10 and GO10, respectively. In addition, the coefficients of variation of crystallized salts on CB-doped MMM tended to be larger than those observed for GO-based membranes. In fact, crystal growth on GO10 showed a lower dispersion of the size distribution around the mean value (CV= 60% for 10GO, CV=74% for 10CB). This was determined by the better dispersion of GO flakes into the PVDF resulting in a homogeneous membrane surface temperature profile that ensured standardized conditions for nucleation.

Likewise, the population density of crystals on GO10 (1862.02 crystals/cm^2) was 3-folds higher than that on PVDF bare and about +20% higher with respect to the observations on GO2.5 and CB2.5 membranes. This agrees with the Classical Nucleation Theory [85]: the boosted vaporization of the water on GO10 caused a facilitated nucleation with the consequent formation of a large number of small nuclei. Furthermore, the shorter nucleation time guaranteed to the nuclei a longer resilience time in a supersaturated solution promoting their growth. Thus, high concentration of GO assisted both the nucleation and the growth phases resulting in a facilitated extraction of minerals from SWRO brine by providing a homogeneous supersaturated environment. In fact, the ultimate result was that GO10 and CB10 membranes achieved a crystallization yield of 21-23%, more that 0.35-fold higher than blank PVDF.

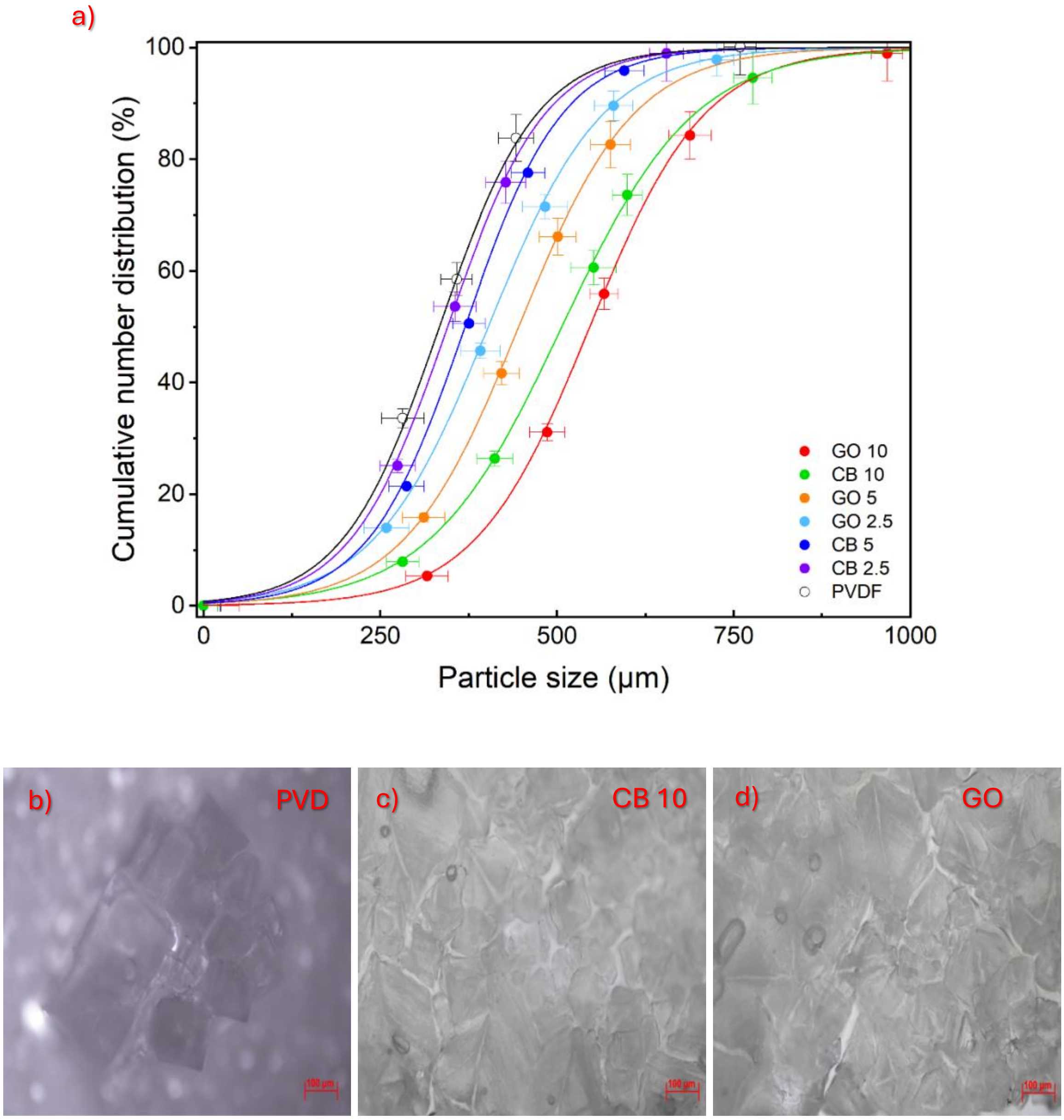

***Figure 3.3 (a)** Cumulative number distribution of crystals collected on the surface of membranes after PhMD-MCr; Microscopic images of crystals extracted on the surface of b) blank PVDF, c) CB10, d) GO10 after the experiments of PhMCr .*

3.4 Conclusions

In this chapter, the analyzed impacts of GO on the PhMD-MCr are in line with photothermal effects studied in chapter 2, as surface high evaporative flux facilitated the generation of supersaturation conditions. Therefore, GO10 outperforms the remaining membranes in terms of short nucleation time for NaCl from multi-ionic brine. This offered to the nucleated salts a longer resilience time in a supersaturated environment useful to promote their growth. Thus, the superior photothermal efficiency of GO10 secured a higher population density (1862.02 crystals/cm^2) of large crystals (583 μm). Interestingly, the facilitated dispersion of the 2D flakes enabled the generation of homogeneous conditions of the supersaturation resulting in crystals with a narrow pore size. In general, the benefits of the exploitation of 2D materials in the development of photothermal membranes was demonstrated, a technique exploitable in the implementation of circular approaches in the desalination via solar-driven PhMD-MCr.

Chapter 4 – Magnesium recovery from RO Brine

4.1 Introduction

Energy-water-raw materials nexus has received significant attention because of the development of the energetic crisis, the water stress and the depletion of ores [86]. The mining sector imposes an enormous pressure on this nexus with detrimental implications on the sustainable development [19]. Just to give an idea, the hydrometallurgical processes in the copper (Cu) and gold (Au) mining industries requires more than 10^9 m^3 per year of water [87] while more than 40 kWh are required for the extraction of one kg of magnesium (Mg) via molten salt electrolysis or thermochemical Pidgeon batch processes[88]. Unquestionably, the modernization of the mining industry and the implementation of circular practices are fundamental to mitigate the energy-water-raw materials nexus and to satisfy the growing need of minerals [89].

Under the impulse of the blue economy, the seas and the oceans will play a decisive role in this crucial challenge being unlimited sources of minerals and water [81]. In this scenario, well-established and emerging membrane technologies have gained momentum in the blue growth. Reverse Osmosis (RO) is the state-of-the art desalination technology covering the 69% of current global desalination capacity ($97\cdot10^6$ $m^3\cdot day^{-1}$) [90]. Noteworthy, the main advantage of RO is the low specific energy consumption (3–6 $kWh\cdot m^{-3}$) in comparison to thermal-based desalination process (10–15 $kWh\cdot m^{-3}$) [91]; while the critical drawback is the low recovery factor limited to ca. 50% by the increasing of the osmotic pressure with the salinity of the rejected streams [92]. The ultimate result is that every day more than $40\cdot10^6$ m^3 of hyper concentrated brine (salinity>50 $g\cdot L^{-1}$) are directly disposed into the sea from RO plants with a remarkable environmental impact [93][94]. In this contexts, innovative membrane techniques aiming to reduce the volume of RO brines by raising the water recovery factor and to extract dissolved salts represent an interesting opportunity towards sustainability [3], in a logic of Circular Approach and Process Intensification.

Mg is one of the major cations in seawater and its mining from brine is of economic relevance since it has been recently included in the Critical Raw Materials by the European Community due to its relevant role in different industrial sectors, as well as its potentialities as substitute of Li in battery field. [6,7].

In literature there is evidence of trials aimed to the removal of Mg from wastewaters, RO brine and seawaters through processes and technologies as chemical precipitation [95,96], electrochemical precipitation [97,98], Electrolysis [99,100], Electrodialysis [101], Adsorption techniques [102], Nanofiltration (NF) [103] and RO techniques [104,105].

Nevertheless, the direct extraction of Mg from brine is still allusive because of its low concentration (ca. 0,1 M) [23] imposing the need of an additional stage of concentration. With respect to this, Membrane Distillation (MD) is an attractive process having the potentialities to intensify the desalination up to a water recovery factor of 90% [13] [24]. However, temperature polarization (TP) phenomena put a strain on the water-energy nexus in MD operations raising the specific energy consumption to values above 100 $Kwh \cdot m^{-3}$ [22].

Among the techniques of the membrane extraction, Donnan Dialysis (DD) stands out thanks to the low energy consumption, low fouling tendency, high simplicity and minimal operating costs being the process not driven by electricity or pressure gradients [106] [46] [40].

In fact, the mechanism of transport in DD is based on the electrochemical potential gradients across an ion-exchange membrane (IEMs) driving the spontaneous and selective ion permeation from a feed to a draw solution [39].

In the case of Cation Exchange Membranes (CEMs), the transport of cations is allowed whereas the permeation of co-ions is hindered due to the electrostatic exclusion (referred as Donnan exclusion) from the membrane phase and, simultaneously, cations from the draw solutions diffuse through the membrane to maintain electroneutrality in both solutions [41].

This process has been employed to study the removal of Ca and Mg ions from water samples with the use of PVDF membrane modified with polyaniline, poly-n-etylaniline, poly-n-metylaniline and poly-o-anisidine doped with1,3 (6 or 7)-napthalenetrisulfonic acid (NTSA) through acidic solution as draw solution ([39]) or using Neosepta standard-grade CMX, and standard-grade Type II CEMs FUJIFILM with saline solutions as strip observing a reduction of divalent cation content in feed between 76 and 90 % phase [42] [43] [44]. Similarly, DD was explored as a separation process aimed to tap water softening, operated with a stripping solution made of NaCl with a removal efficiency around 75% [45]. With the same membranes, Marzouk et al. studied the removal of Ca and Mg through DD from Tunisian dam, lake, and tap water according to the Doehlert design with a Mg removal efficiency around 90% [46]. Agarwal in 2012, measured the transport rate of ions across Nafion-117 ion-exchange membrane in a DD process for mono–monovalent (Na^+ – Cs^+) and mono–bivalent (Na^+ – Ba^{2+}, Na^+ – Mg^{2+}) ion-exchange process for different salt concentrations with removal efficiencies up to 44% [47].

Mg recovery from seawater and RO rejected brine has been also studied in terms of $Mg(OH)_2$ with a purity between 93% and 95% and MgO (purity of 98%) via addition of ammonium hydroxide ($(NH_4)OH$) and sodium hydroxide (NaOH) as precipitating agents [107][108][109][110] respectively.

La Corte in 2020, worked on an ion exchange membrane crystallizer (CrIEM), that combines reactive and membrane crystallization with Anion Exchange Membrane (AEM) in order to recover high purity MgOH from multi-component artificial and natural solutions with a Mg recovery efficiency between 90-100 % in combination to a solid purity around 97% [111] and, similarly, Mohammad investigated a process based on the precipitation of MgOH by the reaction of magnesium carbonate ($MgCO_3$) in the brine with $(NH_4)OH$ with a maximum recovery of 99% at a temperature of 15°C and a brine salinity of 85 $g \cdot L^{-1}$ [112].

The innovative strategy of this chapter is a novel and integrated membrane process (Figure 4.1) aimed to the extraction of Mg from brine based on: i) NF to separate the brine into mono- and multivalent streams; ii) solar-driven PhMD to dehydrate up to a concentration factor of 3.5 the multivalent-rich retentate phase (performed in chapter 2); ii) DD to selectively extract the Mg from hypercontracted retentate of solar-driven PhMD to the stripping phase and iv) recovery of $Mg(OH)_2$ from the stripping phase via reactive batch precipitation with the addition of NaOH.

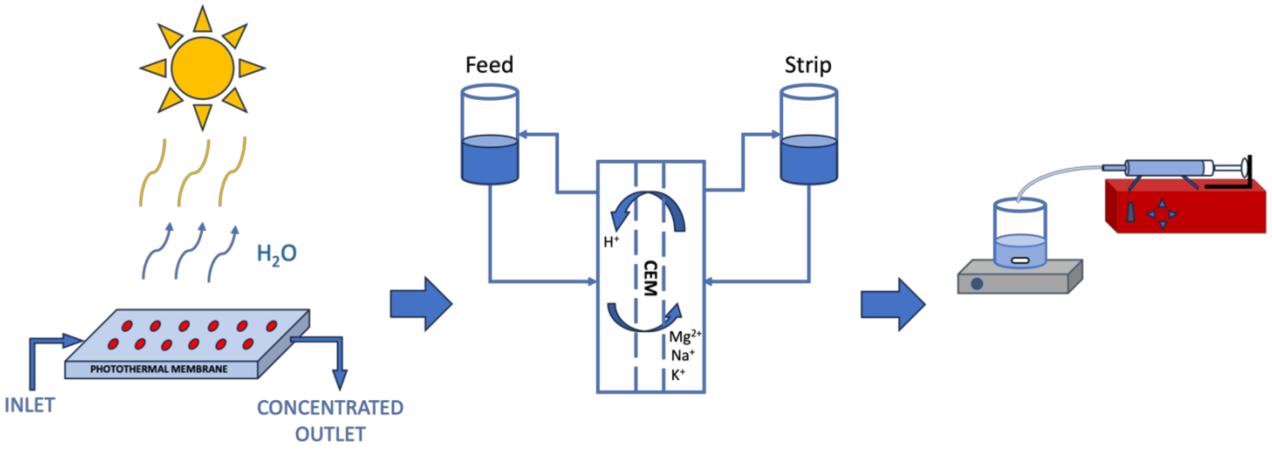

Photothermal MD

Donnan dialysis for selective mineral extraction

Reactive precipitation of $Mg(OH)_2$

Figure 4.1 Concept of selective mineral extraction from R.O. brines.

4.2 Materials and methods

4.2.1 Ion Exchange Crystallizer – Donnan Dialysis (DD)

Artificial feed solutions, whose ionic composition is reported in Table 4.1, where prepared by dissolving $MgSO_4{\cdot}7H_2O$, $MgCl_2{\cdot}6H_2O$, NaCl and KCl (all purchased from Sigma Aldrich, Italy) in deionized water (5.5 $\mu S{\cdot}cm^{-1}$) produced by PURELAB (Elga LabWater, UK). Draw solutions (0.1M/0.25M/0.5M HCl) were prepared by dissolving appropriate amount of hydrochloridic acid 37% (Sigma Aldrich, Italy) in deionized water.

Table 4.1 Composition of artificial feed solutions tested in DD.

Feed code	**$MgSO_4{\cdot}7H_2O$ (M)**	**$MgCl_2{\cdot}6H_2O$ (M)**	**NaCl (M)**	**KCl (M)**
F1	0.502	-	-	-
F2	-	0.372	-	-
F3	-	-	3.877	-
F4	-	-	-	0,09
F5	0.502	0.372	3.877	0,09

Commercial CEM TYPE 1 supplied by Fujifilm Manufacturing Europe B.V. (The Netherlands), with ion exchange capacity of 2 meq/g and permselectivity of 92%, was inserted in a 3-D printed cross-flow cell in Nylon with active membrane area of 120 cm^2 (Figure 2.a-b). Specifications of employed CEM are summarized in Table 4.3 [113].

Table 4.3 Technical specifications of employed CEM.

CEM type	FUJIFILM TYPE 1
Ion Exchange Matrix	Polyamide
Fixed groups	Sulfo group $-SO_3^-$
Exchange capacity	2.23 ± 0.02 meq/g
Thickness	121 ± 1 μm
Water uptake	54.9 ± 1.4 %
Charge density	3.6 ± 0.27 mol/L

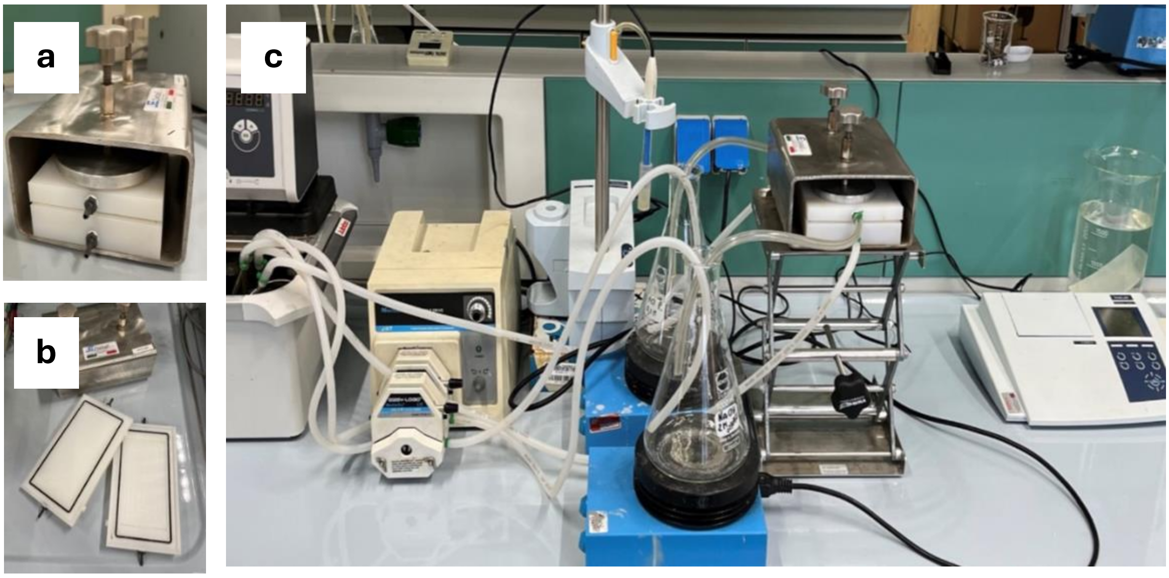

Figure 4.2 a) Cross-flow DD cell inserted in stainless steel housing; **b)** half-cells; **c)** Donnan Dialysis (DD) lab-scale plant.

Feed and draw solutions, both with initial volume of 1 liter, were supplied to the module in counter-current flow by Masterflex peristaltic pump with n.2 Easy-Load L/S heads (Cole Parmer, US) with flowrate of 0.2 L/min at 25°C. The lab-scale setup is shown in Figure 6.c. During each test, the evolution in time of pH at retentate side was monitored by WTW™ inoLab™ pH Benchtop Meter (Thermo Fisher Scientific, US). The duration of each batch test was 7 hours. The concentration of Na^+ and Mg^{2+} ions was determined by Atomic Absorption model HR-CS AAS ContrAA 700 (Analytik Jena AG, Germany).

4.2.2 Ion Exchange Crystallizer - Reactive Precipitation of $Mg(OH)_2$

Reactive precipitation tests were carried out at 25°C on 200 mL of artificial solutions (ion concentration in Table 4.2) mimicking: i) retentate stream from Photothermal Membrane Distillation (PhMD) as benchmark; ii) draw stream from Donnan Dialysis (DD) unit; iii) retentate stream from DD unit.

Table 4.2. Ion concentration of tested artificial solutions

Species	PhMD retentate	DD draw	DD retentate
Na^+ (mg/l)	89 131	7 840	71 160
Mg^{2+} (mg/l)	21 253	410	18 020
Cl^- (mg/l)	163 865	21 100	141 260
SO_4^{2-} (mg/l)	48 222	/	41 570
pH	7.3	0.39	0.14

The alkaline precipitant solution (2M NaOH), obtained by dissolving anhydrous NaOH pellets (Carlo Erba Reagents, Italy) in deionized water (5.5 µS·cm^{-1}) produced by PURELAB (Elga LabWater, UK), was added dropwise – under continuous stirring – by a syringe pump Model NE_1000 (New Era Pump Systems Inc., US) set at flowrate of 7mL/min. During the test, the evolution in time of pH (WTW™ inoLab™ pH Benchtop Meter, Thermo Fisher Scientific, US) and conductivity (WTW™ inoLab™ Conductivity Benchtop Meter Thermo Fisher Scientific, US) was monitored on-line and registered every 7 mL of alkaline solution added. The lab-scale setup is shown in Figure 3.

Figure 3. Lab-scale setup for reactive precipitation of $Mg(OH)_2$.

At the end of each test, the solution was decanted for 24 hours; then, the solid phase was filtered and dried overnight in oven at 70°C for characterization analysis (ongoing).

4.3 Results and discussion

4.3.1 Donnan Dialysis

The employed DD process is a technique where the ion exchange (i.e. ions recovery) is reached by the selective passage of cations through a CEM, that separates the Feed compartment (i.e. donor compartment with high concentration of target ion) and the Strip compartment (i.e. receiver compartment with high concentration of exchange ions) as exemplified in Figure 4.4.

Fuji-Film CEM Type 1 membranes were obtained from Fujifilm Manufacturing Europe B.V. (The Netherlands). Those membranes are specifically designed for high Mg^{2+} permeation and consist in aliphatic polyamide ion exchange matrix functionalized by sulfo groups ($-SO_3^-$), reinforced through a hydrated polyolefin support [113,114].

Donnan equilibrium theory is based on electrochemical potential equilibrium and ion transport equilibrium. The first of these states that the electrochemical potential of ions separated by an ion exchange membrane in a two-cell Donnan reactor will be identical at equilibrium, and, on the other hand, the second states that electroneutrality on both sides of the same cell must also prevail at equilibrium [40].

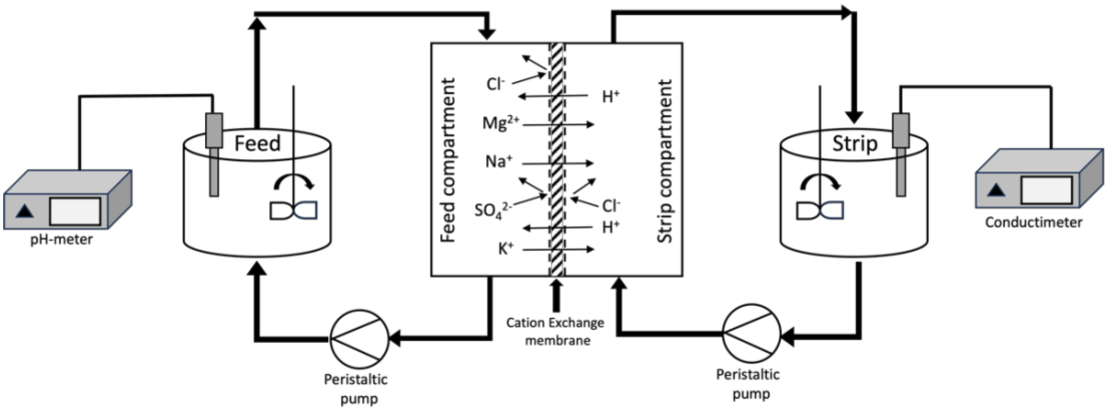

Figure 4.4 Scheme of the employed Donnan dialysis process.

Transport across the membrane continues until the electrochemical potential difference across the membrane is equal to the Donnan potential of the membrane. At this point, Donnan equilibrium across the membrane is reached and the solutions are in equilibrium and no more transport will thus occur. The potential difference (E) across the membrane for a species i can be described by the following equation:

$$E = \frac{RT}{F}\ ln\left(\frac{a_{i,R}}{a_{i,F}}\right)^{1/z_i} \qquad (5)$$

where R is the gas constant (J mol^{-1} K^{-1}), T is the absolute temperature (K) and F represents the Faraday's constant (C mol^{-1}). The two terms $a_{i,R}$ and $a_{i,F}$ are the activity coefficients of electrolyte i in the receiver and feed solution respectively and z_i can be identified as the ionic valence of specie i [115]. The activity coefficients $a_{i,R}$ and $a_{i,F}$ can be computed using Raoult's law and can be considered proportional to the specie i concentration in the solution.

The Donnan membrane equilibrium principle stats that the ratio of equilibrium concentration of the counter-ions in the solutions in the two compartments is given by:

$$\left(\frac{C_{A,feed}}{C_{A,receiver}}\right)^{1/z_A} = \left(\frac{C_{B,feed}}{C_{B,receiver}}\right)^{1/z_B} \qquad (6)$$

where C_A and C_B refer to the concentration of A and B species at equilibrium and z_A and z_B are the respective charges on the two ions [116]. In other words, Donnan stated that the electrochemical potentials in aqueous and membrane phase are equal for each ion.

To satisfy electroneutrality requirements, the rate of target ion removal from the feed solution must be equal to the rate of draw ion removal, considering the charge equivalents, from the strip solution:

$$\sum_{i(or\ j)}\left(z_{i(orj)}\ C_{i(orj)}^{feed\ or\ strip,bulk}\right) = 0 \qquad (7)$$

$$\sum_{i(or\ j)}\left(z_{i(orj)}\ C_{i(orj)}^{feed\ or\ strip,mem}\right) = 0 \qquad (8)$$

The electroneutrality condition imposed through eq. 7 and eq. 8 has to be always satisfied both at the solutions bulk and at the membrane-solution interface on the two sides [117].

Ion transport through the membrane can be described by Fick's diffusion and electromigration law under the conditions of thermal equilibrium, absence of resistance to mass transfer in the bulk solutions, no mass transfer limitations in the liquid film layers at the membrane-solutions interfaces, absence of co-ion transport in the membrane and absence of osmotic effects [106].

Transport of ions through an ion exchange membrane is generally described by the Nernst–Planck equation:

$$J_i = -D_{m,i}\left\{\frac{dc_{m,i}}{dx} - z_i c_{m,i}\frac{F}{RT}\frac{dE}{dx}\right\} \qquad (9)$$

where J and $c_{m,i}$ are the flux and the concentration of ions in the membrane, $-D_{m,i}$ is the diffusion coefficient, z_i is the ionic charge, E is the electrical potential field gradient, x is the distance in the membrane, F is the Faraday constant, R is the gas constant, and T is absolute temperature of the system [116,118,119].

HCl was selected as stripping agent thanks to his strong acid nature, which allows him to totally dissolve in water with the subsequent release of an easily known amount of driving ions (i.e. H^+) [[120]:

$$HCl_{(aq)} \rightarrow H^+{}_{(aq)} + Cl^-{}_{(aq)} \qquad (10)$$

4.3.1.1 Single-ions feed tests

Figure 4.5.a-d shows the evolution in time of Mg^{2+}, Na^+ and K^+ concentration in the draw solution at different HCl concentration. Coherently with mass transport phenomena driven by diffusion, the ion transfer rate increases at increasing HCl concentration: for feed solutions F1 and F2, 2.8 and 2.2-fold enhancement were observed when increasing acid molarity from 0.1 to 0.5M, respectively.

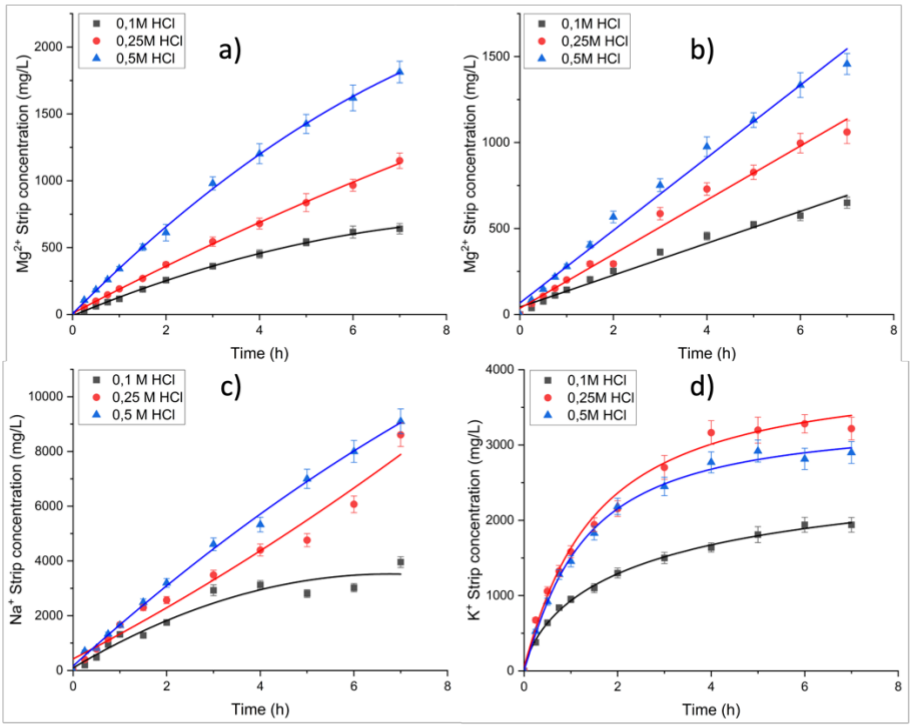

Figure 4.5 Ion concentration evolution in time for feed solution: **a)** F1; **b)** F2; **c)** F3; **d)** F4.

This behavior at increasing strip concentration can be assumed strictly related to the simultaneous increasing of electrochemical potential E of stripping ions (H^+) defined by Eq 5, which brings to an increment of the term $z_i c_{m,i} \frac{F}{RT}\frac{dE}{dx}$ in eq 8, bringing to an enhancement of ions exchange through the CEM.

At 0.5M HCl, the higher molar concentration $c_{m,i}$ of Mg^{2+} in F1 (0.502M) than in F2 (0.372M) resulted in a higher ion transfer flux J_i (eq 9) (F1: 0.89 mol/m^{2}h; F2: 0.71 mol/m^{2}h); this effect appeared negligible at lower HCl concentration because of the decreased value of electrochemical potential E of draw ion at the lowest concentration, resulting in a decreased ion exchange capacity.

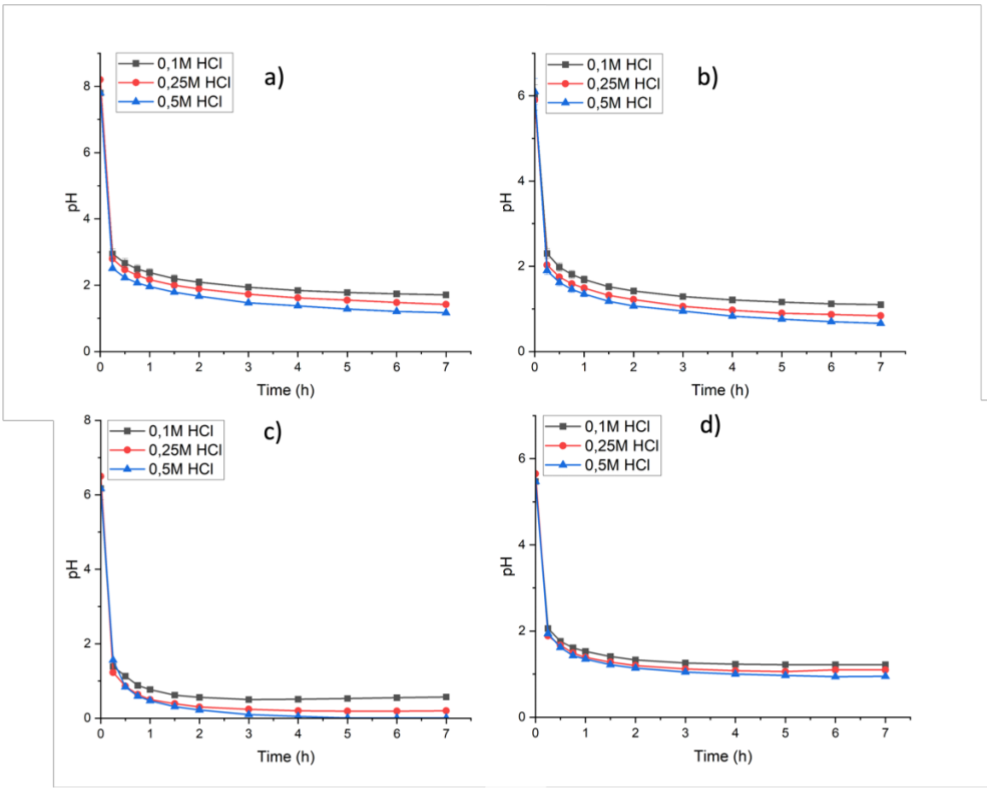

Figure 4.6 Evolution in time of pH for single salts feeds: **a)** F1; **b)** F2; **c)** F3; **d)** F4.

For solution F3, experimental data on NaCl diffusion through CEM – reported in Figure 4.5.c - revealed a significant Na^+ transfer rate, thus anticipating a strong interference on the transport of Mg^{2+} mainly produced by the 288% and 420% increased cation concentration in F3 compared respectively to F1 and F2, bringing to an increase of the driving force of the process.

Diffusional rate of Na^+ as a function of HCl concentration exhibited an analogous trend with respect to Mg^{2+}: a 2.3-fold enhancement was found when increasing acid molarity from 0.1 to 0.5M. For 0.5M HCl draw solution, Na^+ transfer rate was 4.7 mol/m^{2}h. In all cases, the decreasing profile of pH registered in the retentate compartment (Figure 4.6. a-d) confirms the exchange of Mg^{2+} and Na^+ with hydrogen ions, reaching increasingly low values with the increasing of Acid concentration in Strip side.

Concerning F4 (Figure5.d), the behavior showed in this set of experiments is not in compliance with F1, F2 and F3, highlighting a slightly higher concentration (≈ 8%) in strip phase of K^+ working with 0.25M HCl compared to values obtained in 0.5M HCl test. The 0.1M HCl test follows the trend observed in the other three sets showing concentration values ≈ 40% lower with respect to intermediate HCl concentration test.

The physical explanation to the previous-cited reversed trend can be identified in the low concentration of target ion (K^+) in the initial feed F4, which brings to a decreasing of driving force of ions flux through CEM.

Mg^{2+} Fluxes observed in this experimental work are comparable with values that can be found in literature, for instance in Zhong et al work [121], where magnesium was recovered using HNO_3 as stripping agent at different concentration (1-5M) and through the employment of Nafion membranes as CEM.

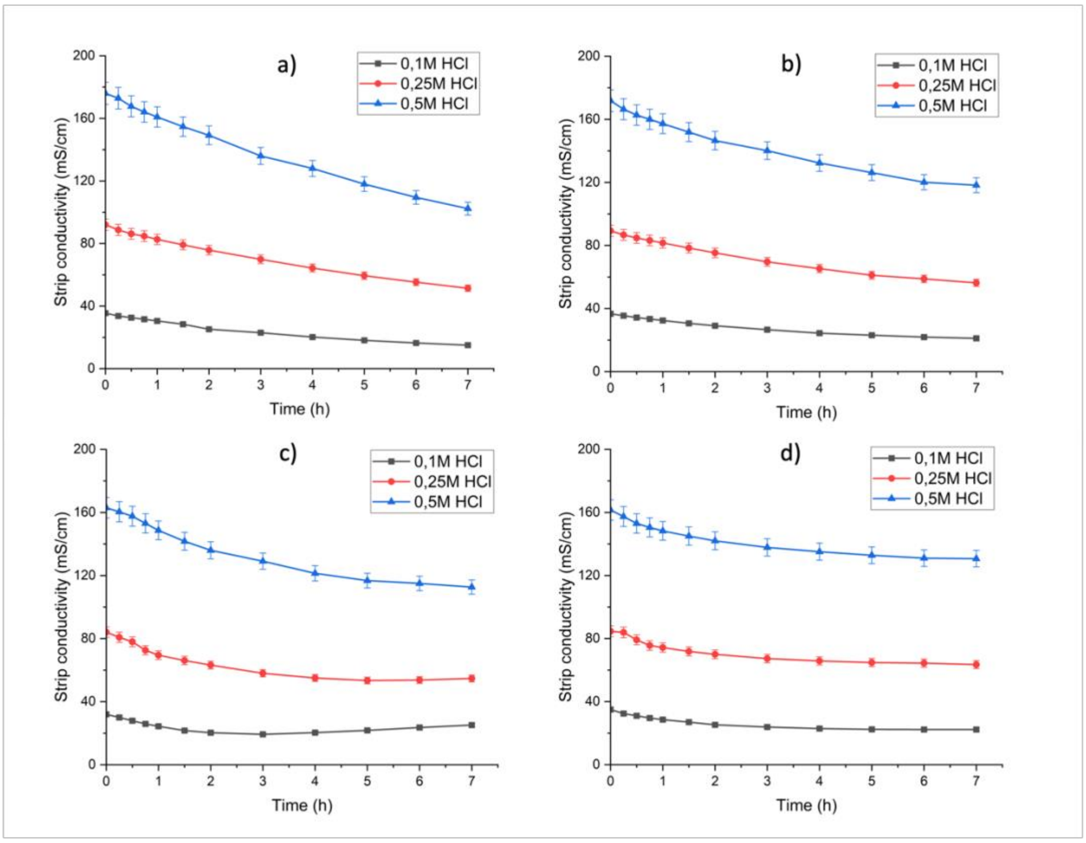

Figure 4.7 Conductivity trends in Strip compartment in single salts Feed tests: **a)** F1; **b)** F2; **c)** F3; **d)** F4.

In Figure 4.7.a-d it is proposed the conductivity trend of draw solutions in tests with single salts feeds, highlighting a common trend in all the four sets of experiment. The behaviour of strip conductivity showed a decreasing trend, simultaneously with ions exchange through CEM, in all the performed tests and during the entire experimental span.

The higher HCl concentration in strip brought to more emphasized negative variations of conductivity; in detail, largest variation was recorded in F1 test at 0.1M HCl (≈58%) and the most negligible one was observed in F4 test with 0.5M HCl strip solution (≈19%).

4.3.1.2 Multi-ions feed test

Figure 4.8.a illustrates the evolution in time of Na^+, Mg^{2+} and K^+ ion concentration within the draw compartment for F5 feed solution.

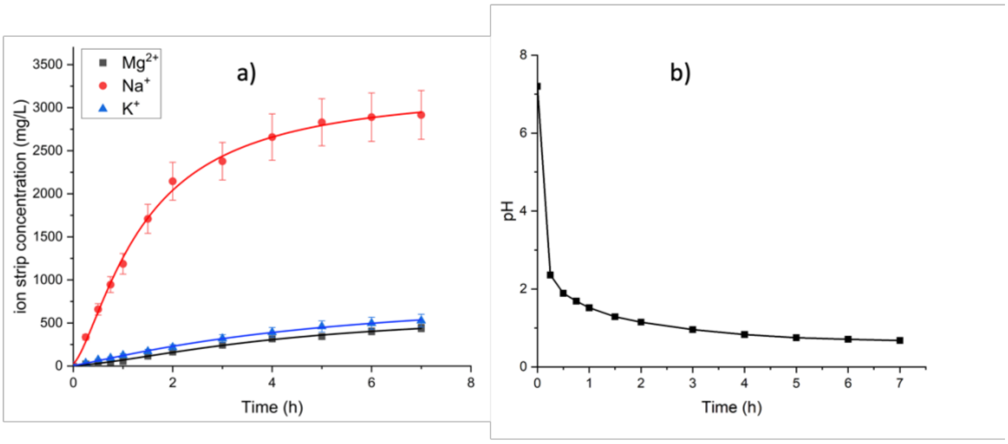

Figure 4.8 Evolution in time of: **a)** concentration profiles of Na^+, Mg^{2+} and K^+ in **F5** draw solution; **b)** pH in **F5** retentate solution.

The ion transfer rate from retentate to draw side remains constant over time (Na^+: 3.4 mol/m^{2}h; Mg^{2+}: 0.17 mol/m^{2}h) and emphasizes the ability of CEM to preferentially remove the monovalent ion. With respect to DD tests with single salts, the ion transfer rate for Na^+ and Mg^{2+} decreased by 27 and 78%, respectively.

Generally, ion flux and ion selectivity of the membrane reflects innate differences in the diffusional velocity and binding strength of the exchanging ions. Assuming that ions are present in the system at similar concentrations, trans-membrane diffusion of the ions will depend on the valence and size of the individual ions. Ions of higher valence tend to hydrate more strongly, are bigger, and thus diffuse more slowly. Within the membrane, the diffusion of these more highly charged ions is further hindered by electrostatic interactions with the membrane functional groups. The binding strength is the other factor that dictates membrane selectivity and in general polyvalent cations bind more firmly to cation exchange binding sites than do mono- or divalent cations. Cations of similar charge are preferentially attracted on the basis of their electronegativity and for strong cation exchangers (in our case $-SO_3H$) the order of binding strength for the cations of interest is given as [40]:

$$Mg^{2+} > Na^+ > H^+$$

In our case, the preferential removal of the monovalent ion is due to its higher concentration in Feed phase in comparison to the bivalent one, creating a discrepancy in terms of driving force of ionic flux for each cation investigated.

Overall, the mass reduction of Na^+ and Mg^{2+} in the retentate is 7.4 and 1.6%, respectively, resulting in a 4.6-times enrichment with respect to the divalent cation. Due to osmosis, a significant flux of water (1.9 L/m^2h) from draw solution to retentate is observed, resulting in a final draw volume reduction to 0.84L.

The exchange of H^+ with Na^+ and Mg^{2+} is confirmed by the decrease of pH in the retentate solution (Figure 4.6.b): from the initial value of 7.2, a drastic decrease to ≈1 is observed within the first 30 minutes, then furtherly reducing to ≈ 0.2 at the end of the test.

4.3.1.3 MATLAB simulation of Donnan dialysis multi-ions feed treatment

The multi-ions Feed treatment has been also simulated with the employment of MATLAB, using eq. 5-14 to compute fluxes across CEM and final concentrations of H^+ in Feed, Na^+ and Mg^{2+} in Strip. In Table 4, fixed parameters employed in the simulation are summarized.

A one-dimensional (1-D) finite difference discretization approach (Figure 4.9) was used to address the differential mass balance equations in the Donnan cell along the channel length. Mass balance equations were solved assuming negligible axial and radial diffusion and can be schematized as follow:

$$\frac{dF_{feed}}{dx} = J_w\,W \qquad (11)$$

$$\frac{dF_{strip}}{dx} = -J_w\,W \qquad (12)$$

$$\frac{dc_i^{feed}F_{feed}}{dx} = \pm\,J_w\,W \qquad (13)$$

$$\frac{dc_j^{strip}F_{strip}}{dx} = \pm\,J_w\,W \qquad (14)$$

where F_{strip} and F_{feed} are the flow rate of the acid and brine solutions [m^3/s], respectively; J_w is the water flux through the membrane [m^3/m^2s]; W is the channel width [m]; c_j^{strip} and c_i^{feed} are the concentration of the *j*th and *i*th species in the acid and brine solution [mol/m^3], respectively [117].

Table 4. Model parameters	
D_{m,H^+}	9.3e-9 m^2/s
D_{m,Na^+}	1.3e-9 m^2/s
$D_{m,Mg^{2+}}$	0.705e-9 m^2/s
F	96405 C/mol
T	298 K
R	8.21e-5 m^3 atm K^{-1} mol^{-1}
A_m	12 cm^2

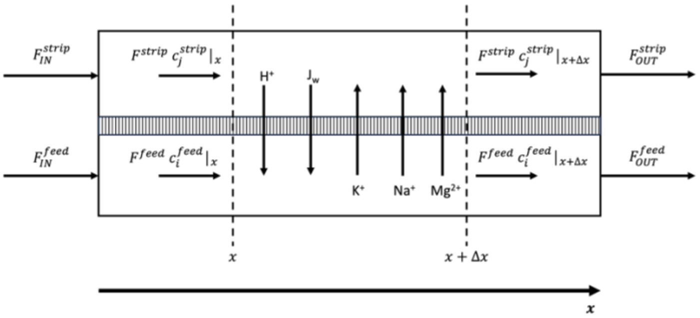

Table 4.4 Model parameters employed in MATLAB simulation (left); **Figure 4.9** Schematization of one-dimensional (1-D) finite difference discretization approach in Donnan simulation (right).

The volume variation in both retentate and diffusate, respectively Figure 4.10.a-b, is due to the water flux across the membrane that is directed from the less concentrated solution to more concentrated one and it has been mathematically modelled considering two main contributions: osmotic and the electro-osmotic flux:

$$J_w = P_{os}\Delta\pi + \sum_k \beta_k J_{m,k} \qquad (15)$$

Where P_{os} is the water permeability of the membrane [$m^3/(Pa\ m^2\ s)$], $\Delta\pi$ is the difference of osmotic pressure between the two channels [Pa] and k refers to the hydration number of the ions. The osmotic pressure was calculated using the van't Hoff equation in which osmotic coefficients were considered to be unitary [117].

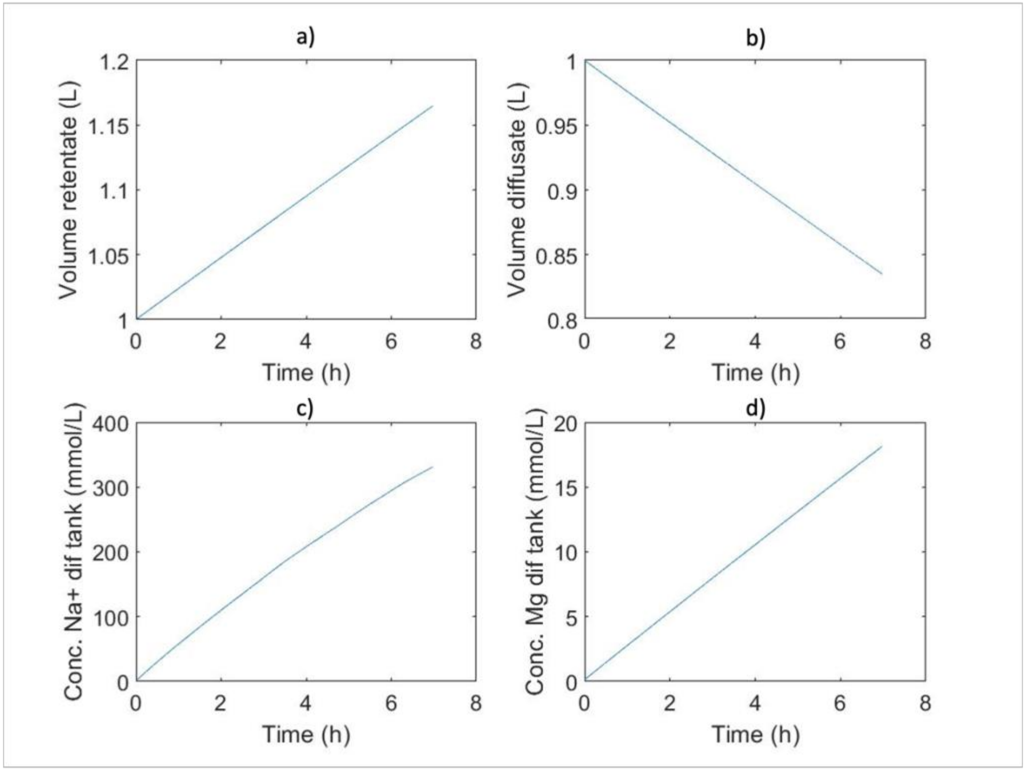

Figure 4.10 Matlab simulation of Donnan Dialysis process of four different parameters: **a)** Volume of retentate (Feed); **b)** Volume of diffusate (Strip); **c)** Na^+ concentration in Strip; **d)** Mg^{2+} concentration in Strip.

Simulation of osmotic flux J_w was realistic, giving a final feed volume 6% higher and a final strip volume 4% lower compared to the real volumes observed at the end of the test.

Simulated trends of Na^+ and Mg^+ concentration in strip validate experimental values obtained in lab-scale Donnan plant, highlighting a 1% higher value in the case of Magnesium compared to experimental value.

The preferential Na^+ exchange over Mg^{2+} ions across the membrane is widely confirmed also in the MATLAB simulation, with a computed concentration of Na^+ in strip phase ≈7600 mg/L, more than the double of the value detected empirically.

4.3.1.4 Mass balances

At the end of each test, it has been performed a material balance taking in count the amount of ions collected in the samples for analytical purposes by means of their analyzed concentration and the volume collected.

The balance employed for each i cation was:

$$IN - OUT + TRANS = ACC \qquad (16)$$

In our case there are no reaction involved in the process and consequently the TRANS term can be considered null. Also, ACC term should be considered null due to the absence of accumulation phenomena inside the two-cells Donnan reactor.

The eq 16 becomes:

$$m_{i,0}^{feed} = m_{i,f}^{feed} + m_i^{strip} + m_i^{samples} \qquad (17)$$

With a further development of the terms eq 17 becomes:

$$C_{i,0}^{feed}\, V_0^{feed} = C_{i,f}^{feed}\, V_f^{feed} + C_{i,f}^{strip}\, V_f^{strip} + \sum_{x=1}^{n} C_{i,x}^{feed}\, V^{sample} + \sum_{x=1}^{n} C_{i,x}^{strip}\, V^{sample} \qquad (18)$$

where $C_{i,0}^{feed}\, V_0^{feed}$ is the amount of ion i in the initial feed at t=0, $C_{i,f}^{feed}\, V_f^{feed}$ and $C_{i,f}^{strip}\, V_f^{strip}$ represent the mass of ion i at the end of test in feed and strip respectively.

Terms $\sum_{x=1}^{n} C_{i,x}^{feed}\ V^{sample}$ and $\sum_{x=1}^{n} C_{i,x}^{strip}\ V^{sample}$ include the total mass of ions taken out through collection of n samples. V^{sample} was the volume collected for analytical purposes and it was kept constant at 0.01 L for all the samples.

Error percentage in material balances was computed comparing the initial known mass of ions i in the feed with the total ions mass detected analytically in all the streams and sample through eq 13:

$$\varepsilon\ \% = \frac{C_{i,0}^{feed}\ V_0^{feed} - (C_{i,f}^{feed}\ V_f^{feed} + C_{i,f}^{strip}\ V_f^{strip} + \sum_{x=1}^{n} C_{i,x}^{feed}\ V^{sample} + \sum_{x=1}^{n} C_{i,x}^{strip}\ V^{sample})}{C_{i,0}^{feed}\ V_0^{feed}} * 100 \qquad (19)$$

Material balances showed an error percentage ε lower than 10% in all the performed Donnan dialysis tests, thus confirming the reliability of employed lab-scale dialysis plant and analytical techniques.

4.3.2 Reactive Precipitation of $Mg(OH)_2$

The reactive precipitation process was experimentally investigated by monitoring the evolution of pH and ionic conductivity as a function of the amount of precipitant added.

As Precipitant agent it was selected 2M NaOH solution, that, after reaching saturation point, was expected to precipitate Mg^{2+} under the form of $Mg(OH)_2$ following the reaction:

$$Mg^{2+}{}_{(aq)} + 2OH^{-}{}_{(aq)} \rightarrow Mg(OH)_{2(s)} \qquad (20)$$

Magnesium recovery via precipitation process can be considered a natural consecution of DD, where Mg extraction takes place. Before the experimental approach, it is important to analyze a simulation of the process, correlating mols of the precipitated solids and pH of the solution with the progressive addition of the precipitant solution (2M NaOH) as showed in Figure 11.

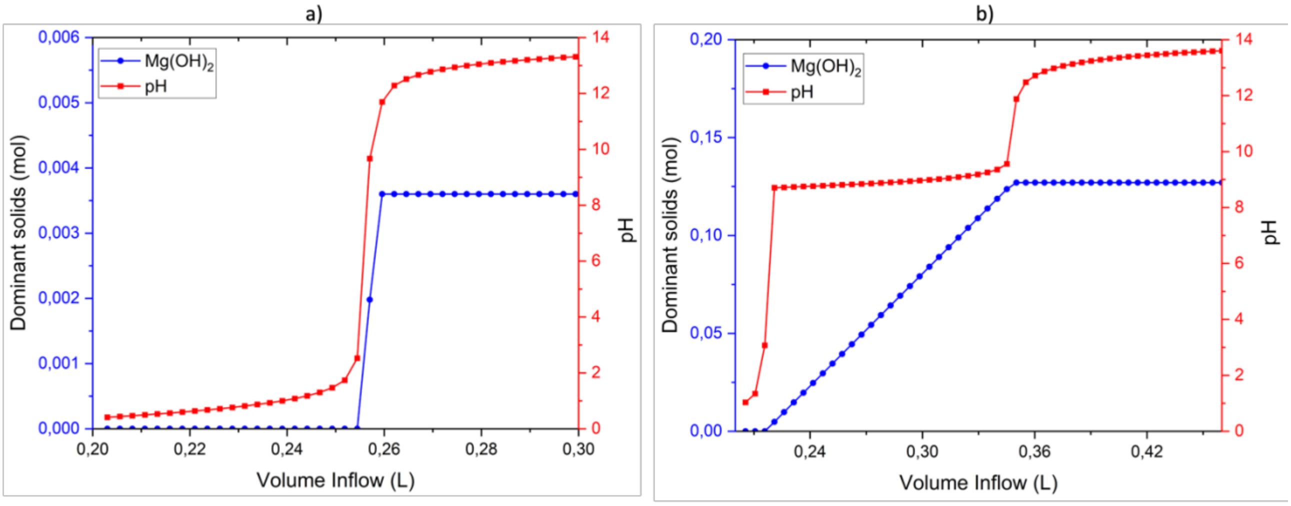

Figure 4.11 OLI Studio simulations of $Mg(OH)_2$ precipitation and recovery at T=25°C and atmospheric pressure with: **a)** DD Strip solution; **b)** DD Feed solution.

From Figure 4.11b. it can be highlighted that $Mg(OH)_2$ formation occurs at pH 10 with a linear increase of the amount of solid in the solution until the complete precipitation of initial mols of Mg^{2+} and, after that point, the stabilization of $Mg(OH)_2$ to the maximum theorical corresponds to a further increase of pH value.

This behaviour can be justified considering that, after complete Mg^{2+} precipitation, all the OH^- ions introduced remain in solution, rising pH value.

The flatter increase of pH trend and the sudden achievement of the maximum theoric of $Mg(OH)_2$ precipitated, showed in Figure 4.11a. (Permeate curve), can be explained considering the lower concentration of buffer agent (Mg^{2+}) and the higher H^+ concentration in the strip solution compared to the Permate.

Performance parameters for evaluation of precipitation are Recovery Yield and Purity, respectively expressed by eq 21 and 22:

$$Recovery\ (Y)\ \% = \frac{N_i^0 - N_i^f}{N_i^0} * 100 \qquad (21) \qquad\qquad Purity\ \% = \frac{X_i}{\sum_i^n X_i} \qquad (22)$$

where N_i^0 and N_i^f are mols or i-th cation respectively at the beginning and at the end of precipitation test, while in eq 15 X_i is referred to molar fraction of i-th cation [110].

In this step, three main feeds have been treated: PhMD retentate, Donnan dialysis draw and Donnan dialysis retentate, both from F5 test.

As shown in Figure 4.12a, the progressive addition of NaOH to the solution mimicking PhMD retentate determined an initial gradual increase of pH from the starting value of 7.3 to ≈ 9.3; at this point, a visual inspection showed the solution becoming cloudy due to the appearance of $Mg(OH)_2$ microparticles.

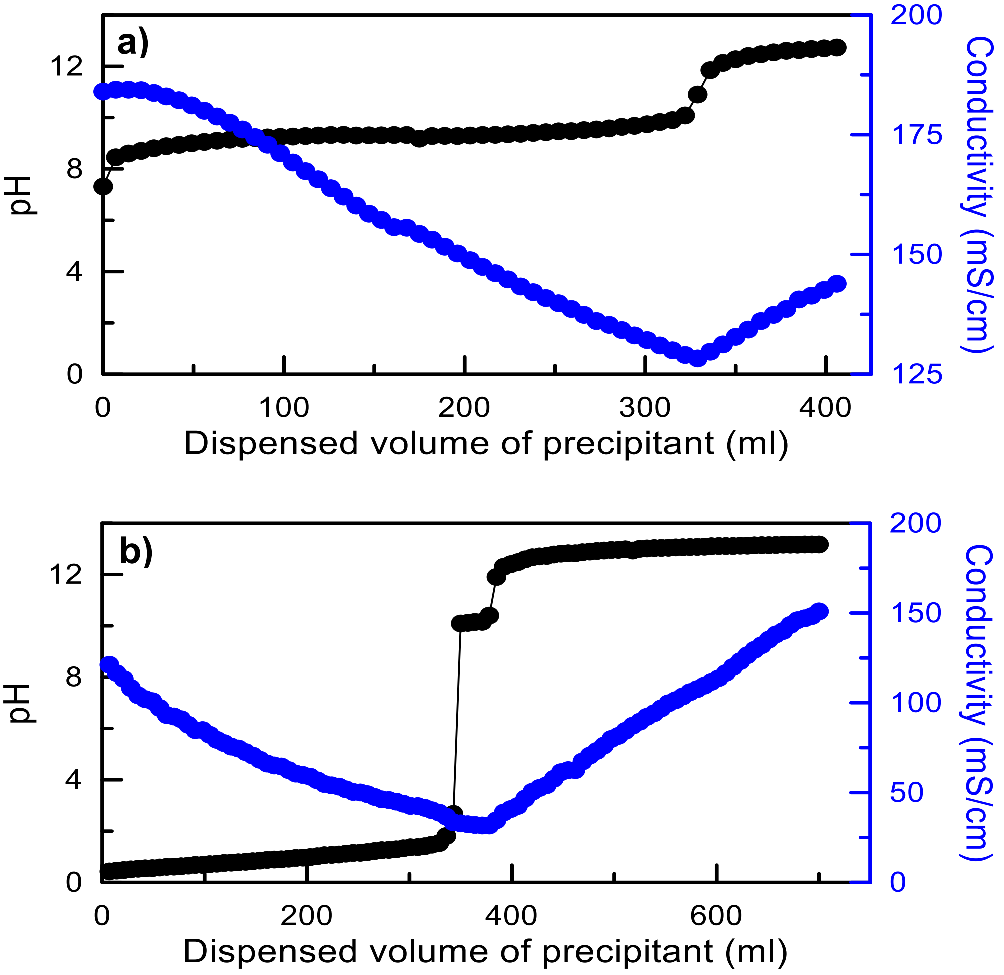

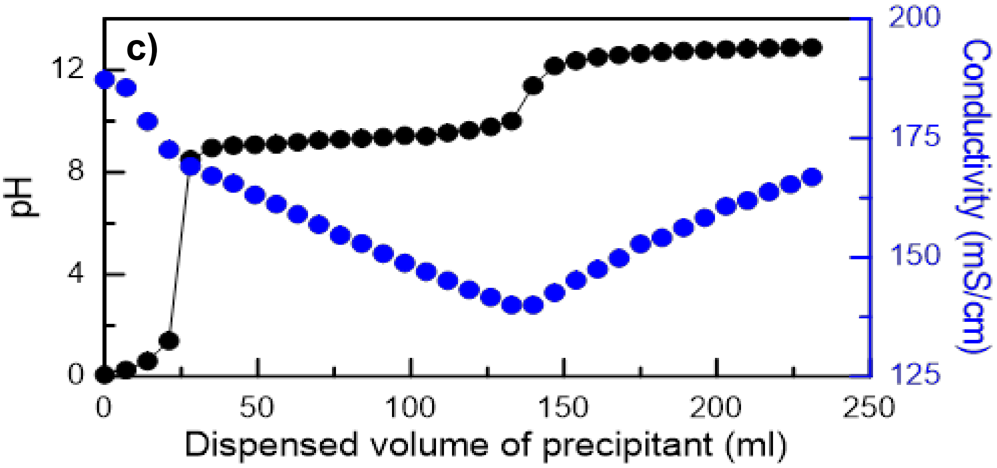

Figure 4.12. Reactive precipitation of $Mg(OH)_2$ by addition of 2M NaOH to artificial solutions mimicking: **a)** PhMD retentate; **b)** DD draw; **c)** DD retentate.

Further addition of precipitant resulted in a pH almost stable within the range 9.3-10, while conductivity decreased as magnesium and hydroxyl ions left the liquid phase by crystallization. The end of the precipitation process was accompanied by a sudden increase of pH to ≈12; from here on, the conductivity curve steeply increased due to the continuous addition of OH^- ions to the solution. In general, considered that all the magnesium was reacted, the pH changed rapidly because no buffering agents are present [122]. The final amount of solid recovered (about 50g) confirmed a yield practically of 100%.

In the case of precipitation tests carried out on DD draw solution (Figure 12.b) and DD retentate solution (Figure 12.c), both characterized by a low pH, the initial addition of NaOH causes a notable decrease of conductivity associated to the neutralization of hydrogen ions by added hydroxyl ions as follows:

$$H^+{}_{(aq)} + OH^-{}_{(aq)} \rightarrow H_2O \quad (16)$$

Accordingly also to OLI Studio simulations (Figure 11), Mg^{2+} precipitation under the form of $Mg(OH)_2$ can be considered complete in both DD Feed and draw solutions around pH 10 and, due to the low amount of Mg^{2+} ions transferred through the CEM used in DD, the completed $Mg(OH)_2$ precipitation resulted in the recovery of 98% of initial Mg^{2+}.

Also in these two last cases, the completion of $Mg(OH)_2$ precipitation is highlighted by conductivity trend inversion, due to the fact that OH^- ions introduced in solution are not consumed through precipitation but remain in solution causing an increase of pH.

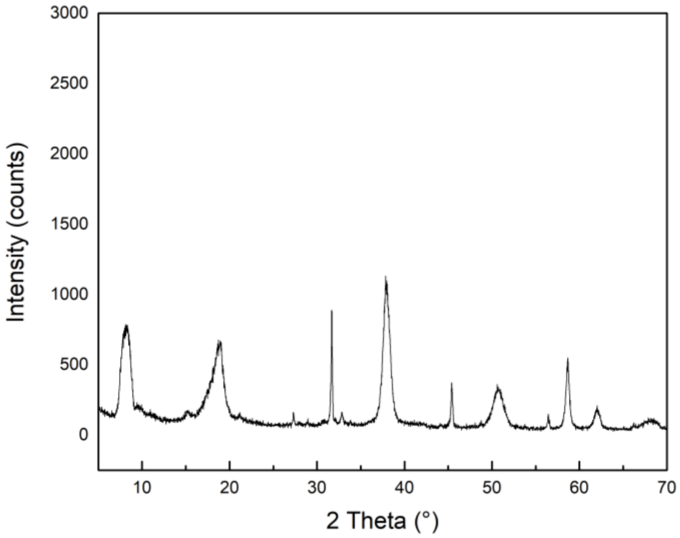

Figure 4.13 XRD pattern of solid precipitate from DD Feed precipitation test.

In Figure 4.13 it is reported the XRD pattern of DD feed precipitation test and thanks to that it was possible to confirm the high purity of the obtained solid. Purity of $Mg(OH)_2$ was 97.3%, with a 2.7% of NaCl impurity identified, maybe due to some residue of NaCl contained in the initial feed that was not entirely washed.

4.4 Conclusions

In this chapter, a synthetic 3.5 times concentrated RO brine has been treated employing Donnan Dialysis – reactive precipitation integrate process for the selective removal and recovery of Magnesium ions under the form of $Mg(OH)_2$.

A peristaltic pump was employed to recirculate the concentrated saline solution through a dialysis module, in order to exploit the concentration gradient across the commercial Fuji-Film Type 1 CEM for the Mg^{2+} ions stripping.

Stripping performances were evaluated coherently with mass transport phenomena driven by diffusion, in fact the ion transfer rate increases at increasing HCl concentration.

In the case of single-ion feed solutions F1 and F2, 2.8 and 2.2-fold enhancement were observed in combination with increasing acid molarity from 0.1 to 0.5M, respectively.

Strip conductivity showed a decreasing trend with time, simultaneously with ions exchange through CEM, in all the performed tests and during the entire experimental span.

The higher HCl concentration in strip brought to more emphasized negative variations of conductivity, with a $\approx$ 58% decrease recorded in F1 test at 0.1M HCl and $\approx$ 19%, the most negligible one, observed in F4 test with 0.5M HCl strip solution.

Similarly, the trend of pH in Feed phase followed a common behavior, given by the migration of H^+ ions from strip to feed phase, in order to counterbalance the Mg^{2+} migration in the opposite direction.

In Multi-ions feed experiments, the ion transfer rate from Feed to Strip side remains constant over time (Na^+: 3.4 mol/m^{2}h; Mg^{2+}: 0.17 mol/m^{2}h) and emphasized the ability of employed commercial CEM to preferentially remove the monovalent ion. With respect to DD tests with single salts, the ion transfer rate for Na^+ and Mg^{2+} decreased by 27% and 78%, respectively.

At the end, reactive precipitation step showed a remarkable match between OLI Studio simulation and experimental, highlighting a $Mg(OH)_2$ formation in DD Feed and Strip treatments occurred at pH between 9 and 10 with a linear increase of the amount of solid in the solution until the complete precipitation of initial mols of Mg^{2+} and, secondly, the stabilization of $Mg(OH)_2$ to the maximum theorical, corresponding to a further increase of pH value. The obtained $Mg(OH)_2$ showed a purity of 97.3%, with a 2.7% of NaCl impurity.

DD showed interesting capabilities in Mg^{2+} separation from R.O. brines, even though hindered from Na^+ ions massive permeation caused by a higher concentration gradient.

In this scenario, the research of selectivity increase of the CEM towards Mg^{2+} permeation represents the next step in Magnesium recovery from concentrated brines, in order to overcome the preferential transport of the monovalent ion.

Chapter 5 – Lithium recovery from battery leachate

5.1 Introduction

The dramatic impacts of the climate change, environmental pollution and energy insecurity on the environment and the society have imposed a cardinal change towards the sustainable development and the decarbonization [123].

Since 1982, the proposed solution has been identified in the large-scale replacement of fossil fuels with clean and renewable energy sources aimed to satisfy the Kyoto Protocol requirements, carrying out a reduction of carbon dioxide emissions [124][125].

Beyond the flourishing of portable devices, the intermittence of renewable energy resources has drastically increased the pivotality of technologies for the energy storage [ref]. Especially, Lithium-ion batteries (LIBs) secure high-density storage (>100 Wh kg^{-1}) in light, compact, safe, inexpensive and reliable devices [126]. Therefore, Lithium (Li) has been considered the core strategic material for the sustainable development. Li is the lightest alkali metal with a density of 0.534 g/cm^3 and an electrochemical activity quantifiable through an outstanding electrode potential of -3.05 V [127] exploited in rechargeable batteries industry [128–131].

Nowadays, Li is from ores (less common) and natural brines (currently dominant). It has been assessed that the environmental impact – more precisely the Global Warming Potential (GWP) – of extraction process from ores and brines was quantified respectively in 2.27 kg and 2.02 kg of CO_2-Eq per kg of Li_2CO_3 [132]. The extraction of Li from brine is based on the vaporization of the water in ponds under the effect of the wind and the sun promoting the precipitation of other minerals (Na, K, Mg) and the concentration of the Li ions [12] subsequently precipitated with soda ash in form of lithium carbonate (Li_2CO_3). This approach presents serious advantages from the economic and energetic point of view, but it is characterized by long resilience time in the evaporation ponds (1-2 year) and an unpair water-Li balance [133], aggravated by high presence of Li in salt-lakes of arid region of South America [12]

In this scenario, Membrane Distillation (MD) and Membrane Crystallization (MCr) are emerging as suitable technologies for mineral recovery via hypersaline retentate stream generation [19].

MD and MCr can ensure water recovery in reduced time, in fact MD is identified as a non-isothermal process based on evaporation and transport of vapour in macroporous membranes (with pore diameters between 0.05 and 0.5 μm) of a hydrophobic membrane contacting an aqueous solution. More specifically, it provides a support for the creation of a liquid-vapour interface at each pore mouth, where phase transition takes place[18]. On the other hand, MCr can be identified as the protraction of water recovery – via MD – up to supersaturation conditions of the saline solution [10,15,17,18]. As a consequence of the previous-described features and of the total absence of osmotic phenomena, MD and MCr can be implemented as a synergic complement to the conventional pressure-driven processes in desalination and mineral recovery from brines [19].

The demand for Li is continuously and quickly growing: Li_2CO_3 production will increase from 265,000 tons in 2015 to 498,000 tons in 2025 with a forecast to witness a supply shortage after 2023.

Beside the necessity to intensify the Li mining sector, its recovery from exhaust LIBs can be considered great opportunity in the logic of the circular economy and the mitigation of the Li-water nexus [129,134].

Li Recycling techniques from LIBs can be categorized in three sub-categories: Hydrometallurgy-dominant methods, Pyrometallurgy-dominant methods, and Mild recycling methods [129].

The first-cited sub-category involves separation of valuable metals through leaching, precipitation and solvent extraction with solutions based on acid/alkali/organics, while the pyrometallurgy technique, which is the most frequently employed in the industry since it is short and readily to scale up, performs the extraction of the valuable metals with a physicochemical transformation at high temperature. The mild recycling approaches integrate the advantages of the two previous-described techniques reducing the employment of acid/alkali/organics and lowering the high operative temperature [129].

The acid leaching, Sulfuric Acid (H_2SO_4) [135–140], such as Hydrochloric Acid (HCl) [138,141] or Malic Acid [142], is a relatively used technique for the recovery of lithium from electrode material, exploiting the high solubility of metal ions in acid solutions.

In this context, leachate treatment represents the next step, and particularly, the core of the Li recovery process. Many techniques have been explored and tested for this scope, including selective Adsorption as overviewed by Xu et al. [143], reporting the effectiveness of Lithium ion-sieves as adsorbent with adsorption values up to 11 mg of Li per g of adsorbent associated to H-Mn-O, and by Zandevakili et al. [144] highlighting an interesting uptake capacity of inorganic ion-sieves tested batchwise with values around 62 g of Li per g of adsorbent.

Moreover, Electrodialysis can be considered another suitable technique for Li removal and enrichment [145,146]. Song et al. [147] promoted Li_2CO_3 precipitation through electrodialysis coupled with Cation Exchange Membranes for the selective separation of lithium from dissolved Li_3PO_4 solution.

In literature, precipitation technique was explored in both heterogeneous and homogeneous variants. The heterogeneous precipitation of lithium from liquid solutions can occur through the bubbling of CO_2 as gaseous precipitant [148,149] or the addition of solid precipitant [130,131,150,151]. As an example, Gerold et al. assisted the precipitation performances in heterogeneous conditions with the employment of Na_2CO_3, Na_3PO_4 and K_2HPO_4 in solid phase, reporting a precipitation efficiency up to 95% using Na_3PO_4 as a precipitating agent.

On the other hand, homogeneous conditions require the reaction between Li-containing solution and precipitant-containing solution, for instance through the addition of Na_3PO_4 solution to precipitate lithium under the form of Li_3PO_4 or the addition of Na_2CO_3 solution to precipitate Li_2CO_3 with recovery efficiencies above 90% [133,152,153].

Our approach was aimed to implement hydrometallurgical process, consisting in the processing of a pretreated stream with a step-by-step removal of impurities integrated with a MD step for a further concentration of Li-containing solution in order to obtain additional water and increase the overall lithium removal in the consecutive heterogeneous precipitation stage.

In this work, the simulated exhaust batteries leachate was pre-treated through the addition of oxalic acid for a preliminary removal and recovery of Nickel, Manganese and Cobalt under the form of oxalates. Then, in order to recover the water and the Li, three main steps were systematically studied and assessed: i) pH adjustment of the leachate via $Ca(OH)_2$ addition to favour the precipitation of the residuals of sulfates; ii) Air-gap Membrane Distillation (AGMD) to increase Li concentration in the stream in combination with water recovery; iii) Li recovery through chemically induced precipitation of Li_2CO_3 via addition of Na_2CO_3 in solid phase.

5.2 Materials and Methods

5.2.1 Materials

All the metal ions were solubilized in the initial stream under the form of hydrated sulfates: Lithium sulfate monohydrate ($Li_2SO_4*H_2O$), Nickel Sulfate Hexahydrate ($NiSO_4*6H_2O$), Maganese Sulfate monohydrated ($MnSO_4*H_2O$), Cobalt Sulfate Heptahydrate ($CoSO_4*7H_2O$). Calcium Hydroxide ($Ca(OH)_2$) and Sodium Hydroxide (NaOH) were employed as alkaline in preliminar precipitations and pH setting, while Oxalic Acid ($C_2H_2O_4$) was used to mimic the Oxalates concentration in initial leachate and Sodium Carbonate (Na_2CO_3) was chosen as precipitant in Li-recovery stage. All the chemicals employed in this work were purchased from Sigma Aldrich® and used without further purification. Ultrapure Water was obtained with the employment of ELGA Purelab Cassic device.

5.2.2 pH Adjustment

Table 5.1 reports the composition of the solution employed for the experiments mimicking the composition of the solutions obtained from the acid leaching of lithium spent batteries.

The leachate solution was obtained by solubilization of Lithium Sulfate monohydrate ($Li_2SO_4*H_2O$), Nickel Sulfate hexahydrate ($NiSO_4*6H_2O$), Manganese Sulfate monohydrate ($MnSO_4*H_2O$), Cobalt Sulfate heptahydrate ($CoSO_4*7H_2O$) in 250mL of deionized water under magnetically stirring at 300 rpm at 20°C rpm for one night, in addition with H_2SO_4 99,99% and $C_2H_2O_4$ in powder in concentrations described in Table 5.1.

Table 5.1. Composition of the leachate solution.

Species	Concentration [mol/L]
$Li_2SO_4*H_2O$	0,202
$NiSO_4*6H_2O$	0,0093
$MnSO_4*H_2O$	0,056
$CoSO_4*7H_2O$	0,011
H_2SO_4	1,41
$C_2H_2O_4$	0,68

The pH adjustment consisted of three precipitation experiments performed by gradually adding 2,2 M of Calcium hydroxide to 50 mL of starting solution under stirring along three different reaction times (24h, 48h and 4 days).

All the previous tests were performed at ambient temperature and pressure, in combination with a stirring speed of 300 rpm, guaranteed by IKA® RCT basic.

At the end of each experiment, the reacted solution was poured in a 50 mL falcon and centrifuged at 1200 rpm for 5 minutes in a centrifuge Sigma 3-16L.

Then, the supernatant was separated from the precipitated and, after a preliminary filtration through a syringe filter 0,45 μm Millex with Durapore membrane, analyzed using an Inductively Coupled Plasma – Optical Emission Spectroscopy (ICP-OES) model iCAP 7000 Series.

On the other side, the solid part was washed with deionized water, dispersed by using a VortexGenie-2 with an intensity of 4 and filtered through a quantitative filter paper 424 using a vacuum pump DIVAC 2.2 L. The obtained solid was dried in an oven at 45°C for five days and then analyzed with a XRD equipment ARL EQUINOX 100 X-ray Diffractometer.

5.2.3 MD

The Membrane Distillation (MD) step has two main goals: water recovery and pre-concentration of the stream before the Lithium recovery.

The process was operated in Air-Gap configuration (AGMD) based on the system described in figure 1 and employing a double-layer flat-sheet Polytetrafluoroethylene (PTFE) membrane in combination with Polypropylene (PP) to guarantee a proper mechanical stability of the module.

The effective surface area was 1886 cm^2 with a thickness of 67μm and a nominal pore size of 0,22 μm.

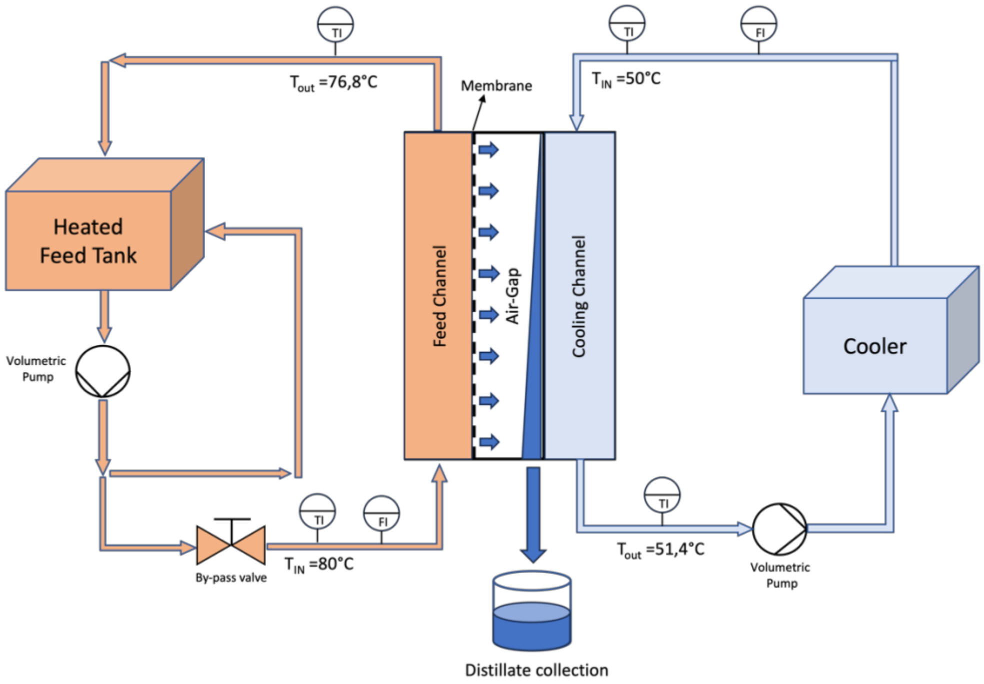

Figure 5.1 Scheme of employed MD system

AGMD was performed at 80°C starting from an initial volume of the feed of 27 L and it was protracting up to achievement of a final volume of 9 L (Concentration factor equals to 3).

The Feed flowrate was kept around 10 L/min using an IWAKI magnetic drive pump MD30R and acting on the bypass valve (globe type) regulation while the cooling consisted in water flowing at 10 L/min in combination with a cooler set to 50°C.

The initial Feed of this step consisted in deionized water enriched with 0,404 M Li^+ (0,202 M Li_2SO_4 H_2O) at a pH of 11.5 adjusted by the addition of 0,1 M NaOH.

Process parameters analyzed and registered during the MD test are Distillate and Feed Conductivity, Distillate volume and final value of pH.

Initial value of pH was measured using Filter-Lab® indicators, while the conductivity in Feed and Distillate side conductivity was measured with the employment of a portable Hanna HI98192 conductometer.

5.2.4 Lithium precipitation and recovery

In Lithium recovery stage, precipitation was inducted by the addiction of Sodium Carbonate (Na_2CO_3) powder to the retentate of the AGMD stages containing Li at a concentration of 1.2 M.

In the first set of experiments, it was investigated the optimal reaction time (24 h, 48 h and 4 days) under-stirring at 350 rpm in an oil bath IKA® HBR 4 control to thermostat the solution at 20, 50 or 80°C.

In the second set of experiments, a wider reaction times interval was monitored at 20°C, taking a sample of the liquid fraction at: 15’, 30’, 1h, 2h, 4h, 6h and 16h.

Once observed the optimal time necessary for the precipitation, it was investigated the optimal operative temperature, setting the oil bath thermostat at 50°C and 75°C.

In all the performed experiments, 7.95 g of Sodium Carbonate were gradually added to 50 mL of initial solution containing 0.60 M Lithium Sulfate monohydrate with a pH adjusted to 12 through the addition of 0.1 M NaOH in pellets.

As for pH adjustment stage, the reacted solution was centrifuged at 1200 rpm for 5 minutes in a centrifuge Sigma 3-16L. Then, the liquid part is separated from the precipitated and, after a preparatory filtration through a syringe filter 0,45 μm, analyzed using an ICP-OES model iCAP 7000 Series.

On the other side, the solid part was washed with deionized water, shaked using a VortexGenie-2 with an intensity of 4 and filtered through a quantitative filter paper 424 using a vacuum pump DIVAC 2.2 L. The obtained solid was dried in an oven at 45°C for five days and then analyzed with a XRD equipment.

5.3 Results and discussion

5.3.1 pH Adjustment – OLI simulation

The initial stream treated in pH adjustment stage has the composition of the oxalates precipitation output, aimed to remove a considerable fraction of Co, Mn and Nickel for an isolation of Lithium to optimize Li_2CO_3 precipitation. The main goal of the pH adjustment stage is to process the entering stream with $Ca(OH)_2$ in order to raise up the pH initial value, that lines up around zero, to successfully precipitate the Mn and Co residuals in addition to $CaSO_4 * 2H_2O$ (Gypsum) precipitation.

From a chemical point of view, Gypsum precipitation follows the reaction:

$$Ca^{2+}{}_{(Aq)} + SO_4{}^{2-}{}_{(Aq)} \rightarrow CaSO_4 * 2H_2O_{(s)} \qquad (1)$$

From a physical side, Gypsum is formed in supersaturated aqueous solutions by a polynuclear mechanism and, in particular, the combination of negative and positive ions leads to a negative value of ΔS, which means a decreasing of the degrees of freedom depending on the decreasing of the number of various species [154].

$Ca(OH)_2$ was chosen as precipitating agent with the aim to remove the entire amount of sulfates ($SO_4{}^{2-}$) in solution coming from leaching process under the form of Gypsum.

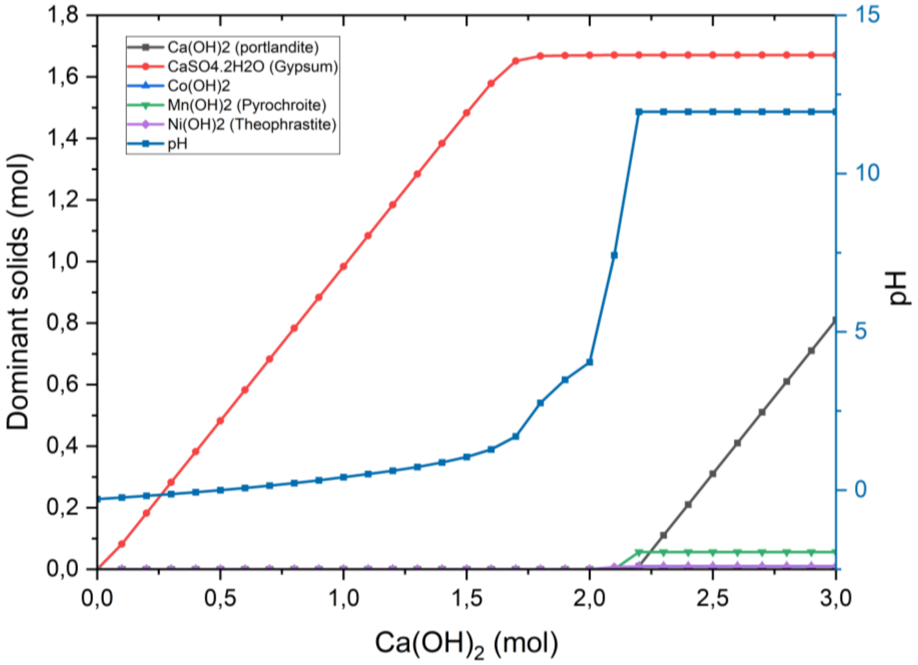

Figure 5.2 Oli Studio simulation of pH adjustment test

As can be noticed from Figure 5.2, $Ca(OH)_2$ solids increase vigorously in combination with the increasing of solution pH (i.e. with the increasing of the OH^- concentration) and this is due to the common ion effect [155].

From the same simulation performed with OLI Studio, it can be highlighted the limit of solubility of the precipitant agent – theoretically equal to 0.02 mols per liter of water at 25°C [156] – that remains undissolved after 2.2 mol/L after reaching a pH of 12. After these conditions, $Ca(OH)_2$ (Portlandite) solids increases linearly in accordance to the addition rate.

Simulation shows that when the curve of $CaSO_4 * 2H_2O$ begins to flatten, pH begins to increase rapidly up to the value correspondent to solubility limit of Portlandite.

At 2.2 mol/L of $Ca(OH)_2$, pH reaches rapidly the value of 12 and it can be noticed the precipitation of the entire amount of Manganese under the form of $Mn(OH)_2$, in fact at pH 10 Mn^{2+} ions are only partially converted to $Mn(OH)_2$ via eq 2:

$$Mn^{2+} + 2(OH^-) \rightarrow Mn(OH)_2 \qquad (2)$$

Between pH 10 and 12, eq 2 is completely moved to right, with a complete conversion of Mn^{2+} in $Mn(OH)_2$ [157] in combination to a stabilized value of precipitated gypsum, meaning that sulfates have been completely removed from initial solution. For this reason, 2.2 mol/L has been identified as the optimal $Ca(OH)_2$ concentration for this stage.

5.3.2 pH Adjustemnt – Experimental results

Effect of reaction time

The first package of tests aimed to investigate the optimal reaction time in precipitation of $CaSO_4*2H_2O$ (Gypsum) and hydroxides from impurity minerals with the addition of 2.2 mol/L $Ca(OH)_2$.

There is no significant difference in the results of the three samples, in fact the concentration of Co, Ni and Mn in solution after treatment is quite low in all of first three experiments and this is due to the precipitation of the previous-cited ions under the form of hydroxides as a consequence of pH increasing [158].

The addition of $Ca(OH)_2$ to the initial solution permitted to precipitate all the impurity minerals with removal efficiencies, as can be observed from Table 2, above 99% with the advantage to remove also SO_4^{2-} in combination with Ca^{2+} ions via eq 2.

The main benefit of the experimented technique is the completely negligible amount of lithium lost via precipitation during this step and this is due to the higher solubility of $Li_2SO_4*H_2O$, quantifiable at 400 g/L at a temperature of 25°C [159].

Table 5.2 Removal Efficiencies in pH Adjustment tests.

	Removal Efficiencies (%)			
Specie	**C_0 (M)**	**Test 24h**	**Test 48h**	**Test 4 Days**
Li	0,404	0,00	0,00	0,00
Mn	0,056	99,96±0,02	99,95±0,04	99,94±0,06
Ca	2,45	99,19±0,03	99,18±0,03	99,14±0,04
Ni	0,0093	99,21±0,03	99,32±0,05	99,62±0,07
Co	0,011	99,66±0,02	99,80±0,01	99,66±0,06

The only tangible dissimilarity was the presence of small white clusters of unreacted $Ca(OH)_2$ in the centrifuged solid belonging to the 24h test and this is due to the relatively short reaction time concerning the low solubility of the precipitant agent. On the other hand, solid fraction centrifuged from the 48 h and 4 days tests show a noteworthy homogeneity in terms of color and consistency thanks to the longer reaction time 8 (Figure 5.3).

As a consequence of the presence of unreacted $Ca(OH)_2$ in 24 h test and the superlative percentages in removal efficiency, the evaluated optimal reaction time was 48 h.

Figure 5.3 Centrifuged solid from pH adjustment 48h test.

Analysis of the dried solids were performed with the employment of XRD equipment (Figure 5.4) and the spectrum of the obtained solids matches with the spectrum of $CaSO_4*2H_2O$, thus detecting its predominant presence. Other impurities as $Mn(OH)_2$ have not been detected because of the very scarce amount of impurity ions in the experimental volume of the starting solution (50mL).

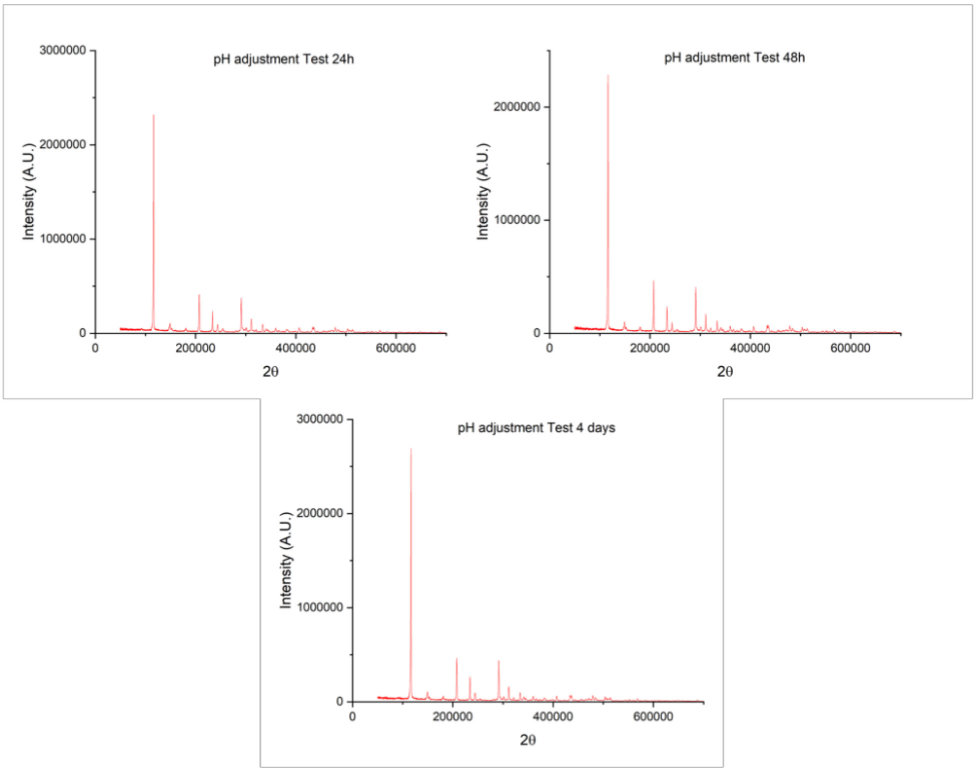

Figure 5.4 XRD detection of $CaSO_4*2H_2O$ in dried solid samples centrifuged from pH adjustment tests.

5.3.3 Pre-concentration and water recovery via Air-gap MD – OLI Studio simulation

The leachate stream treated with pH adjustment was further processed through Air-gap membrane distillation to increase Lithium concentration of the same stream and to recover water in a perspective of circular economy.

The composition of the stream and potential solids precipitation have been investigated through thermodynamic simulation with OLI Studio.

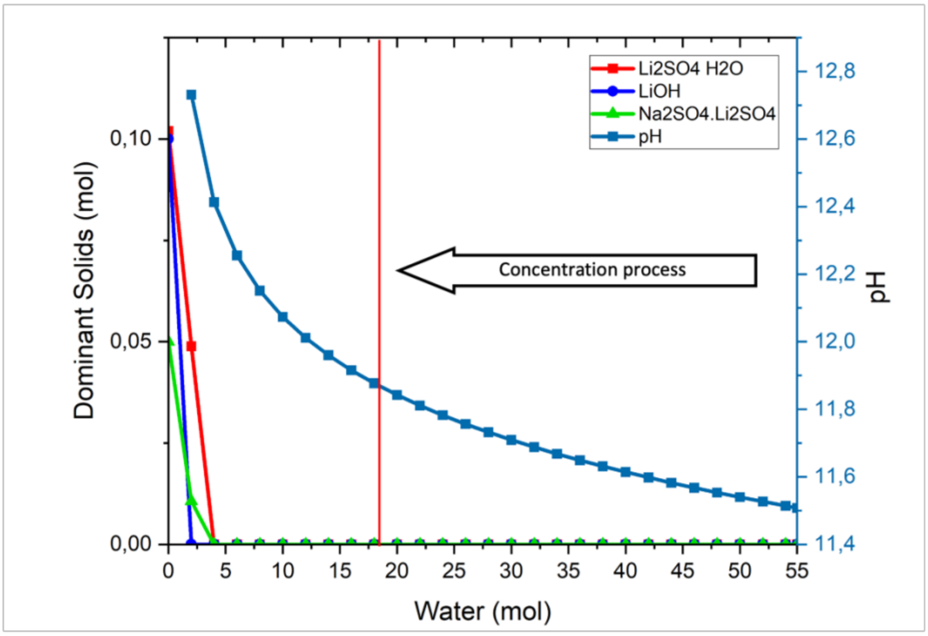

Figure 5.5 Oli Studio simulation for solids precipitation in MD Feed at pH 11,5 and 80°C based on 1 liter of initial solution.

In the simulation showed in Figure 5.5 it was analyzed a Lithium-containing stream with a pH value set at 12, in accordance to the pH of the solution coming from pH adjustment step, through the addition of 0,1 mol/L of NaOH.

The only present specie in the initial stream is Li_2SO_4 because of the removal efficiencies above 99% and the resulting negligible concentration of the other elements.

From Figure 5.5 it can be deduced that in the range from 1 L of water (55 mols) to 100 mL (5 mols) there is no precipitation of Li-containing solids such as $LiOH*H_2O$ and $Li_2SO_4*H_2O$ and this is due to the high solubility of these species, in particular 191 g/L at 30°C for the hydroxide [160] and 328 g/L at 40 °C for $Li_2SO_4*H_2O$ [161].

The absence of solids precipitation in the simulated process brought us to plan a three times concentration experimental step through Air-gap MD at a pH value of 11,5 and with a Feed temperature of 80°C and a 51°C cooling stream. Flowrates have been kept constant at 10 L/min for both Feed stream and Cooling Stream.

5.3.4 Pre-concentration and water recovery via Air-gap MD – Experimental

As can be highlighted from Figure 5.6, experimental distillate flux (L/m^2/h) showed a 6% decrease in the overall 6 hours experimental time span, even more emphasized with the increasing of concentration factor in the Feed. This MD experiment, and consequently Permeate flux analysis, was performed at fixed conditions (table 5.3) of temperature and flowrate in both Cooling and Feed sides.

Table 3 - Air-Gap MD operational parameters	
Initial feed volume, V_f^0 (L)	27
Feed pH	11,5
Li^+ initial Feed concentration, $[Li^+]^0$ (M)	0,404
Feed Temperature, T_f (°C)	80
Cooling temperature, T_c (°C)	50
Feed flowrate, m_f (L/min)	10
Cooling flowrate, m_c (L/min)	10

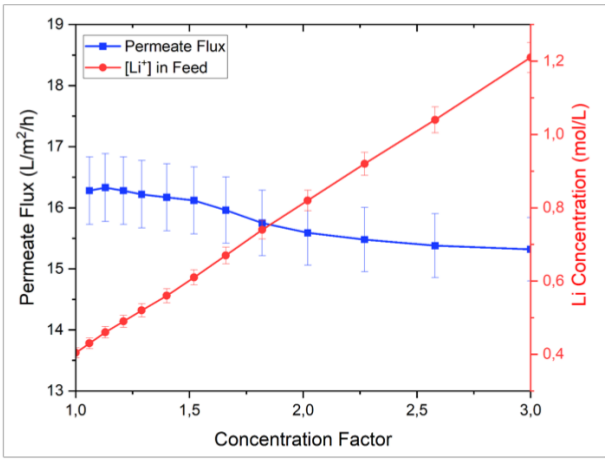

Figure 5.6 Permeate flux and Lithium concentration trends versus concentration factor of Feed stream (right) and resuming table of Air-Gap MD operational parameters (left).

More broadly, this behavior can be justified considering the mathematical definition of Permeate Flux (f), that is one of the main parameters useful to evaluate the performances of Membrane Distillation. From a theoretical point of view, permeate flux can be computed through the expression [162]:

$$J_w = C(p_{w,m}^{f} - p_{w,m}^{a}) \qquad (3)$$

Were C is the Membrane distillation coefficient or membrane flux coefficient [kg/m^2/Pa/s], $p_{w,m}^{f}$ represents the vapor partial pressure [Pa] at the Feed side membrane interface and $p_{w,m}^{a}$ consists in vapor partial pressure [Pa] at Air-Gap side membrane interface.

This parameter can be identified in the entire volume of produced water per unit area per unit time at specified Feed Flowrate and its temperature, Cooling Flowrate and its temperature and membrane specs.

The difference between the two vapor partial pressures represents the driving force of the process and, contextually, an increase of the concentration of the solute in the feed brings to a $p_{w,m}^{f}$

decreasing according to Raoult's law, which states that the value of $p_{w,m}^{f}$ at membrane interface is obtained by multiplying the vapor pressure of pure water p_w^0 evaluated at the interface temperature of the membrane, the molar fraction (x_w) and activity coefficient ($\gamma_w \neq 1$ for a nonideal mixture) of water in the feed solution.

The decreasing of the $(p_{w,m}^{f} - p_{w,m}^{a})$ term of eq 3 produces a decreasing of the driving force and consequently a progressive distillate flux decline (i.e. a lower amount of water vapor passing through the pores of the hydrophobic membrane)[73].

In accordance with that, the real advantage of MD process lies in the relative steadiness of distillate fluxes, thanks to the performances not limited by high osmotic pressure or concentration polarization phenomena [73,163].

On the other side, as we expected, [Li^+] increases linearly with respect to concentration factor, confirming that the initial value of 0.404 M is brought to 1.21 M in order to recover water and increase Lithium concentration to enhance the recovery factor in the subsequent step.

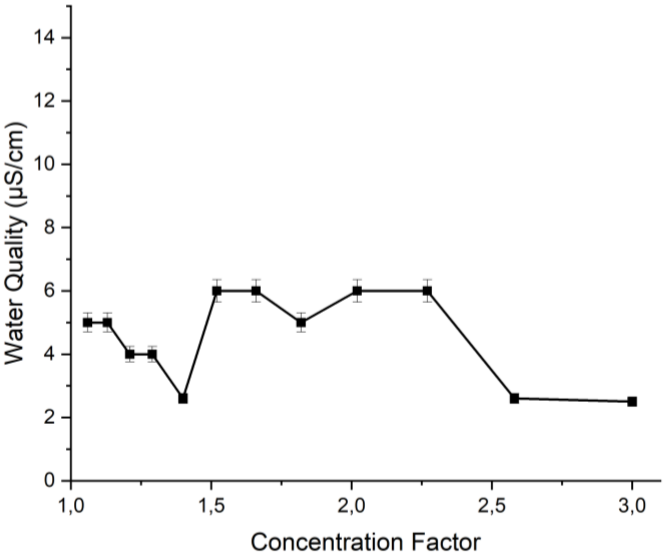

Figure 5.7 Water quality in μS/cm of produced distillate versus Concentration Factor.

Recovered water, as revealed in figure 5.7, showed a conductivity between 2.5 and 6 μS/cm in the entire experimental range stating the good quality of the permeate (i.e. zero seepage of Feed in the permeate) and achieving, at the end of the process, a water recovery factor over 66%.

This pre-concentration step has been analyzed also from a thermal energy point of view, evaluating the energy demand and quantifying the energy efficiency of the AGMD system employed in this experimental session.

MD is identified as a non-isothermal process, which means that it is a process involving a huge heat transfer through the membranes under the form of latent heat and conductive heat transfer.

Thermal energy consumed in this pre-concentration step was based on the evaluation of enthalpy change in the feed channel with an eventual sensible heat recovery on the cooling side. The heat transfer rate Q_f represent heat and Q_c is the one in the cooling side of the module and can be calculated following the Eqs. (4) and (5):

$$Q_f = m_f\ C_{p,H_2O}\ (T_{f,IN} - T_{f,OUT}) \qquad (4)$$

$$Q_c = m_c\ C_{p,H_2O}\ (T_{f,out} - T_{f,IN}) \qquad (5)$$

where m_f and m_c are the feed and cooling water mass flow rates (kg/s) respectively, C_p is the specific heat of water (4.186 kJ/kg/K) and $T_{f,in}$ and $T_{f,out}$ are the feed temperatures (°C) at the inlet and outlet of the membrane module, respectively. $T_{c,out}$ and $T_{c,in}$ are the temperatures (°C) of the cooling water leaving and entering the MD modules respectively [76].

When the heat transferred to the cooling side is assumed to be recovered, the net heat demand for the MD process is calculated using eq 6:

$$Q_{net} = m_f\ C_{p,H_2O}\ \left(T_{f,IN} - T_{f,OUT}\right) - \varphi\ m_c\ C_{p,H_2O}\ (T_{f,out} - T_{f,IN}) \qquad (6)$$

The parameter φ indicates heat recovery on the cold side and assumes a value of 1 for higher cooling temperatures (50°C) of $T_{c,in}$ and 0 for cooling temperature of 15°C.

On the other hand, Specific heat demand, that consists in the amount of heat necessary for the production of one cubic meter of permeate, is measured in kWh/m^3 and is computed from the net heat demand following the Eq. 7:

$$Q_{sp} = Q_{net}/m_p \qquad (7)$$

Parameter m_p indicates the permeate flowrate measured in m^3/h [77].

As can be observed from figure 5.8, specific heat demand of the MD plant increases gradually in accordance with the reduction of permeate flux. In particular, specific heat demand showed a 6% overall increase in the entire experimental time interval, relatable to an identical and opposite variation of permeate flux, thus confirming the inverse mathematical relation expressed by eq 3 [76,164].

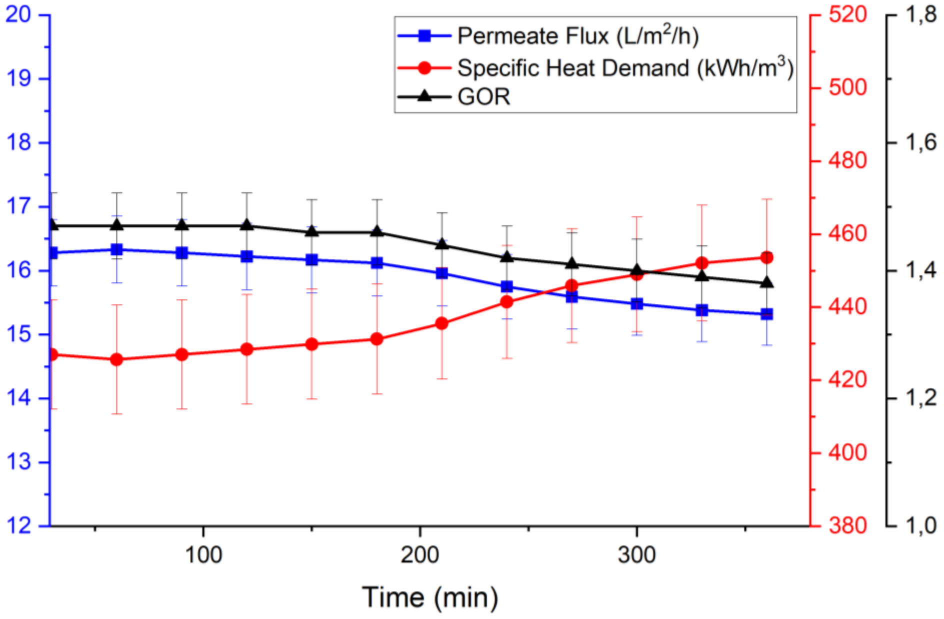

Figure 5.8 Trends of Permeate flux, Specific heat demand and GOR versus time in Air-Gap MD.

In addition to specific thermal energy demand, Gained Output Ratio (GOR) is defined as a ratio between useful heat and the total heat input of the system and it is employed to evaluate the thermal efficiency of the process, the higher the GOR value, the better the system perform in terms of heat recovery. GOR can be computed using the eq 8:

$$GOR = \frac{J_w \, \Delta H_v \, A_m}{Q_{net}} \qquad (8)$$

J_w represents the permeate flux in (kg/m^2/s), A_m is the area of permeation in (m^2), which is equal to the total area of the membrane, ΔH_v is the enthalpy of vaporization of water in (kJ/kg), and Q_{net} is the total input power used by the MD system in (kW).

This latter parameter ranged, during the entire experimental period, in an interval included between 1.38 and 1.47, showing an experimentally observed overall reduction near to 6% according to direct mathematical relation between permeate flux and GOR expressed by eq 8 [78].

5.3.5 Li precipitation and recovery – OLI Studio simulation

Water recovery is not the only advantage of MD step, in fact the additional concentration of the stream coming from pH adjustment brings to an increasing Lithium concentration in the solution, ensuring an easier and more efficient Lithium recovery via precipitation [139,147].

Before the experimental part, it was performed a simulation of Lithium precipitation at three different temperatures, in order to investigate the optimal reaction conditions. Investigated temperatures are 25°C, 50°C and 75°C.

On the other hand, pH was kept stable at the conditions of the MD output stream (≈ 12) and it was adjusted via addition of 0.1 mols of NaOH per liter of initial solution. The choice, in this particular process, of NaOH as pH setting reagent instead of $Ca(OH)_2$ helped us to avoid undesired precipitations as, for instance, Calcium carbonate ($CaCO_3$), with a subsequent loss of carbonate ions (CO_2^{2-}) and a logically correlated decreasing of Lithium recovery under the form of Li_2CO_3.

In all the performed simulations showed in figure 9, Li_2CO_3 precipitation (i.e. Lithium recovery) increases vigorously with the addition of the first mol of Na_2CO_3 per liter of solution recovering up to 75% of Lithium in the 25°C test and approximately 80% in 50°C and 75°C attempts, highlighting the main dissimilarity between the three curves. In the previously analyzed interval, slope of the Li_2CO_3 curve increases in combination with the increasing of reaction temperature, showing in all the cases a flattening of the curve after 1.5 mol of Na_2CO_3 and, in particular, a small hump in 75°C test.

The direct correlation between Li_2CO_3 precipitation and temperature is due to the behavior of its solubility, which decreases in combination to the higher temperatures [130,139,165].

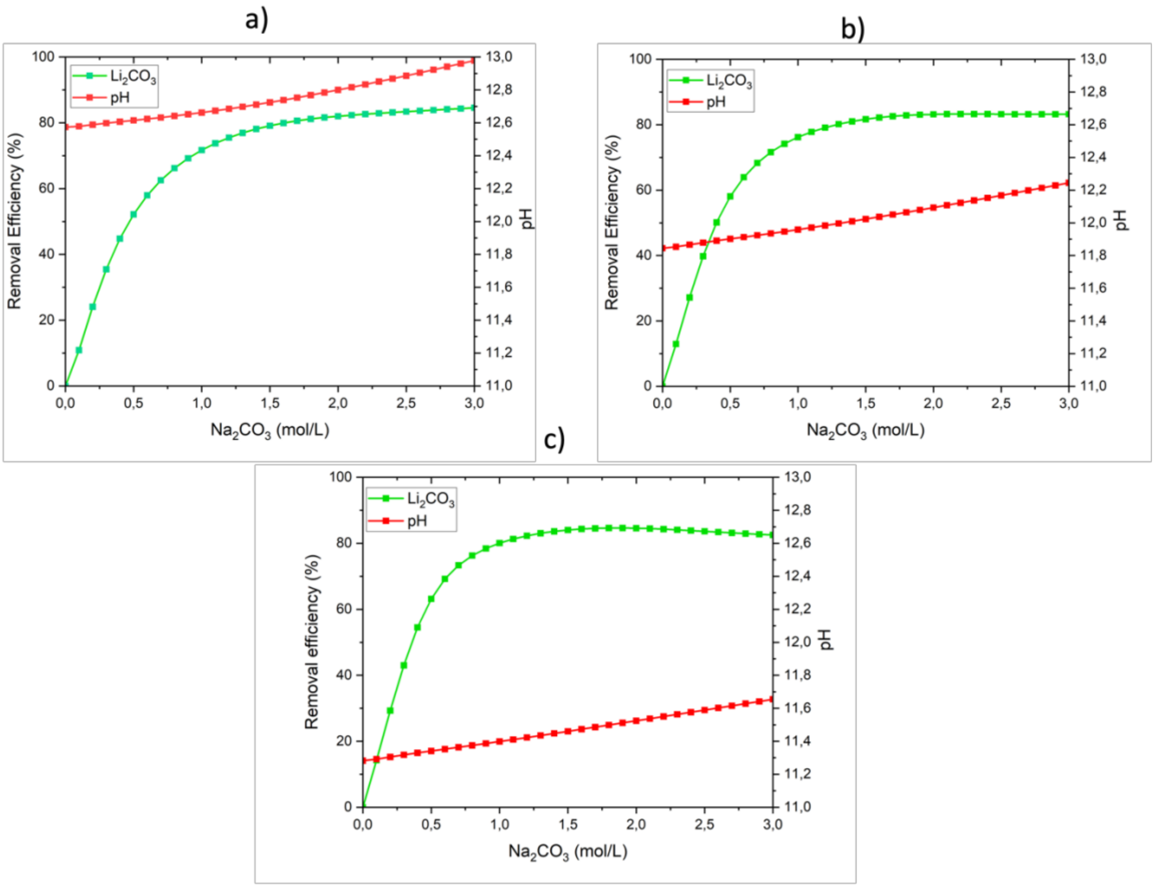

Figure 5.9 Oli Studio thermodynamic simulations of Li_2CO_3 precipitation at 25°C (**a**), 50°C (**b**) and 75°C (**c**) in alkaline environment.

Concerning the pH trends, in these three conditions pH values decrease in parallel with the increasing of operative temperatures in accordance with the effect of temperature on hydrogen activity coefficient, employed for the calculation of pH via eq 9 [166].

$$pH = -log_{10}\, a_{H^+} \qquad (9)$$

In all the three tests, the pH curve showed a slight 4% growth in the simulated interval, due to the precipitation phenomenon.

5.3.6 Li precipitation and recovery – Experimental

It was experimentally investigated the Li_2CO_3 precipitation performances from MD concentrated stream.

Firstly, it was investigated the reaction time effect of precipitation, working at constant temperature and with a constant $[Na_2CO_3]/[Li^+]$ ratio. More specifically, the amount of Na_2CO_3 added gradually to the Li-containing solution was fixed to 1.5 mols per liter of solution, corresponding to a $[Na_2CO_3]/[Li^+]$ ratio of 1.24. This optimal ratio was selected based on the three simulations previously showed, in fact 1.5 mol/L is the concentration of precipitant agent after that the curves start to flat with a corresponding stabilization of Recovery efficiencies at values comprised between 78 and 82% regardless of the increasing of precipitant agent added.

This simulation result is in accordance with literature, where it was observed that the precipitation yield of lithium as Li_2CO_3 was increased with an increase in $[Na_2CO_3]/[Li]$, and maximum precipitation yield (90%) was obtained at $[Na_2CO_3]/[Li] = 1.0$ [130]. In the same work the reaction time was fixed at 15 hours.

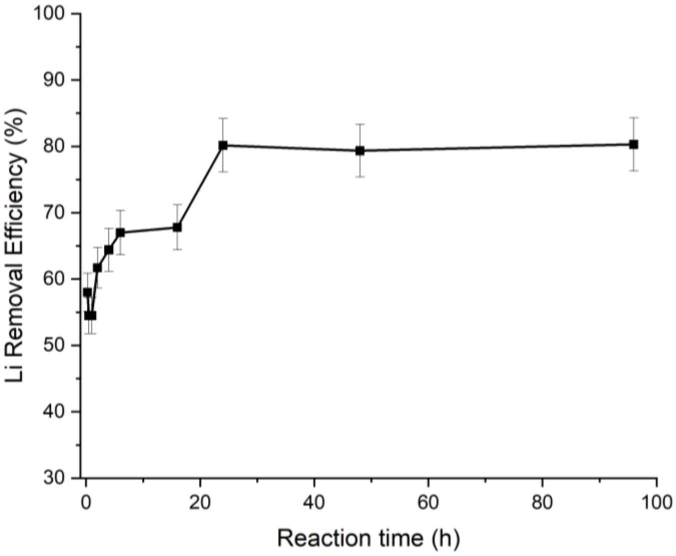

Figure 5.10 Trend of Li_2CO_3 precipitation in 96 hours of time interval at 25°C and with a $[Na_2CO_3]/[Li^+]$ ratio kept constant at 1.24.

After simulation stage, reaction time effect was analyzed in shorter intervals in the first two hours with gradual lengthening up until 96 hours.

Removal Efficiency was analyzed at: 15’, 30’, 1h, 2h, 4, 6h, 16h, 24, 48h, 96h.

As can be observed from Figure 5.10, recovery of Lithium under the form of Li_2CO_3 increases vigorously in the first 24 hours, in which it reaches the maximum value of 80.2%.

Between 24 and 96 hours, Lithium recovery efficiency remains stable, suggesting to avoid an excessive and useless extension of the precipitation step and setting the optimal reaction time to 24h, in accordance to other works that experienced Lithium precipitation with yields up to 90 % in the same alkaline conditions[130,147].

This optimal reaction time was employed for the high temperature batch tests, respectively at 50°C and 75°C, in order to investigate temperature impact in Li_2CO_3 precipitation.

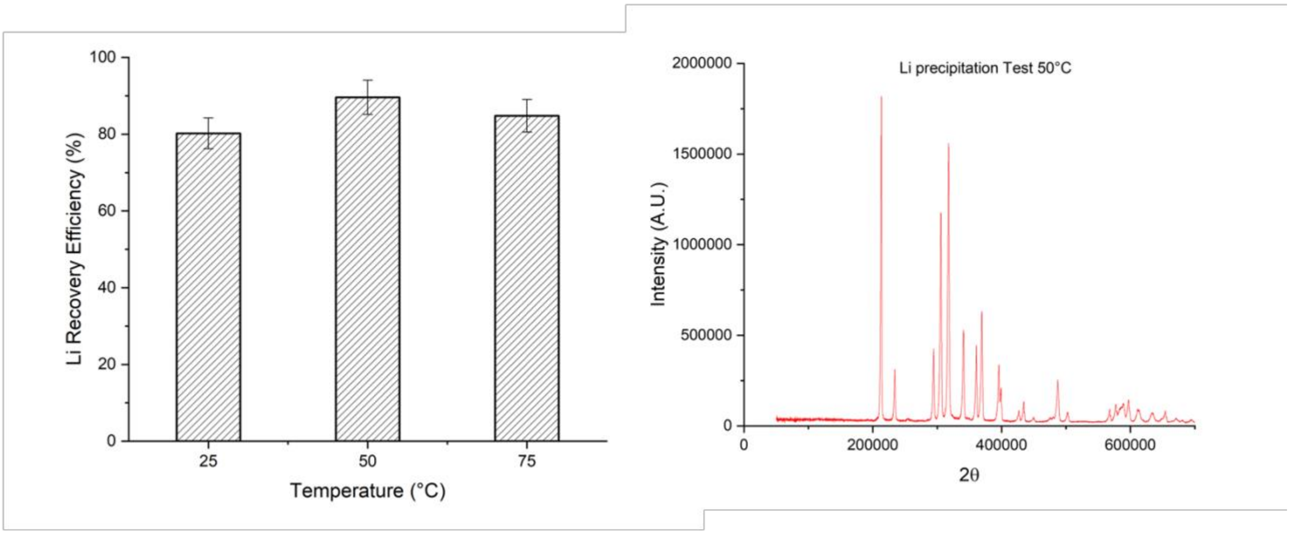

Figure 5.11 Plot of Lithium Removal efficiency in 24 hours batch tests at 25°C, 50°C, 75°C (left) and XRD spectrum of solids obtained from lithium precipitation step (right).

As highlighted in Figure 5.11, the highest lithium Removal Efficiency can be identified in 50 °C tests with a percentage up to 90 %, while the lowest value was observed in 25°C test with a percentage reduced of 10 % in comparison to the 50°C experiment.

This behavior can be explained considering, as said before, that the solubility of Li_2CO_3 decreases in combination with increase of temperature [130,165], thus allowing us to precipitate higher amounts of lithium working at the same operational temperature of the stream coming from air-gap MD step with the essential benefit of the optimization in the total amount of energy supplied to the process.

The XRD spectrum of the solid precipitated during 50°C test in figure 5.11 (right) showed a perfect match with the characteristic peaks of Li_2CO_3, confirming the purity of our solid.

5.4 Conclusions

In this last chapter it was assessed, studied and performed Lithium recovery from exhaust battery leachate, previously treated via Oxalates precipitation in order to remove metal impurities present in the leachate.

The first of the three phases in which our approach consisted was the pH adjustment, a pretreatment stage with the aim to precipitate sulfates under the form of $CaSO_4$ and other metal impurities in hydroxides form via $Ca(OH)_2$ addition.

Experimental results of this first set of experiments matched entirely the simulation performed using Oli Studio, with the complete elimination of metal impurities and sulfates combined with a pH value raised up to 12. During pH adjustment step, Lithium concentration was left intact thanks to its higher solubility limit.

The second step consisted in Lithium concentration increasing and water recovery via Air-Gap membrane distillation, with the aim to facilitate the lithium extraction via precipitation in the third step of our approach.

Also in this case, MD experimental performances have been outstanding, recovering high quality water with conductivities in the range of 2 - 6 μS/cm and with permeate fluxes oscillating between 16.5 and 15 L/m^2/h with an overall decrease of 6% during the distillation process. Low values of GOR and Specific Heat demand confirmed the thermal efficiency of the Lab-scale plant employed for these experiments.

Lithium recovery was performed through Na_2CO_3 addition to the MD retentate solution, obtaining a recovery efficiency above 80% at every different temperature (25, 50, 75 °C) with high purity of the obtained solid (>99%). The highest lithium Removal Efficiency can be identified in 50 °C tests with a percentage up to 90 %, while the lowest value was observed in 25°C test with a percentage reduced of 10 % in comparison to the 50°C experiment.

Chapter 6 – Conclusions and future perspectives

Energy transition and climate changes are pushing towards new frontiers in extraction of crucial metals and minerals for industrial purposes and, reasonably, EU and countries as China, Japan and others are announcing their carbon neutrality plans, setting off a new industrial era.

In this scenario, clean energy systems require more metal resources in terms of type and quantity compared to conventional energy systems, meaning that implementation of carbon neutrality targets will bring to an acceleration in deployment of clean energy technologies, which, in turn, will drive a growth in demand for metals and minerals resources and will force to face previously unknown challenges and demands on metal availability [167].

Metals and Minerals such as Cobalt, Manganese, Lithium and Magnesium are largely employed in crucial sectors like Aerospace, Energy, Constructions, Defense and Transports, and, consequently, the dependance of Europe on import of these metal ores from international market shows many implications for the feasibility of sustained and sustainable industrial development [168].

The climate changes, in combination with the high environmental impact of the traditional mining processes and the problematic politic relationships with the countries where these ores are mined, are pushing towards the necessity to cease this import reliance and to implement innovative technological approaches to secure an undistorted access to crucial raw materials.

Moreover, the mining sector exerts significant pressure on water resources, often leading to over-extraction and contamination of local water supplies. This can result in conflicts over water usage, impacting both the environment and local communities.

The contribution of this thesis work to this difficult scenario consisted in facing the previous described problems through the evaluation of the feasibility of innovative membrane-based technologies applied to unexplored and potentially significant alternative sources of minerals as seawater, natural and anthropic brines and leaching solutions of spent lithium-ion batteries. Moreover, these solutions are often highly diluted, and the membrane technology preconcentrates them, enabling the recovery of high-quality water exploitable for human use. Additionally, this approach not only facilitates the extraction of valuable minerals but also promotes sustainable water management by transforming waste streams into viable resources, thereby reducing environmental impact and enhancing resource efficiency.

Today RO brines are mainly considered as wastes of freshwater production, but in the next future they can be treated as resources thanks to the high concentration of minerals and, specifically, elements and species like: Chlorine, Sodium, Sulphates, Magnesium, Calcium and Carbonates [3].

Our approach was based on dehydration of the RO brine via Photothermal MD, in order to recover additional water and to perform a further concentration of the elements in the stream, everything seen in a logic of circular approach, valorization of waste and Blue Economy.

Photothermal MD was chosen as development of traditional MD processes with the aim to utilize the solar radiation to reverse the detrimental impact of the Temperature Polarization and, consequently, on high energy demand, that are the main problems affecting this technique.

The experimental work proved that the photothermal effect generated by carbon-based nanomaterials embodied in the membrane matrix, when irradiated by both UV or solar light, compensates the effect of Temperature polarization recording outstanding performance efficiencies and highlighting clearly superior permeate fluxes if compared to the bare hydrophobic PVDF membranes.

In the same direction, PhMD was extended up to crystallization, bringing the treated solution above saturation limit, achieving the extraction of dissolved solutes, in particular NaCl, the most abundant salt in seawater.

Therefore, carbon-based MMM's outperformed other membranes in terms of short nucleation time for NaCl from multi-ionic brine and demonstrating superior crystallization in both quality (size and dispersion) and quantity (crystallization yield).

Future perspectives on these technologies impose a progressive scale-up of the process, in order to investigate the benefits in terms of energy demand and evaporative flux as a preliminary step before selective mineral extraction from complex multi-ion solutions. In this scenario, DD process permits the selective extraction of cations from a saline stream exploiting Donnan equilibrium principle with the employment of a Strip phase, promoting an exchange of H^+ with other cations across a commercial Cation Exchange Membrane.

This technique has been implemented during this research work with the aim to extract Mg^{2+} ions from brines previously dehydrated via MD and to study and assess the transport propensity of the membranes and, consequently, the preferential stripping between monovalent and bivalent ions.

Due to the forementioned research goals, experimental results were performed employing single-ion solutions and a multi-ion solution, showing remarkable effectiveness in extraction of K^+, Na^+ and Mg^{2+} with a preferential permeation of Na^+ on other ionic species.

This technique could be employed on industrial scale for the selective removal of industrially valuable ions with the secondary purpose to drastically reduce the salinity of the treated RO brine before being rejected back to seas and ocean, in order to minimize the remarkable environmental impact on marine ecosystem, soil and groundwaters.

After ions recovery, it was assessed and performed a reactive precipitation treatment of the strip phase with the use of NaOH as precipitating agent, with the aim to induce Mg^{2+} precipitation and recovery under the form of hydroxide.

Future works oriented to DD need to make a step forward in membrane selectivity, involving the use of lab-made membranes incorporating Metal Organic Frameworks NPs in their polymeric matrix.

They are an emerging class of crystalline materials that can operate also as chemo-sensors in order to detect heavy metal ions like Lead, Copper and Iron [169] and, in addition, their sensitivity versus metal ions have been widely proved in literature [170] [171].

Higher selectivity of membranes employed in this process means higher recovery efficiencies of target ions, lower amounts of impurities in strip phase and reduced footprint of treatment plants at industrial levels, embracing the logic of process intensification.

MD and reactive precipitation were also employed for the treatment of exhaust battery leachate to extract and recovery Lithium, a crucial element that in the last two decades played a fundamental role in electronic industry and energy storage, with many implications in sectors like defense, automotive, telecommunications and computer industry.

The approach performed in this thesis work consisted in a preliminary step aimed to eliminate impurity ions increasing pH value of initial stream coming from battery acid leaching and, secondly, an Air-Gap MD process was employed for dehydration (water recovery) and concentration of the stream. This last step was crucial for the increasing of lithium concentration in the treated solution in order to optimize and maximize Lithium removal efficiency via reactive precipitation step.

Experimental results revealed a complete removal of impurities during the first step with the neutralization of the pH via $Ca(OH)_2$ addition , leaving unvaried our target ion concentration for the latter treatments in accordance with simulation performed through the employment of Oli Studio simulator.

Moreover, MD in Air-Gap configuration showed interesting permeate fluxes in combination to feasible specific heat demand to power the lab-scale plant.

The main advantage of the combination of the previous described treatment is the capacity to treat all types of highly acidic feeds coming from battery recycling at any scale, thanks to the lowering of the solubility of metal impurities with the increasing of pH value and to the sulfates elimination promoted by Ca^{2+} addition to the solution.

The last step, consisting in reactive precipitation via Na_2CO_3 addition, promoted high purity Li_2CO_3 precipitation with excellent recovery efficiencies, in accordance to simulation performed to optimize Na_2CO_3/Li ratio. The simplicity of the overall process and the employment of non-toxic and harmless reagents make this approach one of the feasible paths for the selective recovery of Lithium with the aim to fulfil the requirements of circular economy and recycling philosophy.

The promising results of this study not only validate the potential of these innovative membrane-based technologies but also highlight their role in promoting sustainable resource management. Moving forward, this research lays the groundwork for future studies focused on scaling up these processes, improving membrane selectivity, and integrating these solutions into industrial applications. Such advancements will be crucial in meeting the growing demand for critical metals, ensuring a sustainable and resilient supply chain in the face of global environmental and economic challenges.

Chapter 7 - Bibliography

[1] A. Panagopoulos, K.J. Haralambous, M. Loizidou, Desalination brine disposal methods and treatment technologies - A review, Science of the Total Environment 693 (2019). https://doi.org/10.1016/j.scitotenv.2019.07.351.

[2] I.G. Wenten, Khoiruddin, Reverse osmosis applications: Prospect and challenges, Desalination 391 (2016) 112–125. https://doi.org/10.1016/j.desal.2015.12.011.

[3] X. Ji, E. Curcio, S. Al Obaidani, G. Di Profio, E. Fontananova, E. Drioli, Membrane distillation-crystallization of seawater reverse osmosis brines, Sep Purif Technol 71 (2010) 76–82. https://doi.org/10.1016/j.seppur.2009.11.004.

[4] D. Blagoeva, G.A. 1969- Blengini, J. 1969- Dewulf, C. Baranzelli, C. Torres De Matos, V. Nita, B. Vidal-Legaz, C.E.L. 1984- Latunussa, Y. Kayam, L. Talens Peirò, S. Manfredi, L. Mancini, P. Nuss, A. 1981- Marmier, P. Alves-Dias, C.C. Pavel, E. Tzimas, F. Mathieux, D. Pennington, C. Ciupagea, Europäische Gemeinschaften Gemeinsame Forschungsstelle, Background report, n.d.

[5] M. Hofmann, H. Hofmann, C. Hagelüken, A. Hool, Critical raw materials: A perspective from the materials science community, Sustainable Materials and Technologies 17 (2018). https://doi.org/10.1016/j.susmat.2018.e00074.

[6] REPORT ON CRITICAL RAW MATERIALS FOR THE EU Report of the Ad hoc Working Group on defining critical raw materials, 2014.

[7] M. Girtan, A. Wittenberg, M.L. Grilli, D.P.S. de Oliveira, C. Giosuè, M.L. Ruello, The critical raw materials issue between scarcity, supply risk, and unique properties, Materials 14 (2021). https://doi.org/10.3390/ma14081826.

[8] D. Liu, X. Gao, H. An, Y. Qi, X. Sun, Z. Wang, Z. Chen, F. An, N. Jia, Supply and demand response trends of lithium resources driven by the demand of emerging renewable energy technologies in China, Resour Conserv Recycl 145 (2019) 311–321. https://doi.org/10.1016/j.resconrec.2019.02.043.

[9] B.B. Ashoor, S. Mansour, A. Giwa, V. Dufour, S.W. Hasan, Principles and applications of direct contact membrane distillation (DCMD): A comprehensive review, Desalination 398 (2016) 222–246. https://doi.org/10.1016/j.desal.2016.07.043.

[10] M. Quilaqueo, G. Seriche, L. Barros, C. González, J. Romero, R. Ruby-Figueroa, S. Santoro, E. Curcio, H. Estay, Water recovery assessment from hypersaline lithium-rich brines using Membrane Distillation-Crystallization, Desalination 537 (2022). https://doi.org/10.1016/j.desal.2022.115887.

[11] M.S. El-Bourawi, Z. Ding, R. Ma, M. Khayet, A framework for better understanding membrane distillation separation process, J Memb Sci 285 (2006) 4–29. https://doi.org/10.1016/j.memsci.2006.08.002.

[12] A. Cerda, M. Quilaqueo, L. Barros, G. Seriche, M. Gim-Krumm, S. Santoro, A.H. Avci, J. Romero, E. Curcio, H. Estay, Recovering water from lithium-rich brines by a fractionation process based on membrane distillation-crystallization, Journal of Water Process Engineering 41 (2021). https://doi.org/10.1016/j.jwpe.2021.102063.

[13] S. Santoro, P. Timpano, A.H. Avci, P. Argurio, F. Chidichimo, M. De Biase, S. Straface, E. Curcio, An integrated membrane distillation, photocatalysis and polyelectrolyte-enhanced ultrafiltration process for arsenic remediation at point-of-use, Desalination 520 (2021). https://doi.org/10.1016/j.desal.2021.115378.

[14] M. Aquino, S. Santoro, G. Di Profio, M.F. La Russa, C. Limonti, S. Straface, G. D’Andrea, E. Curcio, A. Siciliano, Membrane distillation for separation and recovery of valuable compounds from anaerobic digestates, Sep Purif Technol 315 (2023). https://doi.org/10.1016/j.seppur.2023.123687.

[15] E. ’Drioli, G.’ ’Di Profio, E.’ ’Curcio, Membrane-Assisted Crystallization Technology, 2015.

[16] E. Chabanon, D. Mangin, C. Charcosset, Membranes and crystallization processes: State of the art and prospects, J Memb Sci 509 (2016) 57–67. https://doi.org/10.1016/j.memsci.2016.02.051.

[17] S. Santoro, M. Aquino, C. Rizza, A. Cupolillo, D.W. Boukhvalov, G. D’Olimpio, S. Abramovich, A. Agarwal, M.B. Sadan, A. Politano, E. Curcio, Plasmonic nanofillers-enabled solar membrane crystallization for mineral recovery, Desalination 563 (2023). https://doi.org/10.1016/j.desal.2023.116730.

[18] S. Santoro, A.H. Avci, A. Politano, E. Curcio, The advent of thermoplasmonic membrane distillation, Chem Soc Rev 51 (2022) 6087–6125. https://doi.org/10.1039/d0cs00097c.

[19] S. Santoro, H. Estay, A.H. Avci, L. Pugliese, R. Ruby-Figueroa, A. Garcia, M. Aquino, S. Nasirov, S. Straface, E. Curcio, Membrane technology for a sustainable copper mining industry: The Chilean paradigm, Clean Eng Technol 2 (2021). https://doi.org/10.1016/j.clet.2021.100091.

[20] S. Santoro, I.M. Vidorreta, V. Sebastian, A. Moro, I.M. Coelhoso, C.A.M. Portugal, J.C. Lima, G. Desiderio, G. Lombardo, E. Drioli, R. Mallada, J.G. Crespo, A. Criscuoli, A. Figoli, A non-invasive optical method for mapping temperature polarization in direct contact membrane distillation, J Memb Sci 536 (2017) 156–166. https://doi.org/10.1016/j.memsci.2017.05.001.

[21] M. Khayet, Solar desalination by membrane distillation: Dispersion in energy consumption analysis and water production costs (a review), Desalination 308 (2013) 89–101. https://doi.org/10.1016/j.desal.2012.07.010.

[22] S. Santoro, I.M. Vidorreta, V. Sebastian, A. Moro, I.M. Coelhoso, C.A.M. Portugal, J.C. Lima, G. Desiderio, G. Lombardo, E. Drioli, R. Mallada, J.G. Crespo, A. Criscuoli, A. Figoli, A non-invasive optical method for mapping temperature polarization in direct contact membrane distillation, J Memb Sci 536 (2017) 156–166. https://doi.org/10.1016/j.memsci.2017.05.001.

[23] R. Molinari, A.H. Avci, P. Argurio, E. Curcio, S. Meca, M. Plà-Castellana, J.L. Cortina, Selective precipitation of calcium ion from seawater desalination reverse osmosis brine, J Clean Prod 328 (2021). https://doi.org/10.1016/j.jclepro.2021.129645.

[24] E. Balis, J.C. Griffin, S.R. Hiibel, Membrane Distillation-Crystallization for inland desalination brine treatment, Sep Purif Technol 290 (2022). https://doi.org/10.1016/j.seppur.2022.120788.

[25] A. Cerda, M. Quilaqueo, L. Barros, G. Seriche, M. Gim-Krumm, S. Santoro, A.H. Avci, J. Romero, E. Curcio, H. Estay, Recovering water from lithium-rich brines by a fractionation process based on membrane distillation-crystallization, Journal of Water Process Engineering 41 (2021). https://doi.org/10.1016/j.jwpe.2021.102063.

[26] A.H. Avci, S. Santoro, A. Politano, M. Propato, M. Micieli, M. Aquino, Z. Wenjuan, E. Curcio, Photothermal Sweeping Gas Membrane Distillation and Reverse Electrodialysis for light-to-heat-to-power conversion, Chemical Engineering and Processing - Process Intensification 164 (2021). https://doi.org/10.1016/j.cep.2021.108382.

[27] A. Politano, P. Argurio, G. Di Profio, V. Sanna, A. Cupolillo, S. Chakraborty, H.A. Arafat, E. Curcio, Photothermal Membrane Distillation for Seawater Desalination, Advanced Materials 29 (2017). https://doi.org/10.1002/adma.201603504.

[28] A. Politano, G. Di Profio, E. Fontananova, V. Sanna, A. Cupolillo, E. Curcio, Overcoming temperature polarization in membrane distillation by thermoplasmonic effects activated by Ag nanofillers in polymeric membranes, Desalination (2019) 192–199. https://doi.org/10.1016/j.desal.2018.03.006.

[29] S. Abramovich, D. Dutta, C. Rizza, S. Santoro, M. Aquino, A. Cupolillo, J. Occhiuzzi, M.F. La Russa, B. Ghosh, D. Farias, A. Locatelli, D.W. Boukhvalov, A. Agarwal, E. Curcio, M. Bar Sadan, A. Politano, NiSe and CoSe Topological Nodal-Line Semimetals: A Sustainable Platform for Efficient Thermoplasmonics and Solar-Driven Photothermal Membrane Distillation, Small 18 (2022). https://doi.org/10.1002/smll.202201473.

[30] S. Santoro, M. Aquino, D. Han Seo, T. Van Der Laan, M. Lee, J. Sung Yun, M. Jun Park, A. Bendavid, H. Kyong Shon, A. Halil Avci, E. Curcio, Dimensionally controlled graphene-based surfaces for photothermal membrane crystallization, J Colloid Interface Sci 623 (2022) 607–616. https://doi.org/10.1016/j.jcis.2022.05.062.

[31] S. Santoro, M. Aquino, C. Rizza, J. Occhiuzzi, D. Mastrippolito, G. D’Olimpio, A.H. Avci, J. De Santis, V. Paolucci, L. Ottaviano, L. Lozzi, A. Ronen, M. Bar-Sadan, D.S. Han, A. Politano, E. Curcio, Lithium recovery through WS2 nanofillers-promoted solar photothermal membrane crystallization of LiCl, Desalination 546 (2023). https://doi.org/10.1016/j.desal.2022.116186.

[32] P.D. Dongare, A. Alabastri, S. Pedersen, K.R. Zodrow, N.J. Hogan, O. Neumann, J. Wud, T. Wang, A. Deshmukh, M. Elimelech, Q. Li, P. Nordlander, N.J. Halas, Nanophotonics-enabled solar membrane distillation for off-grid water purification, Proc Natl Acad Sci U S A 114 (2017) 6936–6941. https://doi.org/10.1073/pnas.1701835114.

[33] Z. Xie, Y. Duo, Z. Lin, T. Fan, C. Xing, L. Yu, R. Wang, M. Qiu, Y. Zhang, Y. Zhao, X. Yan, H. Zhang, The Rise of 2D Photothermal Materials beyond Graphene for Clean Water Production, Advanced Science 7 (2020). https://doi.org/10.1002/advs.201902236.

[34] A. Politano, P. Argurio, G. di Profio, V. Sanna, A. Cupolillo, S. Chakraborty, H.A. Arafat, E. Curcio, Photothermal Membrane Distillation for Seawater Desalination, Advanced Materials 29 (2017). https://doi.org/10.1002/adma.201603504.

[35] E. Drioli, G. Di Profio, E. Curcio, Progress in membrane crystallization, Curr Opin Chem Eng 1 (2012) 178–182. https://doi.org/10.1016/j.coche.2012.03.005.

[36] C.A. Quist-Jensen, A. Ali, S. Mondal, F. Macedonio, E. Drioli, A study of membrane distillation and crystallization for lithium recovery from high-concentrated aqueous solutions, J Memb Sci 505 (2016) 167–173. https://doi.org/10.1016/j.memsci.2016.01.033.

[37] S.H. Park, J.H. Kim, S.J. Moon, J.T. Jung, H.H. Wang, A. Ali, C.A. Quist-Jensen, F. Macedonio, E. Drioli, Y.M. Lee, Lithium recovery from artificial brine using energy-efficient membrane distillation and nanofiltration, J Memb Sci 598 (2020). https://doi.org/10.1016/j.memsci.2019.117683.

[38] X. Li, Y. Mo, W. Qing, S. Shao, C.Y. Tang, J. Li, Membrane-based technologies for lithium recovery from water lithium resources: A review, J Memb Sci 591 (2019). https://doi.org/10.1016/j.memsci.2019.117317.

[39] M. Şahin, H. Görçay, E. Kir, Y. Şahin, Removal of calcium and magnesium using polyaniline and derivatives modified PVDF cation-exchange membranes by Donnan dialysis, React Funct Polym 69 (2009) 673–680. https://doi.org/10.1016/j.reactfunctpolym.2009.04.015.

[40] Q. Wang, J.J. Lenhart, H.W. Walker, Recovery of metal cations from lime softening sludge using Donnan dialysis, J Memb Sci 360 (2010) 469–475. https://doi.org/10.1016/j.memsci.2010.05.047.

[41] K. Pyrzynska, Preconcentration and recovery of metal ions by donnan dialysis, Microchimica Acta 153 (2006) 117–126. https://doi.org/10.1007/s00604-005-0434-4.

[42] T. Rijnaarts, N.T. Shenkute, J.A. Wood, W.M. De Vos, K. Nijmeijer, Divalent Cation Removal by Donnan Dialysis for Improved Reverse Electrodialysis, ACS Sustain Chem Eng 6 (2018) 7035–7041. https://doi.org/10.1021/acssuschemeng.8b00879.

[43] J.A. Wlśnlewskl, M. Kabsch-Korbutowicz, Elimination of selected anions and cations from water by means of the donnan dialysis, Environment Protection Engineering 43 (2017) 189–205. https://doi.org/10.5277/epe170313.

[44] A.R. O_ Za Nska, J. Wi, Modification of brackish water composition by means of Donnan dialysis as pretreatment before desalination, (n.d.). https://doi.org/10.1016/j.desal.2008.01.05.

[45] R. Gueccia, A.M.M. Alhadidi, A. Cipollina, G. Micale, Donnan dialysis for tap-water softening, Desalination Water Treat 192 (2020) 19–32. https://doi.org/10.5004/dwt.2020.26081.

[46] I. Marzouk-Trifi, L. Baklouti, L. Dammak, Investigation of Calcium and Magnesium Removal by Donnan Dialysis According to the Doehlert Design for Softening Different Water Types, Membranes (Basel) 13 (2023) 203. https://doi.org/10.3390/membranes13020203.

[47] C. Agarwal, S. Chaudhury, A.K. Pandey, A. Goswami, Kinetic aspects of Donnan dialysis through Nafion-117 membrane, J Memb Sci 415–416 (2012) 681–685. https://doi.org/10.1016/j.memsci.2012.05.049.

[48] Mike Agbesi Acheampong, Ebenezer David Okwaning Ansa, Low-Cost Technologies for Mining Wastewater Treatment, Journal of Environmental Science and Engineering B 6 (2017). https://doi.org/10.17265/2162-5263/2017.08.001.

[49] F. Matebese, A.K. Mosai, H. Tutu, Z.R. Tshentu, Mining wastewater treatment technologies and resource recovery techniques: A review, Heliyon 10 (2024). https://doi.org/10.1016/j.heliyon.2024.e24730.

[50] P.N. Alam, Yulianis, H.L. Pasya, R. Aditya, I.N. Aslam, K. Pontas, Acid mine wastewater treatment using electrocoagulation method, Mater Today Proc 63 (2022) S434–S437. https://doi.org/10.1016/j.matpr.2022.04.089.

[51] Z. Yan, H. Yang, F. Qu, H. Yu, H. Liang, G. Li, J. Ma, Reverse osmosis brine treatment using direct contact membrane distillation: Effects of feed temperature and velocity, Desalination 423 (2017) 149–156. https://doi.org/10.1016/j.desal.2017.09.010.

[52] W.T. Stringfellow, P.F. Dobson, Technology for the recovery of lithium from geothermal brines, Energies (Basel) 14 (2021). https://doi.org/10.3390/en14206805.

[53] M.P. Paranthaman, L. Li, J. Luo, T. Hoke, H. Ucar, B.A. Moyer, S. Harrison, Recovery of Lithium from Geothermal Brine with Lithium-Aluminum Layered Double Hydroxide Chloride Sorbents, Environ Sci Technol 51 (2017) 13481–13486. https://doi.org/10.1021/acs.est.7b03464.

[54] Z. Xie, T. Duong, M. Hoang, C. Nguyen, B. Bolto, Ammonia removal by sweep gas membrane distillation, Water Res 43 (2009) 1693–1699. https://doi.org/10.1016/j.watres.2008.12.052.

[55] X. Yang, H. Pang, J. Zhang, A. Liubinas, M. Duke, Sustainable waste water deammonification by vacuum membrane distillation without pH adjustment: Role of water chemistry, Chemical Engineering Journal 328 (2017) 884–893. https://doi.org/10.1016/j.cej.2017.07.104.

[56] D.M. Wang, J.Y. Lai, Recent advances in preparation and morphology control of polymeric membranes formed by nonsolvent induced phase separation, Curr Opin Chem Eng 2 (2013) 229–237. https://doi.org/10.1016/j.coche.2013.04.003.

[57] T. Marino, F. Russo, A. Figoli, The formation of polyvinylidene fluoride membranes with tailored properties via vapour/non-solvent induced phase separation, Membranes (Basel) 8 (2018). https://doi.org/10.3390/membranes8030071.

[58] M. Drobek, A. Figoli, S. Santoro, N. Navascués, J. Motuzas, S. Simone, C. Algieri, N. Gaeta, L. Querze, A. Trotta, G. Barbieri, R. Mallada, A. Julbe, E. Drioli, PVDF-MFI mixed matrix membranes as VOCs adsorbers, Microporous and Mesoporous Materials 207 (2015) 126–133. https://doi.org/10.1016/j.micromeso.2015.01.005.

[59] M. Khayet, T. Matsuura, Preparation and characterization of polyvinylidene fluoride membranes for membrane distillation, Ind Eng Chem Res 40 (2001) 5710–5718. https://doi.org/10.1021/ie010553y.

[60] M. Pagliero, A. Comite, O. Soda, C. Costa, Influence of carbon-based fillers on photoactive mixed matrix membranes formation, J Memb Sci 658 (2022). https://doi.org/10.1016/j.memsci.2022.120752.

[61] A. Figoli, S. Simone, A. Criscuoli, S.A. Al-Jlil, F.S. Al Shabouna, H.S. Al-Romaih, E. Di Nicolò, O.A. Al-Harbi, E. Drioli, Hollow fibers for seawater desalination from blends of PVDF with different molecular weights: Morphology, properties and VMD performance, Polymer (Guildf) 55 (2014) 1296–1306. https://doi.org/10.1016/j.polymer.2014.01.035.

[62] X. Wu, B. Zhao, L. Wang, Z. Zhang, M. Li, Preparation and characterization of superhydrophobic PVDF/HMSNs hybrid membrane for CO2 absorption, Polymer (Guildf) 214 (2021). https://doi.org/10.1016/j.polymer.2020.123242.

[63] S. Santoro, R.A. Tufa, A.H. Avci, E. Fontananova, G. Di Profio, E. Curcio, Fouling propensity in reverse electrodialysis operated with hypersaline brine, Energy 228 (2021). https://doi.org/10.1016/j.energy.2021.120563.

[64] Y. Yang, W. Rigdon, X. Huang, X. Li, Enhancing graphene reinforcing potential in composites by hydrogen passivation induced dispersion, Sci Rep 3 (2013). https://doi.org/10.1038/srep02086.

[65] L. Eykens, K. De Sitter, C. Dotremont, L. Pinoy, B. Van der Bruggen, Membrane synthesis for membrane distillation: A review, Sep Purif Technol 182 (2017) 36–51. https://doi.org/10.1016/j.seppur.2017.03.035.

[66] M. Pagliero, M. Alloisio, C. Costa, R. Firpo, E.A. Mideksa, A. Comite, Carbon Black/Polyvinylidene Fluoride Nanocomposite Membranes for Direct Solar Distillation, Energies (Basel) 15 (2022). https://doi.org/10.3390/en15030740.

[67] X.W.D.G.Q.J.S.C. and S.S. Young-Shin Jun, Photothermal Membrane Water Treatment for Two Worlds, Accounts of Chemical Research 52 (2019) 1215–1225.

[68] A. Ghaffar, Q. Imran, M. Hassan, M. Usman, M.U. Khan, Simultaneous solar water desalination and energy generation by high efficient graphene oxide-melanin photothermal membrane, J Environ Chem Eng 10 (2022). https://doi.org/10.1016/j.jece.2022.108424.

[69] S. Santoro, M. Aquino, D. Han Seo, T. Van Der Laan, M. Lee, J. Sung Yun, M. Jun Park, A. Bendavid, H. Kyong Shon, A. Halil Avci, E. Curcio, Dimensionally controlled graphene-based surfaces for photothermal membrane crystallization, J Colloid Interface Sci 623 (2022) 607–616. https://doi.org/10.1016/j.jcis.2022.05.062.

[70] G.R. Xu, M. Wang, K. Xu, H.L. Zhao, Q. Liu, Membrane fabrication and configuration design development of photothermal membrane distillation (PMD), Desalination 565 (2023). https://doi.org/10.1016/j.desal.2023.116833.

[71] P.D. Dongare, A. Alabastri, S. Pedersen, K.R. Zodrow, N.J. Hogan, O. Neumann, J. Wud, T. Wang, A. Deshmukh, M. Elimelech, Q. Li, P. Nordlander, N.J. Halas, Nanophotonics-enabled solar membrane distillation for off-grid water purification, Proc Natl Acad Sci U S A 114 (2017) 6936–6941. https://doi.org/10.1073/pnas.1701835114.

[72] A. Anvari, A. Azimi Yancheshme, K.M. Kekre, A. Ronen, State-of-the-art methods for overcoming temperature polarization in membrane distillation process: A review, J Memb Sci 616 (2020). https://doi.org/10.1016/j.memsci.2020.118413.

[73] S. Abramovich, D. Dutta, C. Rizza, S. Santoro, M. Aquino, A. Cupolillo, J. Occhiuzzi, M.F. La Russa, B. Ghosh, D. Farias, A. Locatelli, D.W. Boukhvalov, A. Agarwal, E. Curcio, M. Bar Sadan, A. Politano, NiSe and CoSe Topological Nodal-Line Semimetals: A Sustainable Platform for Efficient Thermoplasmonics and Solar-Driven Photothermal Membrane Distillation, Small 18 (2022). https://doi.org/10.1002/smll.202201473.

[74] C.R. Martinetti, A.E. Childress, T.Y. Cath, High recovery of concentrated RO brines using forward osmosis and membrane distillation, J Memb Sci 331 (2009) 31–39. https://doi.org/10.1016/j.memsci.2009.01.003.

[75] H. Geng, J. Wang, C. Zhang, P. Li, H. Chang, High water recovery of RO brine using multi-stage air gap membrane distillation, Desalination 355 (2015) 178–185. https://doi.org/10.1016/j.desal.2014.10.038.

[76] D. Woldemariam, A. Kullab, U. Fortkamp, J. Magner, H. Royen, A. Martin, Membrane distillation pilot plant trials with pharmaceutical residues and energy demand analysis, Chemical Engineering Journal 306 (2016) 471–483. https://doi.org/10.1016/j.cej.2016.07.082.

[77] A.S. Alsaadi, N. Ghaffour, J.D. Li, S. Gray, L. Francis, H. Maab, G.L. Amy, Modeling of air-gap membrane distillation process: A theoretical and experimental study, J Memb Sci 445 (2013) 53–65. https://doi.org/10.1016/j.memsci.2013.05.049.

[78] S.M. Alawad, A.E. Khalifa, Performance and energy evaluation of compact multistage air gap membrane distillation system: An experimental investigation, Sep Purif Technol 268 (2021). https://doi.org/10.1016/j.seppur.2021.118594.

[79] H.C. Duong, P. Cooper, B. Nelemans, T.Y. Cath, L.D. Nghiem, Evaluating energy consumption of air gap membrane distillation for seawater desalination at pilot scale level, Sep Purif Technol 166 (2016) 55–62. https://doi.org/10.1016/j.seppur.2016.04.014.

[80] Curcio Efrem, Drioli Enrico, Di Profio Gianluca, Membrane-assisted crystallization technology, First Edition, World Scientific Publishing, London,UK, 2015.

[81] P. Loganathan, G. Naidu, S. Vigneswaran, Mining valuable minerals from seawater: A critical review, Environ Sci (Camb) 3 (2017) 37–53. https://doi.org/10.1039/c6ew00268d.

[82] E. Drioli, E. Curcio, A. Criscuoli, G. Di Di Profio, Integrated system for recovery of CaCO3, NaCl and MgSO 4·7H2O from nanofiltration retentate, J Memb Sci 239 (2004) 27–38. https://doi.org/10.1016/j.memsci.2003.09.028.

[83] J., M.A., N.J. Garside, Measurement of crystal growth and nucleation rates, 2d Ed, IChemE, Rudby, 2002.

[84] T. Noguchi, M. Kimura, T. Hashimoto, M. Konno, T. Nakamura, M.E. Zolensky, A. Tsuchiyama, T. Matsumoto, J. Matsuno, R. Okazaki, M. Uesugi, Y. Karouji, T. Yada, Y. Ishibashi, K. Shirai, M. Abe, T. Okada, Sylvite and halite on particles recovered from 25143 Itokawa: A preliminary report, Meteorit Planet Sci 49 (2014) 1305–1314. https://doi.org/10.1111/maps.12333.

[85] S. Santoro, M. Aquino, C. Rizza, J. Occhiuzzi, D. Mastrippolito, G. D'Olimpio, A.H. Avci, J. De Santis, V. Paolucci, L. Ottaviano, L. Lozzi, A. Ronen, M. Bar-Sadan, D.S. Han, A. Politano, E. Curcio, Lithium recovery through WS2 nanofillers-promoted solar photothermal membrane crystallization of LiCl, Desalination 546 (2023). https://doi.org/10.1016/j.desal.2022.116186.

[86] A. Elshkaki, S. Lei, W.Q. Chen, Material-energy-water nexus: Modelling the long term implications of aluminium demand and supply on global climate change up to 2050, Environ Res 181 (2020). https://doi.org/10.1016/j.envres.2019.108964.

[87] J.E. Rodríguez, I. Razo, I. Lázaro, Water footprint for mining process: A proposed method to improve water management in mining operations, Cleaner and Responsible Consumption 8 (2023). https://doi.org/10.1016/j.clrc.2022.100094.

[88] J. Liu, M.D. Bearden, C.A. Fernandez, L.S. Fifield, S.K. Nune, R.K. Motkuri, P.K. Koech, B.P. McGrail, Techno-Economic Analysis of Magnesium Extraction from Seawater via a Catalyzed Organo-Metathetical Process, JOM 70 (2018) 431–435. https://doi.org/10.1007/s11837-017-2735-6.

[89] S. Santoro, A.H. Avci, M. Aquino, L. Pugliese, S. Straface, E. Curcio, Towards the Global Rise of Zero Liquid Discharge for Wastewater Management: The Mining Industry Case in Chile, in: 2021: pp. 505–518. https://doi.org/10.1007/698_2021_785.

[90] M. Tawalbeh, L. Qalyoubi, A. Al-Othman, M. Qasim, M. Shirazi, Insights on the development of enhanced antifouling reverse osmosis membranes: Industrial applications and challenges, Desalination 553 (2023). https://doi.org/10.1016/j.desal.2023.116460.

[91] M. Badruzzaman, N. Voutchkov, L. Weinrich, J.G. Jacangelo, Selection of pretreatment technologies for seawater reverse osmosis plants: A review, Desalination 449 (2019) 78–91. https://doi.org/10.1016/j.desal.2018.10.006.

[92] K.P. Lee, T.C. Arnot, D. Mattia, A review of reverse osmosis membrane materials for desalination-Development to date and future potential, J Memb Sci 370 (2011) 1–22. https://doi.org/10.1016/j.memsci.2010.12.036.

[93] C. Laspidou, K. Hadjibiros, S. Gialis, Minimizing the environmental impact of sea brine disposal by coupling desalination plants with solar saltworks: A case study for Greece, Water (Switzerland) 2 (2010) 75–84. https://doi.org/10.3390/w2010075.

[94] I. Abd-Elaty, A.E.L. Shahawy, S. Santoro, E. Curcio, S. Straface, Effects of groundwater abstraction and desalination brine deep injection on a coastal aquifer, Science of the Total Environment 795 (2021). https://doi.org/10.1016/j.scitotenv.2021.148928.

[95] R.D.R. Silva, R.T. Rodrigues, A.C. Azevedo, J. Rubio, Calcium and magnesium ion removal from water feeding a steam generator by chemical precipitation and flotation with micro and nanobubbles, Environmental Technology (United Kingdom) 41 (2020) 2210–2218. https://doi.org/10.1080/09593330.2018.1558288.

[96] F.L. Theiss, G.A. Ayoko, R.L. Frost, Synthesis of layered double hydroxides containing Mg 2+ , Zn 2+ , Ca 2+ and Al 3+ layer cations by co-precipitation methods - A review, Appl Surf Sci 383 (2016) 200–213. https://doi.org/10.1016/j.apsusc.2016.04.150.

[97] D. Hasson, V. Lumelsky, G. Greenberg, Y. Pinhas, R. Semiat, Development of the electrochemical scale removal technique for desalination applications, Desalination 230 (2008) 329–342. https://doi.org/10.1016/j.desal.2008.01.004.

[98] Y. Yu, H. Jin, P. Meng, Y. Guan, S. Shao, X. Chen, Electrochemical water softening using air-scoured washing for scale detachment, Sep Purif Technol 191 (2018) 216–224. https://doi.org/10.1016/j.seppur.2017.09.032.

[99] A.A.G.D. Amarasooriya, T. Kawakami, Removal of fluoride, hardness and alkalinity from groundwater by electrolysis, Groundw Sustain Dev 9 (2019). https://doi.org/10.1016/j.gsd.2019.100231.

[100] R.D. Chebotareva, S. V. Remez, S.Yu. Bashtan, Water Softening and Disinfection Using an Electrolysis Unit with a Filtering Cartridge, Journal of Water Chemistry and Technology 42 (2020) 54–59. https://doi.org/10.3103/s1063455x20010026.

[101] N. Kabay, M. Demircioglu, E. Ersiiz, I. Kurucaovali, Removal of calcium and magnesium hardness by electrodialysis, n.d. www.elsevier.com/locate/desal.

[102] S. K. Hamdona, H. R.Z. Tadros, D. M. Mabrouk, H. M. Refaat, Removal of Water Hardness and Some Inorganic Pollutants using Nano Marine Algae Extract Embedded in Waste Polystyrene, International Journal of Scientific and Research Publications (IJSRP) 12 (2022) 67–75. https://doi.org/10.29322/ijsrp.12.01.2022.p12111.

[103] F. Vassallo, D. La Corte, N. Cancilla, A. Tamburini, M. Bevacqua, A. Cipollina, G. Micale, A pilot-plant for the selective recovery of magnesium and calcium from waste brines, Desalination 517 (2021). https://doi.org/10.1016/j.desal.2021.115231.

[104] K. Walha, R. Ben Amar, L. Firdaous, F. Quéméneur, P. Jaouen, Brackish groundwater treatment by nanofiltration, reverse osmosis and electrodialysis in Tunisia: performance and cost comparison, Desalination 207 (2007) 95–106. https://doi.org/10.1016/j.desal.2006.03.583.

[105] J. Schaep, B. Van Der Bruggen, S. Uytterhoeven, R. Croux, C. Vandecasteele, D. Wilms, E. Van Houtte, F. Vanlerberghe, Removal of hardness from groundwater by nanofiltration, 1998.

[106] H. Chen, M. Rose, M. Fleming, S. Souizi, U. Shashvatt, L. Blaney, Recent advances in Donnan dialysis processes for water/wastewater treatment and resource recovery: A critical review, Chemical Engineering Journal (2022). https://doi.org/10.1016/j.cej.2022.140522.

[107] H. Dong, C. Unluer, E.H. Yang, A. Al-Tabbaa, Recovery of reactive MgO from reject brine via the addition of NaOH, Desalination 429 (2018) 88–95. https://doi.org/10.1016/j.desal.2017.12.021.

[108] H. Dong, C. Unluer, E.H. Yang, A. Al-Tabbaa, Synthesis of reactive MgO from reject brine via the addition of NH4OH, Hydrometallurgy 169 (2017) 165–172. https://doi.org/10.1016/j.hydromet.2017.01.010.

[109] S. Casas, C. Aladjem, E. Larrotcha, O. Gibert, C. Valderrama, J.L. Cortina, Valorisation of Ca and Mg by-products from mining and seawater desalination brines for water treatment applications, Journal of Chemical Technology and Biotechnology 89 (2014) 872–883. https://doi.org/10.1002/jctb.4326.

[110] F. Vassallo, D. La Corte, A. Cipollina, A. Tamburini, G. Micale, High purity recovery of magnesium and calcium hydroxides from waste brines, Chem Eng Trans 86 (2021) 931–936. https://doi.org/10.3303/CET2186156.

[111] D. La Corte, F. Vassallo, A. Cipollina, M. Turek, A. Tamburini, G. Micale, A novel ionic exchange membrane crystallizer to recover magnesium hydroxide from seawater and industrial brines, Membranes (Basel) 10 (2020) 1–14. https://doi.org/10.3390/membranes10110303.

[112] A.F. Mohammad, M.H. El-Naas, A.H. Al-Marzouqi, M.I. Suleiman, M. Al Musharfy, Optimization of magnesium recovery from reject brine for reuse in desalination post-treatment, Journal of Water Process Engineering 31 (2019). https://doi.org/10.1016/j.jwpe.2019.100810.

[113] A.H. Avci, T. Rijnaarts, E. Fontananova, G. Di Profio, I.F.V. Vankelecom, W.M. De Vos, E. Curcio, Sulfonated polyethersulfone based cation exchange membranes for reverse electrodialysis under high salinity gradients, J Memb Sci 595 (2020). https://doi.org/10.1016/j.memsci.2019.117585.

[114] R.A. Tufa, T. Piallat, J. Hnát, E. Fontananova, M. Paidar, D. Chanda, E. Curcio, G. di Profio, K. Bouzek, Salinity gradient power reverse electrodialysis: Cation exchange membrane design based on polypyrrole-chitosan composites for enhanced monovalent selectivity, Chemical Engineering Journal 380 (2020). https://doi.org/10.1016/j.cej.2019.122461.

[115] M. Vanoppen, G. Stoffels, C. Demuytere, W. Bleyaert, A.R.D. Verliefde, Increasing RO efficiency by chemical-free ion-exchange and Donnan dialysis: Principles and practical implications, Water Res 80 (2015) 59–70. https://doi.org/10.1016/j.watres.2015.04.030.

[116] C. Agarwal, A. Goswami, Nernst Planck approach based on non-steady state flux for transport in a Donnan dialysis process, J Memb Sci 507 (2016) 119–125. https://doi.org/10.1016/j.memsci.2016.02.021.

[117] F. Vassallo, C. Morgante, G. Battaglia, D. La Corte, M. Micari, A. Cipollina, A. Tamburini, G. Micale, A simulation tool for ion exchange membrane crystallization of magnesium hydroxide from waste brine, Chemical Engineering Research and Design 173 (2021) 193–205. https://doi.org/10.1016/j.cherd.2021.07.008.

[118] M. Ersoz, H. Kara, Cobalt(II) and Nickel(II) transfer through charged polysulfonated cation exchange membranes, J Colloid Interface Sci 232 (2000) 344–349. https://doi.org/10.1006/jcis.2000.7163.

[119] S. Ring, D. Hasson, H. Shemer, R. Semiat, Simple modeling of Donnan separation processes, J Memb Sci 476 (2015) 348–355. https://doi.org/10.1016/j.memsci.2014.12.001.

[120] K. Ando, J.T. Hynes, LIQUIDS HCl Acid Ionization in Water: A Theoretical Molecular Modeling, 1995.

[121] Q. Zhong, J. Li, L. Yang, G. He, T. Luo, O. Nir, D. Xu, X. Wang, Z. Zhang, Removal of iron, aluminum and magnesium ions from the wet-process phosphoric acid solutions via Donnan dialysis, J Memb Sci 697 (2024) 122451. https://doi.org/10.1016/j.memsci.2024.122451.

[122] D. La Corte, F. Vassallo, A. Cipollina, M. Turek, A. Tamburini, G. Micale, A novel ionic exchange membrane crystallizer to recover magnesium hydroxide from seawater and industrial brines, Membranes (Basel) 10 (2020) 1–14. https://doi.org/10.3390/membranes10110303.

[123] A. García-Olivares, J. Solé, O. Osychenko, Transportation in a 100% renewable energy system, Energy Convers Manag 158 (2018) 266–285. https://doi.org/10.1016/j.enconman.2017.12.053.

[124] M.Z. Jacobson, M.A. Delucchi, Providing all global energy with wind, water, and solar power, Part I: Technologies, energy resources, quantities and areas of infrastructure, and materials, Energy Policy 39 (2011) 1154–1169. https://doi.org/10.1016/j.enpol.2010.11.040.

[125] K. Hansen, C. Breyer, H. Lund, Status and perspectives on 100% renewable energy systems, Energy 175 (2019) 471–480. https://doi.org/10.1016/j.energy.2019.03.092.

[126] E. Muchuweni, E.T. Mombeshora, C.M. Muiva, T.S. Sathiaraj, Lithium-ion batteries: Recent progress in improving the cycling and rate performances of transition metal oxide anodes by incorporating graphene-based materials, J Energy Storage 73 (2023). https://doi.org/10.1016/j.est.2023.109013.

[127] X. Li, Y. Mo, W. Qing, S. Shao, C.Y. Tang, J. Li, Membrane-based technologies for lithium recovery from water lithium resources: A review, J Memb Sci 591 (2019). https://doi.org/10.1016/j.memsci.2019.117317.

[128] P.K. Choubey, M.S. Kim, R.R. Srivastava, J.C. Lee, J.Y. Lee, Advance review on the exploitation of the prominent energy-storage element: Lithium. Part I: From mineral and brine resources, Miner Eng 89 (2016) 119–137. https://doi.org/10.1016/j.mineng.2016.01.010.

[129] C. Liu, J. Lin, H. Cao, Y. Zhang, Z. Sun, Recycling of spent lithium-ion batteries in view of lithium recovery: A critical review, J Clean Prod 228 (2019) 801–813. https://doi.org/10.1016/j.jclepro.2019.04.304.

[130] A. Higuchi, N. Ankei, S. Nishihama, K. Yoshizuka, Selective Recovery of Lithium from Cathode Materials of Spent Lithium Ion Battery, JOM 68 (2016) 2624–2631. https://doi.org/10.1007/s11837-016-2027-6.

[131] E. Gerold, S. Luidold, H. Antrekowitsch, Separation and efficient recovery of lithium from spent lithium-ion batteries, Metals (Basel) 11 (2021). https://doi.org/10.3390/met11071091.

[132] A. Stamp, D.J. Lang, P.A. Wäger, Environmental impacts of a transition toward e-mobility: The present and future role of lithium carbonate production, J Clean Prod 23 (2012) 104–112. https://doi.org/10.1016/j.jclepro.2011.10.026.

[133] X. Chen, T. Zhou, J. Kong, H. Fang, Y. Chen, Separation and recovery of metal values from leach liquor of waste lithium nickel cobalt manganese oxide based cathodes, Sep Purif Technol 141 (2015) 76–83. https://doi.org/10.1016/j.seppur.2014.11.039.

[134] X. Sun, H. Hao, F. Zhao, Z. Liu, Tracing global lithium flow: A trade-linked material flow analysis, Resour Conserv Recycl 124 (2017) 50–61. https://doi.org/10.1016/j.resconrec.2017.04.012.

[135] J. Nan, D. Han, X. Zuo, Recovery of metal values from spent lithium-ion batteries with chemical deposition and solvent extraction, J Power Sources 152 (2005) 278–284. https://doi.org/10.1016/j.jpowsour.2005.03.134.

[136] J.F. Paulino, N.G. Busnardo, J.C. Afonso, Recovery of valuable elements from spent Li-batteries, J Hazard Mater 150 (2008) 843–849. https://doi.org/10.1016/j.jhazmat.2007.10.048.

[137] G. Dorella, M.B. Mansur, A study of the separation of cobalt from spent Li-ion battery residues, J Power Sources 170 (2007) 210–215. https://doi.org/10.1016/j.jpowsour.2007.04.025.

[138] H. Wang, B. Friedrich, Development of a Highly Efficient Hydrometallurgical Recycling Process for Automotive Li–Ion Batteries, Journal of Sustainable Metallurgy 1 (2015) 168–178. https://doi.org/10.1007/s40831-015-0016-6.

[139] W. Wang, W. Chen, H. Liu, Hydrometallurgical preparation of lithium carbonate from lithium-rich electrolyte, Hydrometallurgy 185 (2019) 88–92. https://doi.org/10.1016/j.hydromet.2019.02.013.

[140] D.P. Mantuano, G. Dorella, R.C.A. Elias, M.B. Mansur, Analysis of a hydrometallurgical route to recover base metals from spent rechargeable batteries by liquid-liquid extraction with Cyanex 272, J Power Sources 159 (2006) 1510–1518. https://doi.org/10.1016/j.jpowsour.2005.12.056.

[141] R.C. Wang, Y.C. Lin, S.H. Wu, A novel recovery process of metal values from the cathode active materials of the lithium-ion secondary batteries, Hydrometallurgy 99 (2009) 194–201. https://doi.org/10.1016/j.hydromet.2009.08.005.

[142] L. Li, J. Ge, R. Chen, F. Wu, S. Chen, X. Zhang, Environmental friendly leaching reagent for cobalt and lithium recovery from spent lithium-ion batteries, Waste Management 30 (2010) 2615–2621. https://doi.org/10.1016/j.wasman.2010.08.008.

[143] X. Xu, Y. Chen, P. Wan, K. Gasem, K. Wang, T. He, H. Adidharma, M. Fan, Extraction of lithium with functionalized lithium ion-sieves, Prog Mater Sci 84 (2016) 276–313. https://doi.org/10.1016/j.pmatsci.2016.09.004.

[144] S. Zandevakili, M. Ranjbar, M. Ehteshamzadeh, Recovery of lithium from Urmia Lake by a nanostructure MnO2ion sieve, Hydrometallurgy 149 (2014) 148–152. https://doi.org/10.1016/j.hydromet.2014.08.004.

[145] Q.B. Chen, Z.Y. Ji, J. Liu, Y.Y. Zhao, S.Z. Wang, J.S. Yuan, Development of recovering lithium from brines by selective-electrodialysis: Effect of coexisting cations on the migration of lithium, J Memb Sci 548 (2018) 408–420. https://doi.org/10.1016/j.memsci.2017.11.040.

[146] Z. yong Ji, Q. bai Chen, J. sheng Yuan, J. Liu, Y. ying Zhao, W. xian Feng, Preliminary study on recovering lithium from high Mg2+/Li+ ratio brines by electrodialysis, Sep Purif Technol 172 (2017) 168–177. https://doi.org/10.1016/j.seppur.2016.08.006.

[147] Y. Song, Z. Zhao, Recovery of lithium from spent lithium-ion batteries using precipitation and electrodialysis techniques, Sep Purif Technol 206 (2018) 335–342. https://doi.org/10.1016/j.seppur.2018.06.022.

[148] B. Han, R. Anwar Ul Haq, M. Louhi-Kultanen, Lithium carbonate precipitation by homogeneous and heterogeneous reactive crystallization, Hydrometallurgy 195 (2020). https://doi.org/10.1016/j.hydromet.2020.105386.

[149] S. Kim, H. Yoon, T. Min, B. Han, S. Lim, J. Park, Carbon dioxide utilization in lithium carbonate precipitation: A short review, Environmental Engineering Research 29 (2023) 230553–0. https://doi.org/10.4491/eer.2023.553.

[150] B.K. Biswal, U.U. Jadhav, M. Madhaiyan, L. Ji, E.H. Yang, B. Cao, Biological Leaching and Chemical Precipitation Methods for Recovery of Co and Li from Spent Lithium-Ion Batteries, ACS Sustain Chem Eng 6 (2018) 12343–12352. https://doi.org/10.1021/acssuschemeng.8b02810.

[151] M. Grágeda, A. González, M. Grágeda, S. Ushak, Purification of brines by chemical precipitation and ion-exchange processes for obtaining battery-grade lithium compounds, Int J Energy Res 42 (2018) 2386–2399. https://doi.org/10.1002/er.4008.

[152] M. Al, H. Shuva, A. Kurny, Hydrometallurgical Recovery of Value Metals from Spent Lithium Ion Batteries, American Journal of Materials Engineering and Technology 1 (2013) 8–12. https://doi.org/10.12691/materials-1-1-2.

[153] H. Liu, G. Azimi, Process analysis and study of factors affecting the lithium carbonate crystallization from sulfate media during lithium extraction, Hydrometallurgy 199 (2021). https://doi.org/10.1016/j.hydromet.2020.105532.

[154] A.L. Petrou, A. Terzidaki, Calcium carbonate and calcium sulfate precipitation, crystallization and dissolution: Evidence for the activated steps and the mechanisms from the enthalpy and entropy of activation values, Chem Geol 381 (2014) 144–153. https://doi.org/10.1016/j.chemgeo.2014.05.018.

[155] T. Yuan, J. Wang, Z. Li, Measurement and modelling of solubility for calcium sulfate dihydrate and calcium hydroxide in NaOH/KOH solutions, Fluid Phase Equilib 297 (2010) 129–137. https://doi.org/10.1016/j.fluid.2010.06.012.

[156] K. Johannsen, S. Rademacher, Modelling the kinetics of calcium hydroxide dissolution in water, Acta Hydrochimica et Hydrobiologica 27 (1999) 72–78. https://doi.org/10.1002/(SICI)1521-401X(199902)27:2<72::AID-AHEH72>3.0.CO;2-H.

[157] C. Morgante, F. Vassallo, G. Battaglia, A. Cipollina, F. Vicari, A. Tamburini, G. Micale, Influence of Operational Strategies for the Recovery of Magnesium Hydroxide from Brines at a Pilot Scale, Ind Eng Chem Res 61 (2022) 15355–15368. https://doi.org/10.1021/acs.iecr.2c02935.

[158] F. Moi, P. Teng, T. Tow Teng, A.K. Mohd Omar, Heavy Metals Removal by Hydroxide Precipitation and Coagulation-Flocculation Methods from Aqueous Solutions, 2009. http://iwaponline.com/wqrj/article-pdf/44/2/174/229542/wqrjc0440174.pdf.

[159] K. Boopathi, P. Rajesh, P. Ramasamy, Growth of negative solubility lithium sulfate monohydrate crystal by slow evaporation and Sankaranarayanan-Ramasamy method, J Cryst Growth 345 (2012) 1–6. https://doi.org/10.1016/j.jcrysgro.2012.01.036.

[160] https://www.ilo.org/dyn/icsc/showcard.display?p_card_id=0914&p_version=1&p_lang=it, (n.d.).

[161] A. Silambarasan, E.N. Rao, S.V. Rao, P. Rajesh, P. Ramasamy, Bulk growth, crystalline perfection and optical characteristics of inversely soluble lithium sulfate monohydrate single crystals grown by the conventional solvent evaporation and modified Sankaranarayanan-Ramasamy method, CrystEngComm 18 (2016) 2072–2080. https://doi.org/10.1039/c6ce00012f.

[162] E.K. Summers, J.H. Lienhard, Experimental study of thermal performance in air gap membrane distillation systems, including the direct solar heating of membranes, Desalination 330 (2013) 100–111. https://doi.org/10.1016/j.desal.2013.09.023.

[163] S. Al-Obaidani, E. Curcio, F. Macedonio, G. Di Profio, H. Al-Hinai, E. Drioli, Potential of membrane distillation in seawater desalination: Thermal efficiency, sensitivity study and cost estimation, J Memb Sci 323 (2008) 85–98. https://doi.org/10.1016/j.memsci.2008.06.006.

[164] D. Woldemariam, A. Kullab, E.U. Khan, A. Martin, Recovery of ethanol from scrubber-water by district heat-driven membrane distillation: Industrial-scale technoeconomic study, Renew Energy 128 (2018) 484–494. https://doi.org/10.1016/j.renene.2017.06.009.

[165] B. Han, R. Anwar Ul Haq, M. Louhi-Kultanen, Lithium carbonate precipitation by homogeneous and heterogeneous reactive crystallization, Hydrometallurgy 195 (2020). https://doi.org/10.1016/j.hydromet.2020.105386.

[166] J.N. Hausmann, B. Traynor, R.J. Myers, M. Driess, P.W. Menezes, The pH of Aqueous NaOH/KOH Solutions: A Critical and Non-trivial Parameter for Electrocatalysis, ACS Energy Lett 6 (2021) 3567–3571. https://doi.org/10.1021/acsenergylett.1c01693.

[167] J. Ju, Y. Feng, H. Li, C. Xu, Z. Xue, B. Wang, Extraction of valuable metals from minerals and industrial solid wastes via the ammonium sulfate roasting process: A systematic review, Chemical Engineering Journal 457 (2023). https://doi.org/10.1016/j.cej.2022.141197.

[168] https://ec.europa.eu/growth/content/raw-materials-scoreboard-2018_en Accessed on Jul2020, (n.d.).

[169] S.W. Lv, J.M. Liu, C.Y. Li, N. Zhao, Z.H. Wang, S. Wang, A novel and universal metal-organic frameworks sensing platform for selective detection and efficient removal of heavy metal ions, Chemical Engineering Journal 375 (2019). https://doi.org/10.1016/j.cej.2019.122111.

[170] Y. Zhao, M. Wu, Y. Guo, N. Mamrol, X. Yang, C. Gao, B. van der Bruggen, Metal-organic framework based membranes for selective separation of target ions, J Memb Sci 634 (2021). https://doi.org/10.1016/j.memsci.2021.119407.

[171] N. Yin, K. Wang, L. Wang, Z. Li, Amino-functionalized MOFs combining ceramic membrane ultrafiltration for Pb (II) removal, Chemical Engineering Journal 306 (2016) 619–628. https://doi.org/10.1016/j.cej.2016.07.064.